Engineering Calibration and Physical Principles of GNSS-Reflectometry for Earth Remote Sensing

by

Tianlin Wang

A dissertation submitted in partial fulfillment
of the requirements for the degree of
Doctor of Philosophy
(Electrical Engineering)
in the University of Michigan
2021

Doctoral Committee:

Professor Christopher Ruf, Chair
Associate Research Scientist Darren McKague
Professor Mark Moldwin
Professor Kamal Sarabandi
Professor Fawwaz Ulaby

Tianlin Wang

wangtl@umich.edu

ORCID iD: 0000-0002-4925-5915

To my family,
With love and gratitude.

ACKNOWLEDGEMENTS

First and foremost, I'd like to sincerely express my deepest gratitude and most sincere thanks to my advisor, Dr. Christopher Ruf, for his careful and patient supervision on formulating a research question, coming up with a practical and optimal solution, verifying scientific results with independent sources, delivering effective oral and written communication, etc. With his trust, patience and generosity, I learned how to conduct solid research, gained confidence in my abilities and built up my professional network. There are more things I have learned from him: how to be a good leader who always takes more responsibility and less credit; how to make decisions and accept what it is; how to prioritize work and meet deadlines; etc. He cares about his students as he cares about his satellites. It's my great honor and fortune to work under his supervision.

I would also like to extend my deep appreciation to my committee members for their long-term support and mentoring, as well as their insightful questions, constructive feedback, and invaluable advice for my research and dissertation. Dr. Fawwaz Ulaby taught me his phenomenal course on microwave remote sensing and since then he has been a great mentor and a role model, who provides consistent support and guidance to my career development. Dr. Kamal Sarabandi taught three remarkable courses on electromagnetic theory, microwave measurements, and wave scattering theory, which, just like a triangle, set up a solid basis for my research. Dr. Mark Moldwin has been very generously sharing his GPS lab with us to place our GNSS receiver over the long-term. Dr. Darren McKague, just like a co-advisor, is always there to help and support my research. What I have learned from them has shaped my philosophy of research, teaching, and service.

I'm deeply indebted to and extremely grateful to my senior collaborators for their great advising and mentoring. Dr. Valery Zavorotny always provides physical insight into a research problem and teaches me invaluable knowledge on electromagnetic wave theory and physical oceanography. Mr. Bruce Block has conducted numerous fundamental engineering calibration works for my research and also taught me many engineering skills and knowledge through his top-level bench work. Dr. Scott Gleason always sends me a detailed technical note that provides in-depth and throughout information whenever I ask a question. Dr. Andrew O'Brien has provided numerous brilliant ideas to improve these antenna calibration research works. Dr. Joel Johnson has shared many wise ideas and been very supportive of my postdoc fellowship application. It's my fortune to collaborate with these top experts in this field and learn from them.

I would like to extend my sincere thanks to my previous advisors: Dr. Leung Tsang has accepted me at the University of Washington (UW) and brought me to the University of Michigan (UM). He has taught me electromagnetic wave scattering theories and problem-solving skills from the fundamental physics rule; Dr. Ya-Qiu Jin, as my master thesis advisor, brought me into the research field of microwave remote sensing and inspired me to work harder and achieve better with his academic life. I am also very grateful to two mentors: Dr. Adriano Camps has encouraged and supported me on both research and professional development, as a role model serving the community and young professionals; Dr. Steffen Thoelert has very kindly shared their data and research with us, which have provided a guideline to address these GPS power variability in remote sensing. My special gratitude also goes out to Mr. Anthony Russel, Ms. Dorina Twigg, and Mr. Tim Butler from the CYGNSS Science Operation Center (SOC) and the Space Physics Research Laboratory, who have provided long-term technical support and prepared tons of datasets used in my research. My wonderful journey in academia would not have been possible without them.

My sincere thanks should also go to many researchers from the CYGNSS science team and the broad community for their encouragement, constructive feedback, and patience for the long-term calibration/validation work, including Drs. Mahta Moghaddam, Derek Posselt, Simon Yueh, Dara Entekhabi, Faozi Said, Mohammad Al-Khaldi, Ruzbeh Akbar, Bachir Annane, Shakeel Asharaf, Mauricio di Bisceglie, Alexandra Bringer, Charles Bussy-Virat, Estel Cardallach, Paul Chang, Shuyi Chen, Clara Chew, Maria-Paola Clarizia, Juan Crespo, Giuseppe Foti, Lilli Galdi, James Garrison, Feixiong Huang, Zorana Jelenak, Mark Leidner, Eric Loria, Hugo Carreno Luengo, David Moroni, Stephen Musko, Lin Van Nieuwstadt, Yulin Pan, Daniel Pascual, Nazzareno Pierdicca, Damen Provost, Zhaoxia Pu, Rashmi Shah, C. K. Shum, Seubson Soisuvarn, Derek Starkenburg, Baijun Tian, Martin Unwin, Xiaochun Wang, April Warnock, Yuchan Yi, Cinzia Zuffada and many others.

I am very grateful to colleagues from the IEEE Geosciences and Remote Sensing Society and also IEEE for their support to my service and career development, including Drs. Leland Pierce, Subit Chakrabarti, Mariko Burgin, Sidarth Misra, Paolo Gamba, Laura Natalia Puerto Caro, Allison Fleisher, James Garrison, Ashish Ghosh, Jasmeet Judge, George Komar, David Kunkee, Kristen MacCartney, Mauro Dalla Mura, Rosa Correa Pabon, Steven Reising, Tushar Sharma, Mustafa Ustuner, and many others.

I must also sincerely thank many faculty members for teaching great courses and advising my career, including: Drs. Amir Mortazawi, Mark Kushner, Anthony Grbic, Mingyan Liu, Eric Michielssen, Sandeep Pradhan, Kim Winick, and Adib Nashashibi from UM Electrical and Computer Engineering (ECE); Drs. Sushil Atreya, James Slavin, Lennard Fisk, John Boyd, Aaron Ridley, Enrico Landi, Roger De Roo, Jeremy Bassis, Frank Marsik, Ashley Payne, Allison Steiner, and Nilton Renno from UM Climate and Space Sciences and Engineering (CLaSP); Drs. Yasuo

Kuga and Vikram Jandhyala from UW ECE; and many instructors who have taught me at Fudan University, East China University of Science and Technology, and Shanghai Normal University.

I gratefully acknowledge the staff team who provided kind support and prompt assistance, including Kristen Thornton, Steve Pejuan, Michelle Chapman, Stacie Printon, John Feldkamp, Anne Rhoades, Katherine Godwin, Kim Novak, Alesha Montgomery, and Jennifer Feneley from UM ECE; Marti Moon, E J Olsen, Sandra Pytlinski, Barbara Lupi, Michael Meister, Claire Miller, Faye Ogasawara, Bryan K White, Darren Britten-Bozzone, Kevin McLaughlin, Rachel Long, Rick Baker, Jodi Holbrook, Jessica Pfund, Eidilia Thomas, Laura Hopkins, Shannon Coon, Deborah Eddy, and Lindsay Coleman from UM CLaSP; Bryan Crockett from UW ECE. I'd also like to recognize the assistance from staff team with Center for Research on Learning and Teaching in Engineering (CRLT-Engin) at UM, including Tershia Pinder-Grover, Audra Baleisis, Grenmarie Agresar, Gina Michael, Carol Lagemann, and many engineering teaching consultants (ETCs) I have worked with over past four years.

Many thanks go to my fellow lab mates, including: Shannon Brown, Sidarth Misra, David Chen, Mary Morris, Jinzheng Peng, John Xun Yang, Rachael Kroodsma, Cynthia Gerlein-Safdi, David Mayers, Rajeswari Balasubramaniam, Rachel Norris, Charles Powell, Mahnaz Vahdat, Ethan Gregory, and Madeline Evans. It's my great pleasure to work with you at the same space.

I want to specially acknowledge many mentors and colleagues who have supported and advised my pursuit of higher education, including Drs. Mark Wieczorek from Observatoire de la Côte d'Azur, Sarah Seager from Massachusetts Institute of Technology (MIT), Wolfgang-Martin Boerner from University of Illinois at Chicago (UIC), Wenzhe Fa from Peking University, Chongye Zhu, Dongxin Liu, Hongxia Ye, Geng-Ming Jiang and Feng Xu from Fudan University, Lei Zhang, Checheng Liang, David Chang, and many others.

I would also like to thank many friends since I studied abroad, including: Omar Abdelatty, Abdulrahman Alaqeel, Laura Andre, Navid Barani, Michael Benson, Jordan Budhu, Xiuzhang Cai, Ruiying Chai, Nikolaos Chiotellis, Amanda Couch, Tanner Douglas, Yanlei Du, Ruoxing Gao, Weihui Gu, Shouchang Guo, Shuo Huang, Ashley Jian, Armin Jam, Mani Kashanianfard, Milad Zolfagharloo Koohi, Tarun Kumar, Tien-Hao Liao, Amanda Lietz, Yunbo Liu, Josip Loncar, Mohammad Mousavi, Abdelhamid Nasr, Chenhui Qu, Brian Raeker, Menglou Rao, Maryam Salim, Shurun Tan, Brian Tierney, Xiaoyu Wang, Jiangfeng Wu, Zhanni Wu, Haokui Xu, Behzad Yektakhah, Mostafa Zaky, and Jiyue Zhu from the Radiation Laboratory and UM ECE; Abigail Azari, Dan Brandt, Zachary Butterfield, Xiuhong Chen, Yi-Hsuan Chen, Yuxi Chen, Paige Cooley, Ryan Dewey, Zachary Fair, Alan Gorchov-Negron, Camilla Harris, Zhenguang Huang, Geoffrey Jenkins, Garrett Limon, Garima Malhotra, Taylor Morton, Agnit Mukhopadhyay, Fang Pan, Genevieve Plant, Jiaen Ren, Yeimy Rivera, Yash Sarkango, Tong Shi, Yinsi Shou, Sarah Spitzer, David Sweeney, Anthony Torres, Tara Vega, Zihan Wang, Xiantong Wang, Emily Yang, Hongyang Zhou, and Jialei Zhu from UM CLaSP; Eshita Khera and Adam Ley from Tau Beta Pi Michigan Gamma; Xin Chang, Xudong Li, Chenxin Su, Hao Fang, Zhijun Zhou, Huazeng Deng, and Shadi Aslebagh from UW ECE.

Last but not least, I would like to express my deepest gratitude and love to my parents, Zefu Wang and Wuqin Gong for the sacrifices they have made and the endless love they have for me. They are always the strongest support behind me in all my pursuits. My deep gratitude goes to family members, grandma Jinhua Yao, uncle Shaoming Gong, aunt Qiaoyu Zhu, sister Guangxu Wang, and brother-in-law Zhiqiang Hu, for their faith in me and support for me. I’m also deeply indebted to my significant other, and I can never adequately express my sincere thanks for her unconditional love and steadfast support over the many years.

TABLE OF CONTENTS

LIST OF TABLES

LIST OF FIGURES

ABSTRACT

The Cyclone Global Navigation Satellite System (CYGNSS) is a NASA mission that uses 32 Global Positioning System (GPS) satellites as active sources and 8 CYGNSS satellites as passive receivers to measure ocean surface roughness and wind speed, as well as soil moisture and flood inundation over land. This dissertation addresses two major aspects of engineering calibration: (1) characterization of the GPS effective isotropic radiated power (EIRP) for calibration of normalized bistatic radar cross section (NBRCS) observables; and (2) development of an end-to-end calibration approach using modeling and measurements of ocean surface mean square slope (mss).

EIRP, defined as the product of the transmit power and antenna gain, is a key parameter needed to determine the power incident on the Earth surface, and therefore is significant to the calibration of Level 1 NBRCS. Major challenges in the estimation of GPS EIRP include: 1) temporal variation of the transmit power, 2) limited knowledge of the transmit antenna pattern, and 3) gain uncertainty due to pattern asymmetry and GPS spacecraft yaw maneuvers. The uncertainty in GPS EIRP is considered to contribute the largest component to the overall CYGNSS error budget.

To estimate the GPS transmit power, a ground-based GPS constellation power monitor (GCPM) system has been built to accurately and precisely measure the direct GPS signals. Radiometric calibration is performed to determine the system dynamic range and to calibrate GCPM gain. A GPS signal simulator is used to compute the scale factor that converts the measured counts into power in watts. The GCPM received power is highly repeatable and has been verified

with independent measurements made by the German Space Operations Center (GSOC) of The German Aerospace Center (DLR). The transmit power of the L1 coarse/acquisition (C/A) code of the full GPS constellation is estimated using an optimal search algorithm. Updated values for transmit power have been successfully applied to CYGNSS L1b calibration and found to significantly reduce the PRN dependence of CYGNSS L1 and L2 data products.

The gain pattern of each GPS satellite's transmit antenna for the L1 C/A signal is determined from measurements of signal strength received by the 8-satellite CYGNSS constellation. Mapping the complete on-Earth portion of the GPS main beam is enabled by the variety of measurement geometries that result from the GPS and CYGNSS orbits. Conversely, the gain pattern of the receive antenna on each CYGNSS satellite is also determined from the measurements. Determination of GPS patterns requires knowledge of CYGNSS patterns and vice versa, so a procedure is developed to solve for both of them iteratively. The procedure is shown to converge to a final set of patterns that is independent of first guess assumptions about the patterns. In both GPS and CYGNSS cases, the patterns derived here differ from those based on pre-launch measurements of the antenna mounted on approximate physical mockups of the satellite. The differences are inferred to result from inadequacies in the fidelity of the mockups and limitations in the repeatability of satellite final assembly when multiple versions are built. The new GPS and CYGNSS patterns have been incorporated into the science data processing algorithm used by the CYGNSS mission and result in improved calibration performance.

Variable transmit power by numerous Block IIF and IIR-M GPS space vehicles has been observed due to their flex power mode. Non-uniformity in the GPS antenna gain patterns further complicates EIRP estimation. A dynamic calibration approach is developed to address GPS EIRP variability. It uses measurements by the direct received GPS signal to estimate GPS EIRP in the

specular reflected direction and then incorporates them into the calibration of NBRCS. Error analyses using Monte Carlo simulations and a root sum-of-squares (RSS) approach show that the resulting error in NBRCS is about 0.32 dB. Dynamic EIRP calibration instantaneously detects and corrects for power fluctuations in the GPS transmitters and significantly reduces errors due to GPS antenna gain azimuthal asymmetry. It allows observations with the most variable Block IIF transmitters (approximately 37% of the GPS constellation) to be included in the standard data products and further improves the calibration quality of the NBRCS.

A physics-based approach is then proposed to examine potential calibration errors and to further improve the Level 1 calibration. The mean square slope (mss) is a key physical parameter that relates the ocean surface properties (wave spectra) to the CYGNSS measurement of NBRCS. An approach to model the mss for validation with CYGNSS mss data is developed by adding the contribution of a high frequency tail to the WAVEWATCH III (WW3) mss from Institut Français de Recherche pour l'Exploitation de la Mer (IFREMER, English: French Research Institute for Exploitation of the Sea). It is demonstrated that the ratio of CYGNSS mss to modified WW3 mss can be used to diagnose potential calibration errors that exist in the Level 1 calibration algorithm. This approach can help to improve CYGNSS data quality, including the Level 1 NBRCS and Level 2 ocean surface wind speed and roughness.

To summarize, the engineering calibration methods presented in this dissertation make significant contributions to the spatial coverage, calibration quality of the measured NBRCS and the geophysical data products produced by the NASA CYGNSS mission. These are critical for unleashing the full potential of the mission in many high-level scientific applications, for example, tracking hurricane intensity and flood inundation after landfall, resolving diurnal variations in ocean surface winds and heat flux, and capturing the rapid dry down response of soil moisture to

extreme precipitation events. The research is also useful to the system design, science investigation and engineering calibration of future GNSS-reflectometry missions.

CHAPTER I

Introduction

1.1 Global Navigation Satellite System (GNSS)

Global navigation satellite system (GNSS) is the standard generic term for satellite navigation systems that provide positioning, navigation, and timing (PNT) services on a global basis. GNSS consists of four major segments: the space segment (constellation of satellites), the control segment (worldwide monitor and control stations), the user segment (receiver equipment), and the augmentation segment (satellite-based and ground-based augmentation systems). GNSS satellites broadcast synchronized signals containing orbital data and the precise time of the signal transmission. The GNSS receiver compares the time of broadcast to the local time of reception to determine the time-of-flight (TOF) to each satellite. The pseudorange representing the satellite-user range is computed by multiplying the speed of light by the TOF. Pseudorange measurements from at least four satellites are needed to estimate the four unknowns: three coordinates of user position and receiver clock bias [1] [2].

Satellite navigation has its origin in the Sputnik era when scientists were able to track the satellite with shifts in its radio signal known as the 'Doppler Effect'. Transit, a pioneering Doppler-based system, was realized with four to seven satellites in low-altitude (1100 km), nearly circular, polar orbits, each broadcasting signals at 150 MHz and 400 MHz with total transmit power of 1 watt. Only one satellite was in view at a time, and a user waited up to 100 minutes before successive

satellite passes to determine position. Transmit was successfully used to update a ship's position and reset the inertial navigation system [3]. The success of Transit led to the development of the Global Positioning System (GPS): 1) the basic architecture of a Medium Earth Orbit (MEO) was approved in 1973; 2) the first Navigation System with Timing and Ranging (NAVSTAR) satellite was launched in 1978; 3) the system was declared fully operational in 1995; 4) as of August 2020, 75 GPS satellites have been launched, 31 of which are operational, 9 in reserve, 3 being tested, 30 have been retired and 2 were lost at launch. GPS is now a multi-use, space-based navigation system that meets national defense, homeland security, civil, commercial, and scientific needs [4].

The success of GPS has inspired the development of similar GNSS, regional navigation satellite systems (RNSS), and space-based augmentation systems (SBAS), including Russia's GLObal NAvigation Satellite System (GLONASS), China's BeiDou Navigation Satellite System (BDS), the European Union's Galileo, Japan's Quasi-Zenith Satellite System (QZSS), and India's Indian Regional Navigation Satellite System (IRNSS) [5]. GPS, GLONASS and Galileo constellations are all in MEO with 31, 24, and 24 operational satellites, respectively, while BDS has 24 satellites in MEO, 3 in Geostationary Earth Orbit (GEO) and 3 in Inclined Geosynchronous Orbit (IGSO). QZSS has 1 Geosynchronous Earth Orbit (GEO) and 3 Tundra-type orbit operational satellites, and IRNSS has 3 GEO and 9 IGSO operational satellites. As of September 2020, the GPS, GLONASS, BDS, and Galileo are fully operational GNSSs. QZSS is scheduled for 2023 to be independent of GPS. The IRNSS is planned to be expanded to a global version.

1.2 GNSS-Reflectometry for Earth Remote Sensing

GPS was created solely for global navigation purposes. It soon became clear that signals from GPS and other GNSS satellites can be used for Earth remote sensing and many other

applications [6], [7]. GNSS signals were proposed for ratio occultation remote sensing of the Earth's atmosphere [8], [9], with the first observations and processing performed in a GPS/MET experiment [10], [11]. It was also proposed to use the GNSS signals reflected from the Earth's surface for scatterometry [12] and ocean altimetry [13]. It was then demonstrated from an aircraft experiment that the reflected GNSS signals could be used to sense ocean surface roughness and wind speed [14], [15]. The GNSS signal reflections at very low grazing angles were occasionally observed during radio occultation experiment [16], [17], and the first GNSS signal reflection at steep incidence was serendipitously found in calibration data during the SIR-C radar experiment [18]. More elaborate airborne GNSS-R campaigns were conducted to measure various geophysical parameters of Earth environment, including the retrieval of wind speed and wind vector above rough seas [19]–[21], the mean square slopes [22], and wind speed in tropical cyclones [23]–[25]. GNSS-R has also been applied to make altimetry measurements [26]–[32] and sea-ice sensing [33], [34] during various airborne campaigns. Besides these, GNSS-R was also used to estimate the near-surface soil moisture content over land in both airborne and ground-based experiments [35]–[37].

The first spaceborne GNSS-R remote-sensing measurements were performed during the UK Disaster Monitoring Constellation (DMC) mission in 2004 [38]. It has been demonstrated that GNSS-R is feasible to remotely sensing global ocean, land and ice sensing at spacecraft altitudes [39]–[43]. Following its success, a GNSS-R instrument, the SGR-ReSI receiver was developed and integrated with the TechDemoSat-1 (TDS-1) satellite [44], [45]. TDS-1 was launched in 2015 in a Sun-synchronous near-circular orbit (inclination = 98.8º) with an altitude of ~ 635 km. TDS-1 collected data since then until its end of service in December 2018. Carrying a similar SGR-ReSI receiver, the eight-satellite constellation of the NASA Cyclone Global Navigation Satellite System

(CYGNSS) mission was launched in December 2016. CYGNSS is flying in a non-synchronous near-circular orbit (all spacecraft in a single plane) with an altitude ~ 520 km . The eight satellites are inclined at 35º to provide better coverage and a fast revisit of tropical regions to better observe the track and intensity of tropical cyclone [6], [46], [47]. Launched in 2016, the 3Cat-2 was the first CubeSat mission dedicated to GNSS-R technique [48]. In June 2019, BuFeng-1 A/B twin satellites were successfully deployed in orbit by a Chinese first-time sea platform launch. Each satellite carries two nadir sciences antennas directed at the left and right sides of the spacecraft with an inclination angle of 26° [49]. Spire launched two GNSS-R CubeSats on an Indian Polar Satellite Launch Vehicle (PSLV) in December 2019 [50]. The FSSCat mission, consisting of two federated 6-Unit CubeSats, named ^{3}Cat-5/A and ^{3}Cat-5/B was launched in September 2020. Each CubeSat carries a dual microwave payload (a GNSS-R and an L-band radiometer with interference detection/mitigation), and a multi-spectral optical payload to measure soil moisture, ice extent, and ice thickness, and to detect melting ponds over ice [51]. Besides these GNSS-R missions, in 2015, the SMAP radar receiver was re-tuned to 1227.6 MHz (GPS L2 frequency) to collect reflected GPS signals at two polarizations (Horizontal H and Vertical V) [52]. These developments have been accompanied by increased activity with many other satellite missions [53]–[55]. Past, current and future spaceborne GNSS-R missions are summarized in Table I-1, adapted from a recent report on standards of GNSS-R [56].

The advancements of these spaceborne missions lead to a large number of GNSS-R scientific applications, including: 1) altimetry [57]–[60], wind speed in tropical cyclones [61]–[64] as well as global winds [65]–[67], and swell waves [68]–[70] over ocean surface; 2) soil moisture content [71]–[80], biomass [81]–[83], flood inundation [84]–[88], and wetland dynamics [89], [90] over land surface; 3) sea ice [91]–[96] and glaciers [97], [98] in the cryosphere.

Table I-1 Past, present, and future space-borne GNSS-R missions [56]

Mission	Year	GNSS-R type	Band/Pol	GNSS system used
UK-DMC	2003	cGNSS-R	L1 / LHCP	GPS
UK-TDS-1	2015	cGNSS-R	L1 / LHCP	GPS
CYGNSS	2016	cGNSS-R	L1 / LHCP	GPS
^{3}Cat-2	2016	cGNSS-R rGNSS-R iGNSS-R	L1, L2 / LHCP, RHCP	GPS, GLONASS, Galileo, BeiDou
SMAP GNSS-R	2017	cGNSS-R	L2 / H, V	GPS
BuFeng-1 A/B	2019	cGNSS-R	L1 / LHCP	GPS BeiDou
Spire	2019	cGNSS-R	L1 / LHCP	GPS Galileo
^{3}Cat-5 A/B (FSSCat mission)	2020	cGNSS-R	L1 / LHCP	GPS Galileo
Fengyun-3 series	2020	cGNSS-R	L1 / LHCP	GPS Galileo BeiDou
^{3}Cat-4	2021	cGNSS-R	L1, L2 / LHCP	GPS Galileo
PRETTY	2021	iGNSS-R	L1 / RHCP	GPS Galileo

* cGNSS-R: conventional GNSS-R; rGNSS-R: Reconstructed-code GNSS-R; iGNSS-R: interferometric GNSS-R; LHCP: Left Hand Circular Polarization; RHCP: Right Hand Circular Polarization.

1.3 GNSS-R Bistatic Scattering Models

GNSS-R uses a bistatic radar configuration, with the transmitter and the receiver flying in very different orbit planes, as shown in Figure I.1. Measuring a temporal delay between the direct and reflected signals and recalculating it into spatial distance turns GNSS-R into an altimeter. Measuring the peak power and waveform of the scattered GNSS signal and retrieving geophysical properties (surface roughness, dielectric constant, etc.) from these measurements makes GNSS bistatic radar a multi-beam scatterometer [7].

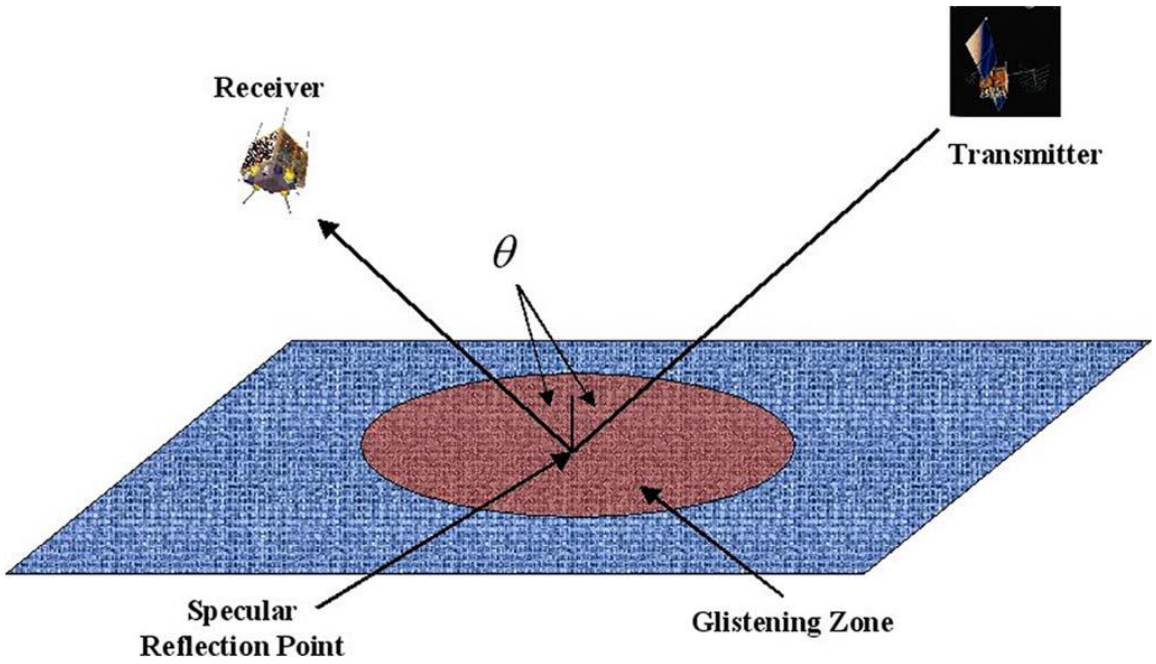

Figure I.1 Overall system configuration of the GNSS-R concept [43]

The typical GNSS-R observables are the delay-waveforms and Delay Doppler Maps (DDMs). Figure I.2 depicts an idealized case of the satellite receiver at 600-km altitude, flying in the same plane as the GNSS transmitter. The left panel shows the surface coordinate system and the right panel shows the corresponding horseshoe-shape DDM. Pixels in the surface coordinate domain formed by intersecting equi-range (green ellipses) and equi-Doppler (black curve) lines

correspond to pixels in the delay-Doppler domain of the DDM. The intensity of every DDM pixel is proportional to scattered power originating from the pair of pixels located symmetrically with respect to line AB [7].

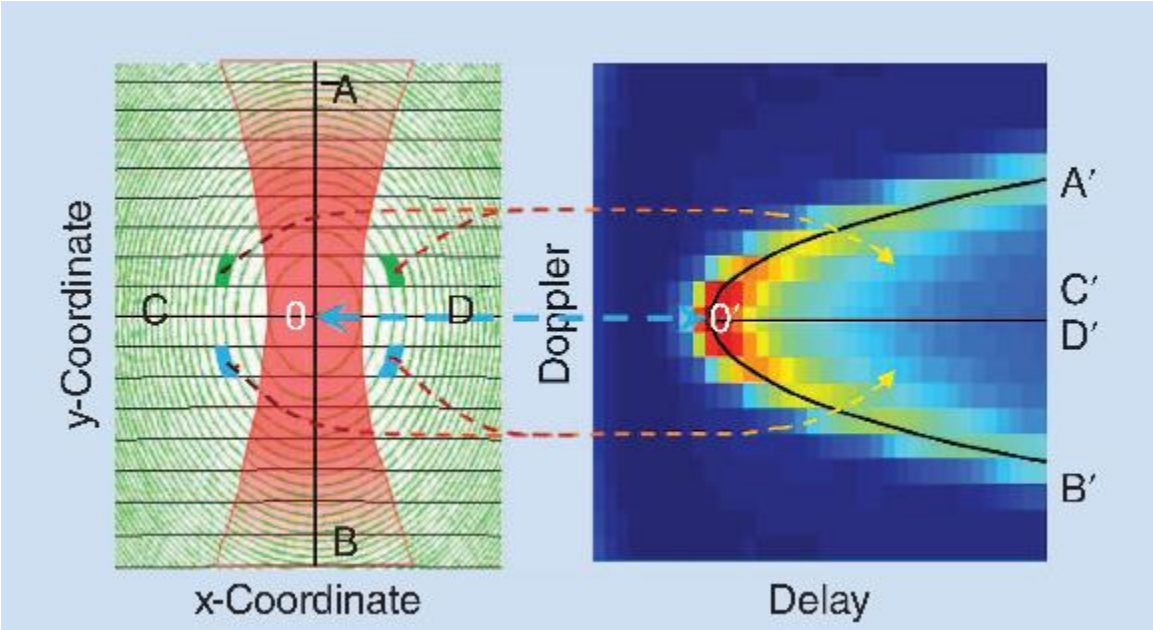

Figure I.2 A concept of DDM related with the surface coordinate system [7]

A GNSS-R bistatic scattering model [22] under the geometric optics (GO) limit of the Kirchhoff approximation (KA) was developed. The average scattered power of DDM $\langle|Y_r(\tau,f)|^2\rangle$ is modeled as follows

$$\langle|Y_r(\tau,f)|^2\rangle = \frac{T_c^2 P_T \lambda^2}{(4\pi)^3} \iint \frac{G_T G_R \left|\chi\left(\tau - \frac{(R_T+R_R)}{c}, f - f_c\right)\right|^2 \sigma^0}{R_T^2 R_R^2} d^2\bar{\rho} \qquad (1.1)$$

where P_T is the power of the transmitted signals, λ is the wavelength of the signals, G_T and G_R are the transmitting and receiving antenna gains, R_T and R_R are the ranges from the transmitter and the receiver to the specular point, χ is the Woodward Ambiguity Function (WAF), τ is the delay of the signal from the transmitter to the receiver, f is the Doppler shift of the reflected signal, f_c

is aimed to compensate the Doppler shift of the signal, σ^0 is the bistatic radar scattering coefficient (BRCS), and $\bar{\rho}$ is the positioning vector of the scattering point.

A small slope approximation (SSA) method was proposed for modeling the BRCS in the strong scattering regime [99] and for the transition from weak to strong diffuse scattering [100]. The KA-GO bistatic scattering model was revisited to include scattering from partially coherent surfaces in [101].

1.4 GNSS-R Signal Calibration and Geophysical Retrieval

Measured DDMs and delay power waveforms of the signals for different ocean wind speed and wave height, made from the UK DMC-1 mission, have demonstrated that when surface roughness increases with the wind speed, then more diffusive incoherent scattering appears in the DDM. This results in a decrease of the peak DDM power and an increase of the slope of the delay power waveform. They lead to two different retrieval approaches to estimate the wind speed, as discussed below.

1.4.1 Waveform-based Approach

For the early airborne ocean wind experiments [20], the cross-correlation power in the reflected signal is measured and the shapes of this power distribution, including both the trailing edge slope and the complete shape of the waveform, are then compared against analytical models based on a geometric optics approach. The wind speed is estimated by obtaining the nonlinear least squares estimate between the measurement and model prediction.

For the UK DMC mission, a similar approach [38] was developed by minimizing the least square cost function of the model-generated delay waveforms under different wind speeds and the measured waveform computed from the raw datasets defined as

$$\varepsilon = \sum_{k}^{k_l} [A_R P_M(U_{10}, k - \tau_M) - P_R(k)] \tag{1.2}$$

where τ_M is delay of the peak of the model waveform, A_R is the magnitude of the model waveform, scaled to fit the actual signal level, U_{10} is wind speed 10 m above the ocean surface, as input into the Elfouhaily et al. [102] wave spectrum, k_l is the number of aligned samples between the detected and model waveforms, P_R is the correlation power delay response of the detected signal waveform, and P_M is the model predicted correlation power delay response.

These approaches do not require absolute calibration of the received power and the retrievals are only dependent on the shape of the waveform. However, a calibrated received power will provide more physical insight into the scattering mechanism for in-depth studies of the ocean surface process and its relation to the wind waves and swell-generated waves.

1.4.2 BRCS-MSS Approach

A BRCS based retrieval approach was developed for sensing the near-surface ocean wind conditions for the UK-DMC experiment. The key idea of this approach can be summarized as: 1) convert the signal-to-noise ratio (SNR) to estimates of the BRCS; 2) correct the measurement bias and scale all BRCS estimates to achieve consistency with theoretical and empirical L-band scattering results; 3) general model prediction curves of the BRCS and use them to estimate the surface mss; 4) estimate the near-surface wind speed using a linear wind–wave relationship [43].

Due to calibration errors, it is suspected that the UK-DMC measurements of NBRCS contain a bias. The Elfouhaily et al. wave spectrum [102], integrated to the L-band cutoff as proposed in [19], and the wind inversion formula proposed by Katzberg et al. in [24] were applied to calculate the bias in the observations. This predicts a negative bias of −1.8 dB and −1.3 dB, respectively, for the two approaches. After correcting the bias in all BRCS measurements, the resulting mss and wind speed estimates fell within a physically reasonable range of L-band surface scattering. Figure I.3 shows the estimation curves over a range of scattering incident angles and surface slopes. Thus BRCS can then be used to estimate the ocean roughness mss.

The final step in the estimation process is to estimate the near-surface wind speed using a linear wind–wave relationship, for which the slope was determined empirically by minimizing the root mean square difference (RMSD) between the estimated wind speeds and in situ national data buoy center (NDBC) ocean buoy wind speeds. The retrieved wind speed error is 1.5 m/s, 1.9 m/s, and 2.2 m/s for measurements taken under wind conditions below 5 m/s, from 5 to 10 m/s, and above 10 m/s, respectively.

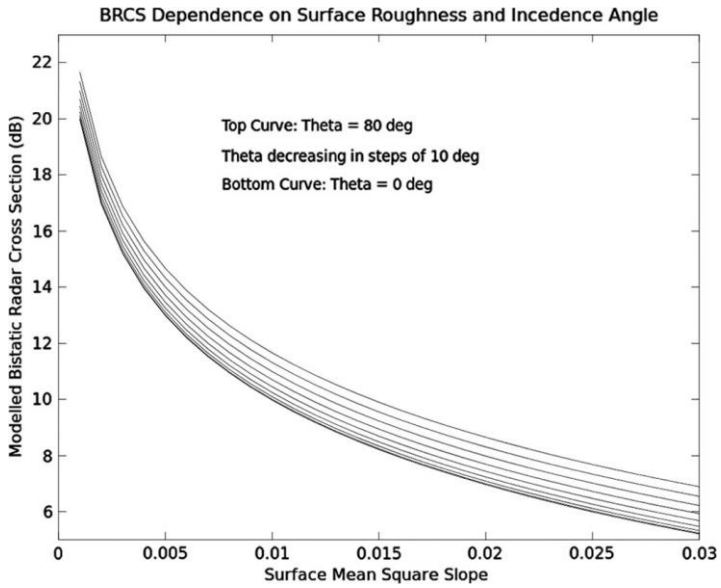

Figure I.3 Changes in the BRCS as a function of surface MSS and incidence angle [43]

1.4.3 Average BRCS-based Empirical Approach

The TDS-1 mission uses the average bistatic radar cross section (BRCS) to retrieve the wind speed [103], with an assumption that BRCS is constant over the glistening zone. The averaged BRCS measurements are collocated with the European Centre for Medium-range Weather Forecasts (ECMWF) wind for generating a geophysical modeling function (GMF), as shown in Figure I.4. TDS-1 wind is retrieved using this empirical GMF. TDS-1 wind differences with ECMWF result in an RMSE and bias of−0.33 and 2.77 m/s, while the ASCAT winds show an RMSE and bias of 0.25 and 2.31 m/s, respectively.

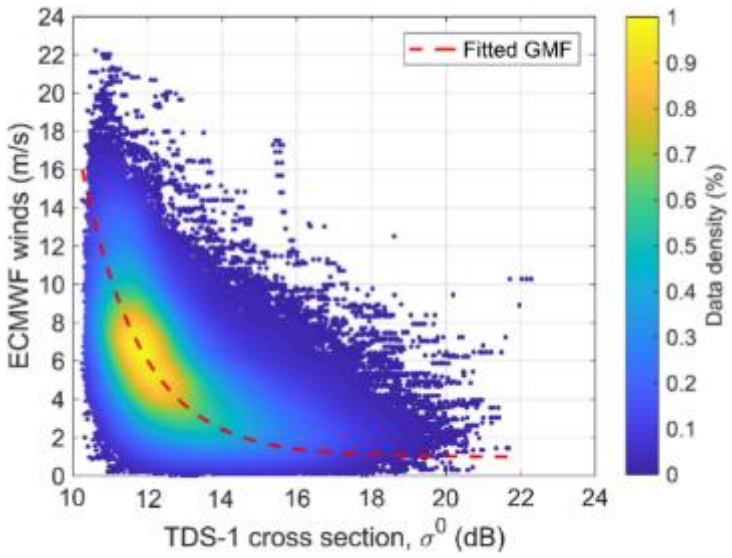

Figure I.4 TDS-1-derived BRCS with SNRs>0 dB versus collocated ECMWF wind speed for the training dataset. The fitted GMF of the form is shown with the red dashed line [103]

1.4.4 NBRCS-based Empirical Approach

For the NASA CYGNSS mission, individual bins of the DDM are measured in raw and uncalibrated units referred to as “counts”. These counts are linearly related to the total signal power processed by the DDM Instrument (DDMI). The signal components include the reflected GPS signal, the thermal emission by the Earth, the noise generated by the DDMI, and possible radio frequency interference (RFI) signals from other satellite navigation systems. The power in the total signal is the product of all the input signals multiplied by the total gain of the DDMI receiver [104].

The Level 1a (L1a) calibration converts each bin in the Level 0 DDM from raw counts to units of watts using open ocean calibration, blackbody calibration, and routine calibration. Then the CYGNSS Level 1b (L1b) calibration generates two data products associated with each L1a DDM: 1) a bin-by-bin calculation of the surface BRCS σ and 2) bin-by-bin values of the effective scattering areas. The two intermediate variables are used to compute the Level 1 data product: normalized bistatic radar cross section (NBRCS), as scattering cross section per meter squared [104], [105].

Geophysical modeling functions (GMFs) are then empirically derived from the CYGNSS observables which are nearly coincident with independent estimates of the 10-m-referenced ocean surface wind speed (U10). Two different Level 1 observables are used: NBRCS σo and the leading edge slope (LES). Two different sources of “ground truth” wind speed are considered: U10 from the numerical weather prediction (NWP) models and measurements by the NOAA P-3 hurricane hunter during eyewall penetrations of major hurricanes. The two wind speeds are used for different sea state conditions: fully developed sea (FDS) and young sea/limited fetch (YSLF) conditions in hurricanes, respectively. By pairing different observables with different sea state conditions, four empirical GMFs are derived, including DDMA-FDS, DDMA-YSLF, LES-FDS, and LES-YSLF

[106]. The former two GMFs are shown in Figure I.5. It has to be noted that these GMFs have a second-dimensional dependence on the specular incidence angle, because CYGNSS makes measurement over all incident angles.

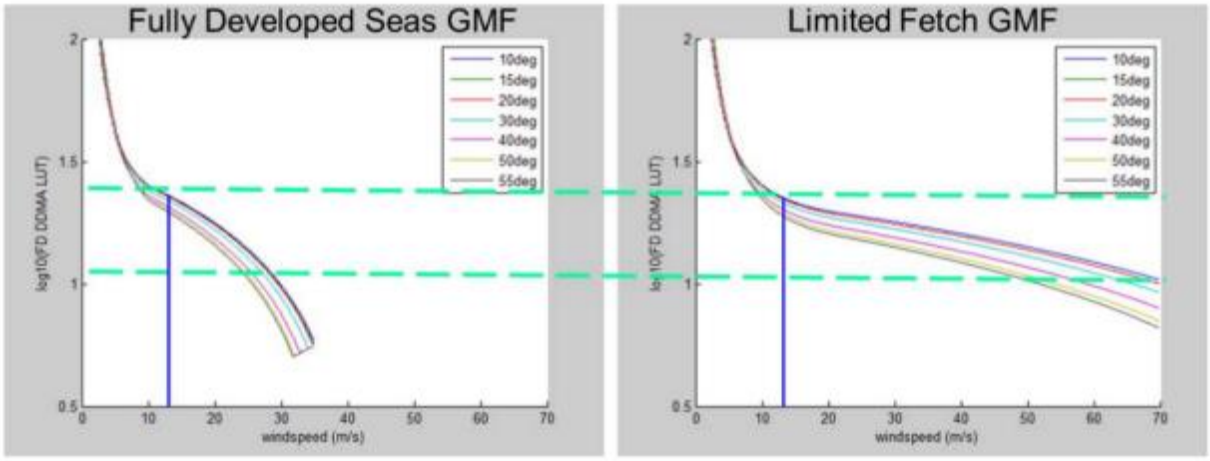

Figure I.5 GMFs appropriate for (left) fully-developed sea (FDS) and (right) young sea/limited fetch (YSLF) conditions in hurricanes [106]

For small errors in the Level 1 NBRCS observable, the corresponding wind speed retrieval error can be estimated by linearizing the GMF, given as

$$\varepsilon_{Obs}(u_{10}) = \left|\frac{d\mathrm{Obs}}{du_{10}}\right|^{-1} \varepsilon(\mathrm{Obs}) \tag{1.3}$$

It is noted that: 1) at low wind speeds below 5–10 m/s, the slope of the GMF is very steep and the component of wind speed retrieval error that is dependent on Level 1 observable error is expected to be low; 2) while for higher wind speeds, the slope decreases markedly, thus the component of wind speed error due to measurement error will be much higher. This dependence is stronger for the YSLF condition in hurricanes [106]. This indicate that in the regime of high wind speed, the calibration quality of Level 1 observable is extremely important to the accuracy of wind speed retrieval [107].

1.5 Challenges in GNSS-R Engineering Calibration

1.5.1 CYGNSS L1b Calibration Error Analysis

The primary correction terms in the CYGNSS L1b calibration include the transmit power P_T, transmit antenna gain G_T, receive antenna gain pattern G_R, and the transmit path loss. The former three terms need to be precisely and accurately characterized. Table I-2 summarizes the CYGNSS L1b calibration algorithm errors [104]. Besides the L1a error team, obviously the errors in the GPS EIRP (defined as the product of transmit power and antenna gain) and CYGNSS receiver antenna gain are the major error sources existing in the L1b calibration [105]. Detailed analysis of the two errors, as the main focus of this dissertation, are discussed in the next two sub-sections.

Table I-2 CYGNSS L1b calibration algorithm errors (in decibel) [104]

Error Term	L1b error, dB (Low winds, < 20 m/s)	L1b error, dB (High winds, > 20 m/s)	Comment
$\boldsymbol{E(P_g)}$	0.50	0.23	L1a calibration error
$\boldsymbol{E(L_{a12})}$	0.04	0.04	Atmospheric modeling error
$\boldsymbol{E(R_R) + E(R_T)}$	0.01	0.01	Total range error
$\boldsymbol{E(P_T) + E(G_T)}$	0.40	0.40	GPS transmitter EIRP error
$\boldsymbol{E(G_R)}$	0.43	0.43	Receiver antenna gain error
$\boldsymbol{E(A)}$	0.20	0.20	Effective scattering area error
Margin	0.20	0.20	
Total L1b error	0.82	0.70	

1.5.2 Uncertainty of GPS Transmit Power

Current operational GPS satellites have 4 different block types of SVs, including 8 IIR, 7 IIR-M and 12 IIF, and 4 III. Among these, the IIR, IIR-M, and III SVs were built by Lockheed Martin and the IIF SVs were built by Boeing. Differences in the design and manufacturing of the SVs and, in particular, in the transmitted power and transmit antenna patterns introduce corresponding differences in the GPS EIRP, which, if not properly accounted for, increase the uncertainty of the measurement.

One primary determiner of EIRP is the GPS transmit power. According to GPS specifications, the power referenced to the transmit antenna input port is at least 14.3 dBW (27 watts). However, typical GPS satellites broadcast 2 to 4 dB more power than that value [2]. Previous studies show that there are differences in the GPS transmit power of individual IIR block type satellites [108]. Secondly, and more importantly, a flex power mode of the Block IIR-M and IIF GPS satellites was developed and implemented to redistribute the transmit power between the individual signal components of the C/A, P(Y), and M codes for increased protection against jamming in certain regions [109]. On February 7th and 8th, 2017, 7 active IIR-M satellites performed a commanded redistribution of transmit power from M-code to C/A code and P(Y) code [110] [111]. From January 27, 2017 to Feb 13, 2020, Block IIF GPS satellites have implemented a geographically driven flex power mode, which enables a ~ 2.5 dB increase and decrease in the L1 C/A code's power with every orbit [109], [112]. This flex power mode was simultaneously observed by a local GPS constellation power monitor (GCPM) system [113], [114] and a local GPS Continuously Operating Reference Station (CORS) by NOAA, as shown in Figure I.6. The carrier-to-noise ratio (C/N_0) has increased more than 2 dB for both systems. The difference between the C/N_0 levels is caused by the different configurations of the two GPS receivers,

including the receiver system gain, the setting of automatic gain control (AGC), etc. The significant power increase and decrease over several seconds repeats at the same geographical location over consecutive days.

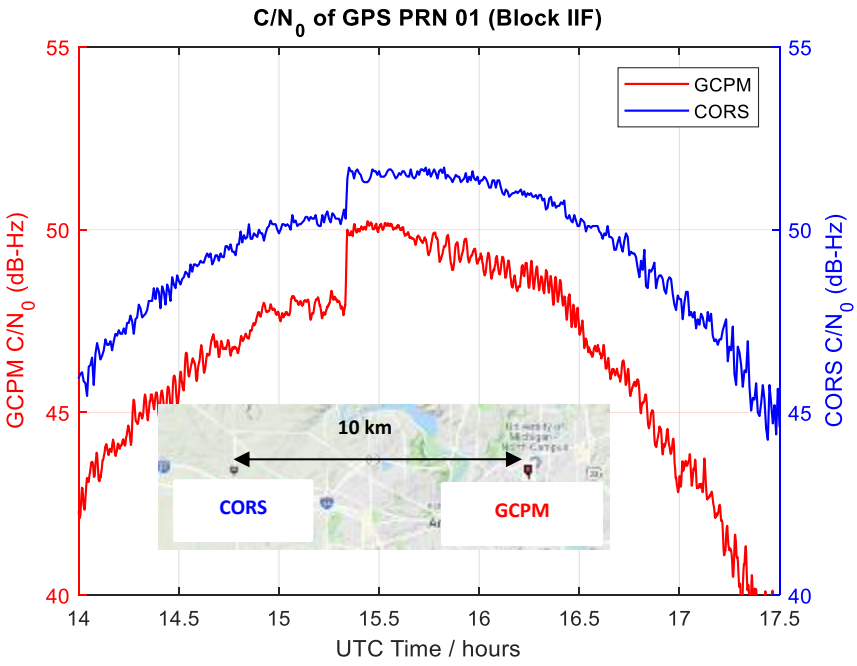

Figure I.6 Flex power of GPS PRN 1 observed by two independent GPS receivers

Independent measurements made by DLR using a high gain dish antenna also demonstrates the geographically driven flex power mode [109]. The ground tracks of 10 GPS Block IIF satellites with increased power (~2.5 dB) for C/A code are shown in Figure I.7.

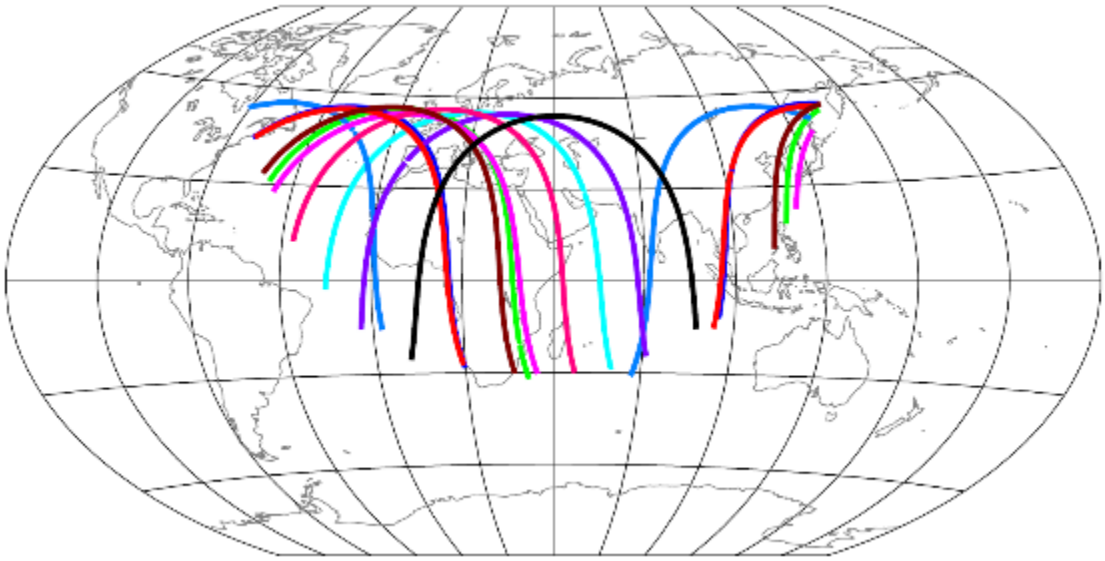

Figure I.7 Ground tracks of GPS Block IIF satellites with increased power for C/A code on June 2, 2018 [109]

1.5.3 Uncertainty of GPS Transmit Antenna Gain

The second primary determiner of EIRP is the transmit antenna gain. The gain is defined as the product of the directivity and the gain correction factor (GCF). However, only the 20 antenna patterns of block type 12 IIR and 8 IIR-M satellites have been published in [115], while those of 12 IIF and 4 III satellites have not been publicly released. The published pre-launch measured antenna patterns are not sufficient for the CYGNSS Level 1 calibration because: 1) the on-orbit GPS transmit antenna gain patterns are known to differ from the pre-launch measured patterns, as the pre-launch measurements were not made while mounted on the flight space vehicle. This would result in pattern distortions as the antenna interacted with the spacecraft and additional avionics present on the same face as the GPS transmit antenna; 2) the resolution of the published patterns is low, 2 degrees in off-boresight angle and 10 degrees in around-boresight angle; 3) the azimuthal asymmetry of GPS antenna gain brings additional error if using an off-boresight azimuthal averaged estimate or if not properly corrected for spacecraft yaw attitude maneuvers [116], [117].

The limited knowledge and possible measurement error of the directivity reduce confidence in the estimate of antenna gain and, thus, the GPS EIRP.

An absolute calibration algorithm would require replacement of simple off-boresight models with full GPS antenna pattern estimates and GPS satellite yaw state modelling for each transmitter. It is extremely difficult to estimate the full pattern using limited ground-based GPS receivers. Also, knowledge of the GPS satellite orientation is complicated by its recurring yaw maneuvers. It is possible but would be rather cumbersome to implement and would increase data latency in order to obtain the necessary GPS satellite yaw states.

1.5.4 Uncertainty of CYGNSS Receiver Gain Pattern

Prior to launch, the gain patterns of the CYGNSS nadir antennas were measured. However, modeling using gain pattern simulation tools and EM chamber measurements show that the solar panels have a significant impact on the observatory antenna gain patterns. The individual pattern measurements were adjusted using a constant gain factor based on measured differences. However, this constant gain scaling is overly simplistic because there is potentially significant variability in the exact deployed position of the solar panels from repeated prelaunch panel deployment tests Therefore, a correction to the receiver antenna gain pattern was derived using anomalies in the NBRCS observations and it was applied as part of the V2.1 Level 1 calibration algorithm [105]. However, it has been demonstrated that the error in wind speeds retrieved from GNSS-R observations is strongly correlated with the significant wave height (SWH) of the ocean surface [118]. Hence, NBRCS anomaly is not the optimal parameter suitable for empirical calibration. It is desirable to take into account the sea state influence, especially the non-local swell contribution

to the ocean surface roughness, to derive a reference NBRCS for precise and accurate calibration of CYGNSS receiver antenna gain pattern.

1.6 Overview of the Dissertation

The objective of this dissertation is to calibrate and mitigate the uncertainties which exist in the estimate of the GPS EIRP and CYGNSS receiver antenna gains.

This dissertation include four major components:

1) Measuring GPS average transmit power with a ground based system;

2) Measuring GPS transmit antenna gain with a spaceborne antenna range;

3) Measuring GPS EIRP in real-time with a spaceborne system;

4) Level 1 end-to-end calibration using mss inter-comparisons.

CHAPTER II

Measuring GPS Average Transmit Power with a Ground Based System

2.1 Introduction

The primary determiner of EIRP is the GPS transmit power. According to GPS specifications, the power referenced to the transmit antenna input port is 14.3 dBW (27 watts). However, typical GPS satellites broadcast 2 to 4 dB more power than that value [2]. Previous studies show that there are differences in the GPS transmit power of individual IIR block type satellites [108]. An independent study using the DLR's German Space Operations Center (GSOC)'s high gain dish antenna examined the differences in transmit power within the GPS constellation [119]. If not properly accounted for, these differences in transmit power can introduce errors into the CYGNSS L1b calibration of NBRCS.

The main goal of this chapter's work is to estimate the effective GPS transmit power (L1 C/A) for each SV. However, there are several main challenges and difficulties: 1). the high expense and time required to use traditional high gain antenna dishes to measure the GPS received power; 2). no high quality absolute power calibration is available for commercial GPS receivers (they usually output only the raw, uncalibrated, counts). A ground-based GPS constellation power monitor (GCPM) system is designed, built, and calibrated to measure the direct GPS L1 C/A signal. A PID thermal controller successfully stabilizes the system temperature over the long term. Radiometric calibration and single PRN calibration are performed to accurately convert the raw

counts reported by the commercial receiver into power in watts. The GCPM received power is highly repeatable and has been verified with DLR/GSOC's independent measurements.

Combined with the baseline antenna pattern [115], an optimization algorithm determines the transmit power of GPS L1 C/A-code by minimizing a cost function based on the difference between an engineering forward model prediction and the measurement of received power. In this way, we determine the effective transmit power of the 32 GPS satellites. Updated values for transmit power have been successfully applied to CYGNSS L1b calibration and found to significantly reduce the PRN dependence of CYGNSS L1 and L2 data products.

Much of the work presented in this chapter is derived from [113], [114].

2.2 Forward Model and Optimal Search Algorithm

The GPS Transmitter Receiver (GTR) coordinate systems are shown in Figure II.1. For the GPS transmitter, $+X_T$ points in the orbital velocity direction, $+Z_T$ points to nadir; for the receiver, $+X_R$ points to North, $+Z_R$ points to the zenith. θ_T, ϕ_T and θ_R, ϕ_R are the off-boresight angle and around-boresight angle of the transmitter and the receiver, respectively.

Measurement of the direct GPS signal is described by a forward model based on the Friis transmission equation [6]:

$$P_R = \frac{[P_T G_T(\theta_T, \phi_T)]}{4\pi R^2 L_a}\left(\frac{\lambda^2}{4\pi}\right) G_R(\theta_R, \phi_R) \tag{2.1}$$

where P_R is the received power of the direct GPS signal, P_T is the GPS transmit power, G_T is the antenna gain of the GPS transmitter, R is the distance between the transmitter and the receiver, λ is the wavelength for GPS L1 signals, L_a is the atmospheric loss dominated by the attenuation by oxygen at the GPS L1 frequency [4], and G_R is the gain of the receiver antenna. The amplifier gain

of the receiver system is not included because the received power P_R is calibrated with reference to the RF input of the GCPM box, as explained in Section 2.4.

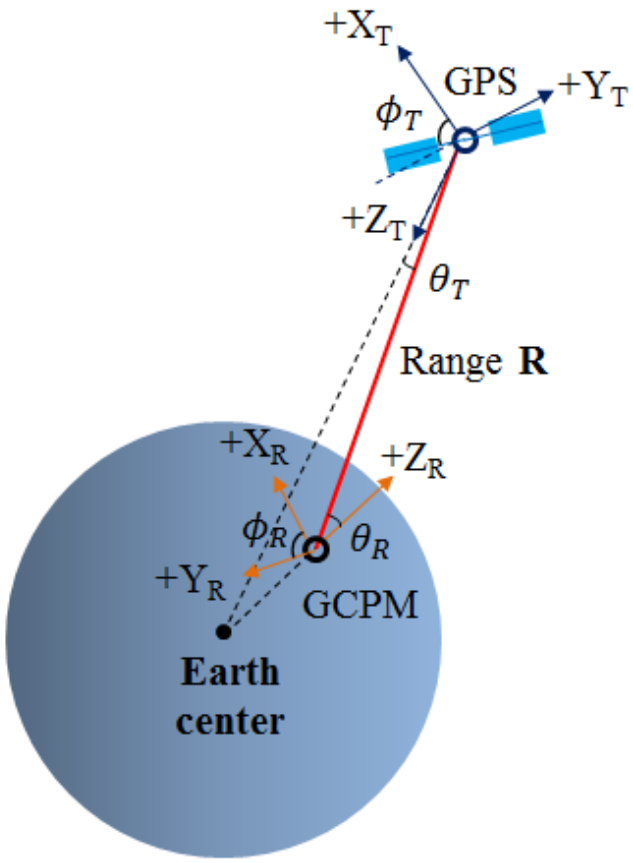

Figure II.1 Definition of GPS Transmitter Receiver (GTR) coordinate systems

In the antenna panel coordinate system, θ is the angle across the face of the antenna panel and ϕ is the angle that is counter-clockwise around the antenna panel boresight axis [115]. If yaw steering of the satellite is considered, a correction should be applied to map ϕ in the transmitter coordinate system into the antenna panel coordinate system [120].

To simulate the received power, the transmit power and antenna gain are based on the look-up table (LUT) of GPS transmit power and 5th order power series for transmit antenna gain [105]. The gain of the receiver antenna is based on the measured pattern, with more details described in

Subsection 2.3.2 below. The distance R, off-boresight angles and around-boresight angles are computed from the position, velocity, time (PVT) of the GPS satellites and the geo-location of the GCPM station. We account for the time dependence of all variables due to the measurement geometry, and use the calibrated P_R to estimate the GPS EIRP.

An optimal search algorithm for transmit power is proposed as follows. Define a cost function as

$$cost(P_T) = \sum_{t=t_1}^{t_N} \left[P_R^{Model}(P_T, t) - P_R^{Meas}(t) \right]^2 \tag{2.2}$$

where $P_R^{Model}(P_T, t)$ is the modeled received power, $P_R^{Meas}(t)$ is the measured received power, and the summation of the square of difference is over the time from t_1 to t_N, which is the effective measurement time of a GPS satellite overpass of the GCPM station located in Ann Arbor, Michigan, USA (latitude = 42.2808° N, longitude = 83.7430° W) filtered by a 20 degrees elevation mask with the consideration of minimizing the local environment multipath effect.

The cost function is used to maximize the benefits of the additional measurements using the GCPM system and to solve for a more reliable estimate of GPS transmit power from an over-constrained dataset.

By varying the transmit power P_T, we are able to minimize the cost function. The power value corresponding to the minimum cost function is selected as the estimated P_T. We are able to determine the GPS transmit power (L1 C/A) for each satellite by averaging 32 days' estimates.

2.3 Design and Implementation

2.3.1 Overview of System Design

The GCPM system was designed and built at the Space Physics Research Laboratory, University of Michigan.

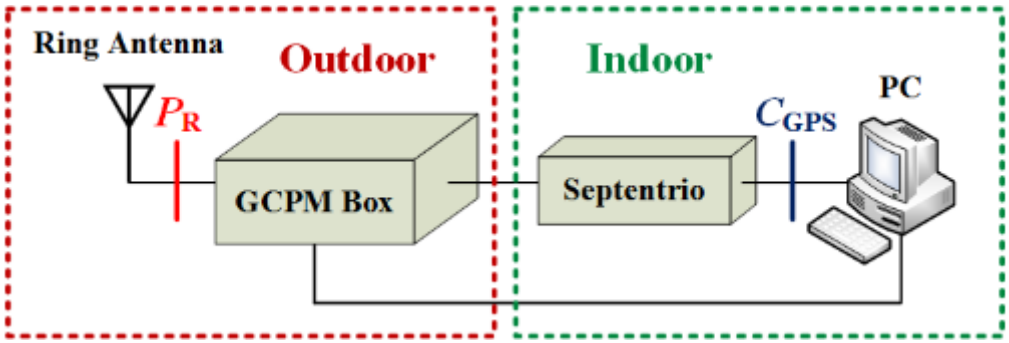

Figure II.2 The measurement setup of the GCPM system

As shown in Figure II.2, the GCPM system includes both outdoor and indoor segments:

1). Outdoor: a passive choke ring antenna is used to receive the direct GPS signal. A thermally controlled, box-enclosed plate containing the cold load, warm load, excess noise source, and LNA are used for stable signal amplification and calibration. As shown in Figure II.3, the receiver antenna and the thermal box are mounted on the roof top of Space Research Building, University of Michigan.

(a) (b)

Figure II.3 GCPM: (a) Location; (b) Antenna and thermally controlled box

2). Indoor: a commercial Septentrio PolaRxS GPS receiver is used to measure the counts C_{GPS}, as the sum of the squared I and Q counts of the prompt correlator, which is proportional to a GPS signal's carrier power. Calibration (discussed in Section 2.4) converts C_{GPS} to the received power P_R in watts. A control and data handling desktop computer is used to: i). control the Septentrio receiver and store the raw measurement data; ii). switch the measurement between external antenna and internal calibration loads; iii). command the proportional–integral–derivative (PID) temperature controller, and measure the temperature of the thermally controlled box.

2.3.2 Receiver Antenna

The receiver antenna is a mast-mounted passive Javad RingAnt-DM antenna, as shown in Figure II.4 (a). The full antenna pattern at the GPS L1 frequency (1.57542 GHz) has been measured at the ElectroScience Laboratory, Ohio State University, as shown in Figure II.4 (b) and (c). The black circles correspond to zero degrees of elevation angle. The right hand circular polarization

(RHCP) gain is much higher than the left hand circular polarization (LHCP) gain. The RHCP pattern is azimuthally symmetric and minimizes the differences at different observing azimuth angles. This demonstrates that the receiver antenna is well designed and manufactured to receive the GPS direct signal. A surge protector is applied to avoid lightning spike damage.

(a)

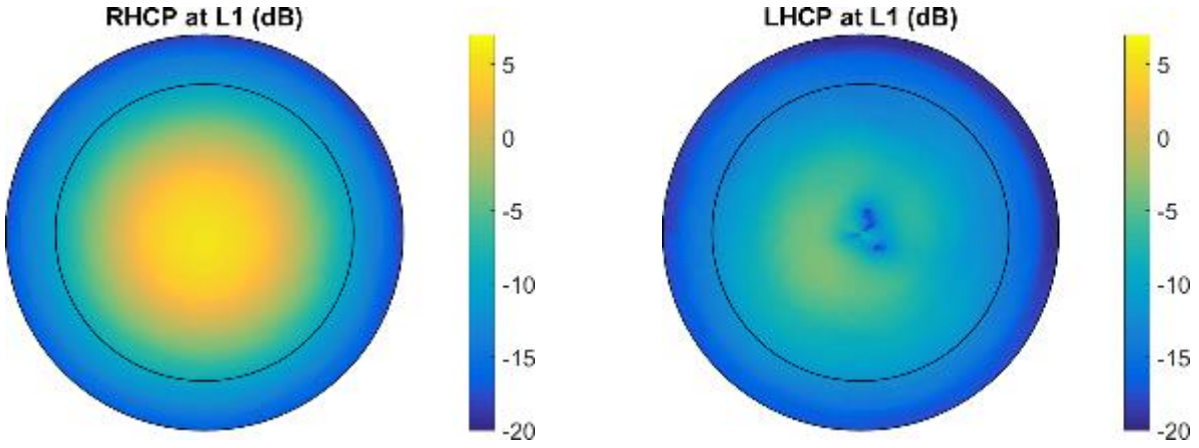

(b) (c)

Figure II.4 Javad RingAnt-DM antenna: (a). Side view; (b). RHCP pattern at GPS L1 frequency; (c). LHCP pattern at GPS L1 frequency

2.3.3 Calibration Subsystem and LNA

A functional block diagram of the calibration subsystem and low noise amplifier (LNA) is shown in Figure II.5. The received GPS signal flows into bandpass filter (BPF) 1 (50 MHz bandwidth) and the directional coupler, then is amplified by the LNA with ~34 dB gain, and finally is filtered by BPF 2 (5 MHz bandwidth). The measured gain of the entire circuit from input port to output port is 27.92 dB, after accounting for all insertion loss of the circuit components and the cables. The system bandwidth is 5 MHz centered at 1.57542 GHz (GPS L1).

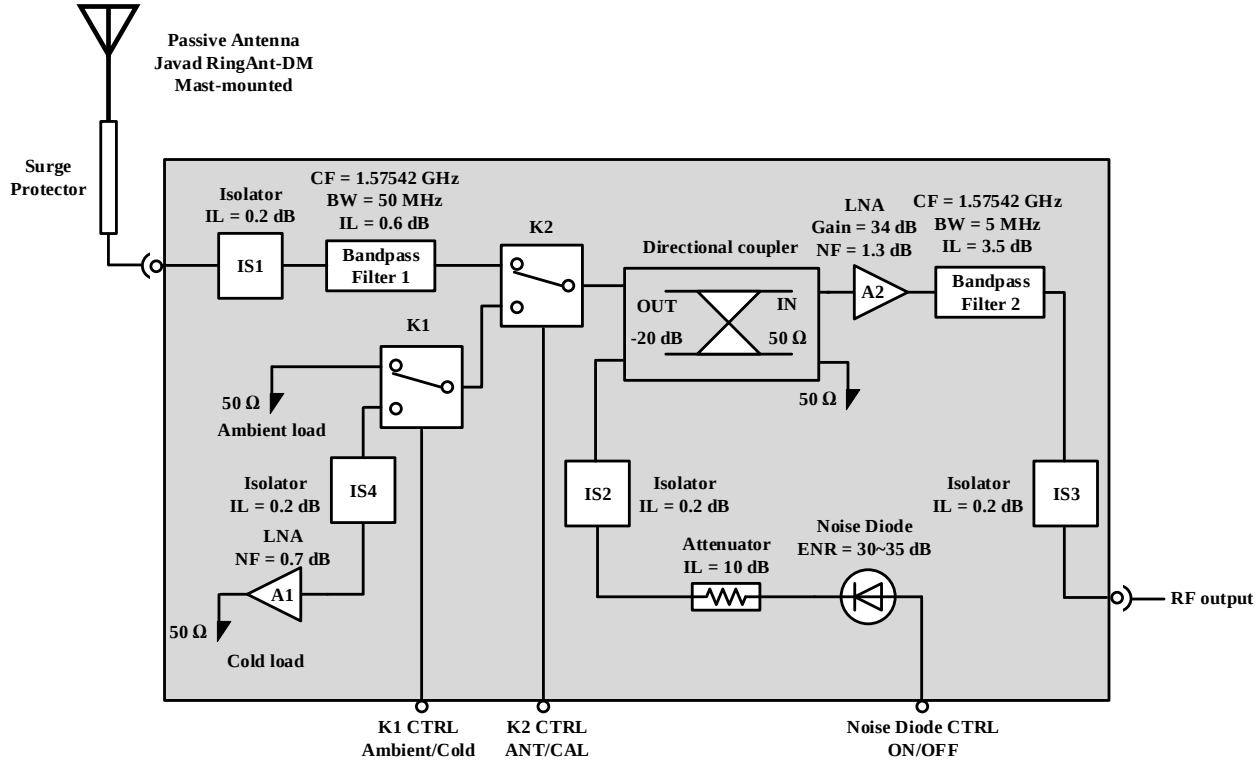

Figure II.5 Functional block diagram of calibration subsystem and LNA

The ambient load, cold load (reverse LNA) and noise diode are designed to provide stable radiometric calibration references. Note that the noise diode's power level is attenuated by a 10 dB attenuator and a 20 dB directional coupler.

K1 is used to switch the ambient load and cold load, and K2 is used to switch the external antenna measurement and internal calibration load. The noise diode can be turned ON/OFF by the control signal.

Table II-1 gives more detailed information about the circuit elements, including part number, noise figure (NF) and gain (negative values for gain denote insertion loss).

Table II-1 Circuit element summary

	Part number	Gain (dB)	NF (dB)	Note
LNA A1	Mini-Circuits ZX60-P162LN+	~18.7*	~ 0.7*	Used as cold load
LNA A2	RF-Lambda RLNA11M01G	34* (typical)	1.3* (typical)	Amplifier
BPF1	Reactel 6c7-1575.42-50S11	-0.6**	/	50 MHz bandwidth
BPF2	Reactel 5C7-1575.42-5S21	-3.5*	/	5 MHz bandwidth
Noise diode	Noisecom NC3203	/	ENR 30~35*	/
Directional coupler	Pasternack PE2201-20	-0.2*	/	-19.4 dB* coupling
Attenuator	Mini-Circuits VAT-10+	-10*	/	/
Isolator	UTE Microwave CT2002OT	-0.2**	0.2*	/

*: values from datasheet; **: values measured by vector network analyzer (VNA)

2.3.4 Thermally Controlled Box

The thermally controlled box is shown in Figure II.6. It has a solar reflective exterior white coating to ensure a more stable temperature.

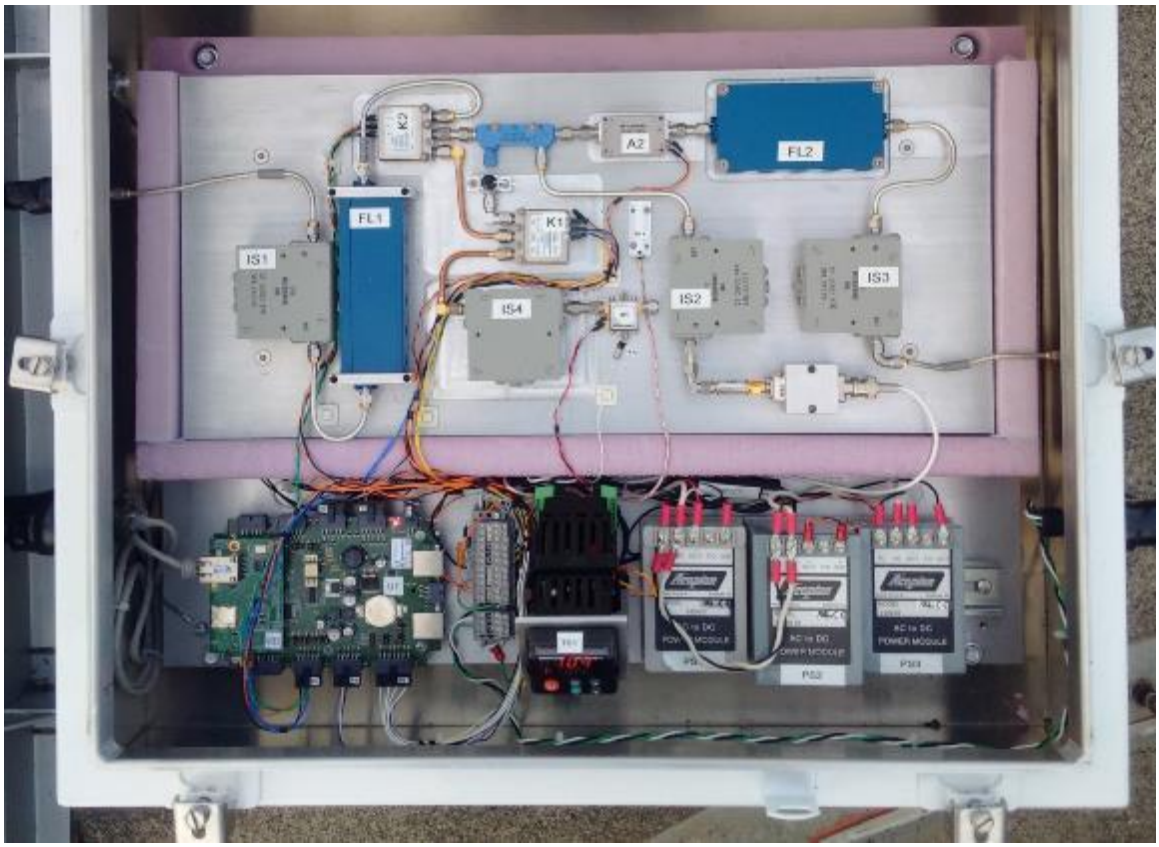

Figure II.6 Picture of the GCPM thermally controlled box

The upper part is the calibration subsystem and LNA implemented on a thermal plate. Temperature is stabilized by a PID controller. The set point temperature is 50 °C to ensure stable LNA gain and system noise figure for all expected ambient temperatures. Three thermistor sensors are used to measure the temperatures of the ambient load, the thermal plate, and the base plate in the GCPM box.

The lower part (from left to the right) includes the Rabbit single board computer (SBC), PID temperature controller, and power supplies. The SBC is used to: 1) communicate with the PC; 2) control the calibration states by control (CTRL) signals to K1, K2 and noise diode; 3). command the PID controller; and 4) measure the temperatures via thermistor sensors.

2.3.5 Septentrio GPS Receiver

A Septentrio PolaRxS ultra-low noise multi-frequency, multi-constellation GPS receiver is used. The PolaRxS has a sufficient dynamic range. The automatic gain control (AGC) is turned off and the system gain is fixed to 38 dB (see the radiometric calibration in Section 2.4).

The PolaRxS measures power in raw counts. It provides two types of power measurement: the total system noise power (baseband counts $C^B_{Blackbody}$) and the power in individual (PRN) GPS satellite L1 transmissions (post-correlated counts C_{GPS}). The output data rate is set to 1 Hz.

2.4 Calibration

2.4.1 Radiometric Calibration

An external liquid nitrogen load (Maury noise calibration system MT7000) was connected to the input port of the GCPM calibration subsystem and LNA. It is used to calibrate the brightness temperatures of the internal cold load and noise diode.

There are 6 calibration states: EXT LN2 Start, INT Cold, INT Cold+ND, INT Ambient, INT Ambient+ND, EXT LN2 End. (EXT is external, INT is internal, ND is noise diode, and LN2 is liquid nitrogen). Each state is measured for 0.5 hour; one full calibration routine requires 3 hours. The calibration routine is performed 3 times in total. The averaged baseband counts $C^B_{Blackbody}$ vs. the time of calibration state is shown in Figure II.7.

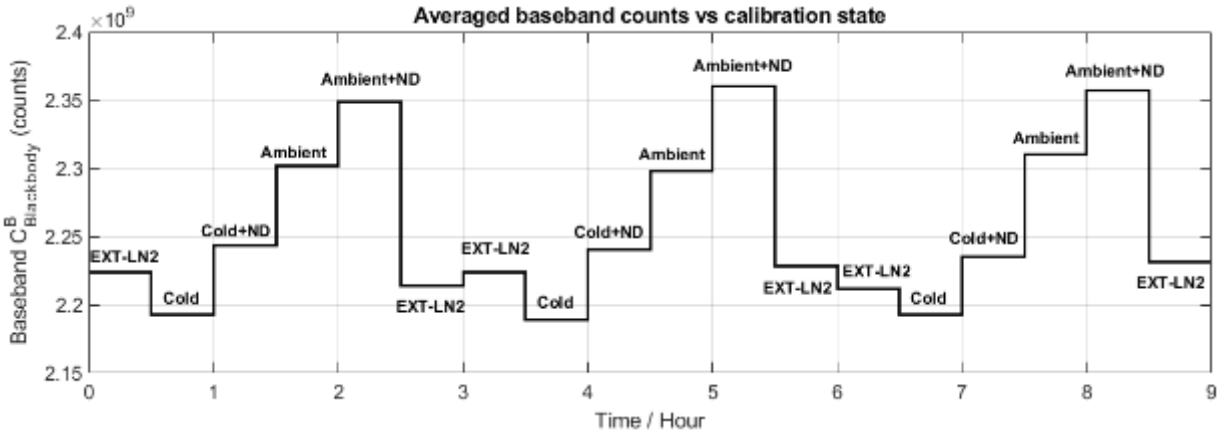

Figure II.7 Averaged baseband counts vs. time of calibration state

The calibrated equivalent brightness temperatures of the internal and external loads are given in Table II-2. The brightness temperatures (Tbs) of the external LN2 (80.5 K) and the internal ambient load (323.15 K) are used as references. Note the calibration of brightness temperature is referenced at the input of K2, so the equivalent Tb of the external LN2 is 120.77 K. The calibrated brightness temperatures of the internal cold load and excess noise diode are 59.39 K and 110.52 K (averaged value), respectively.

Table II-2 Equivalent brightness temperature of noise sources at K2

Noise source	Brightness temperature Tb (K)
External LN2 load	120.77
Internal ambient load	323.15
Internal cold load	59.39
Excess Noise diode [Tb(Ambient+ND) – Tb(Ambient)]	110.87
Excess Noise diode [Tb(Cold+ND) – Tb(Cold)]	110.16

To test system linearity, the output-averaged baseband counts vs. Septentrio gain is plotted in Figure II.8. The gain of the Septentrio receiver is set to a fixed 38 dB to be in the middle of the portion of the dynamic range that is nearly linear.

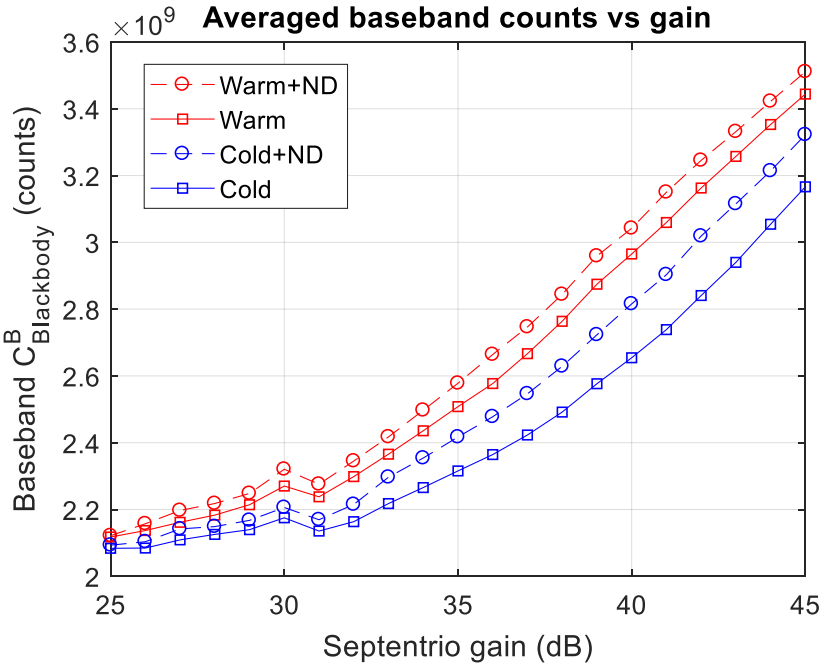

Figure II.8 Averaged baseband counts vs. Septentrio gain

The internal calibration loads can be used to track the system gain. Because of the low baseband sampling rate (1 kHz) of the Septentrio receiver, the internal calibration loads cannot be measured every hour. Currently they are measured monthly to ensure stable system gain and consistent hardware functionality.

2.4.2 Single PRN Calibration

Because the output power of individual (PRN) GPS satellite L1 transmissions is in the form of raw counts C_{GPS}, we need to convert it to the received power P_R in watts. A single PRN

calibration using the CYGNSS GPS signal simulator (GSS) is performed to determine the ratio of total system gain to PRN-specific correlated gain.

The measurement configuration is shown in Figure II.9. A simulated signal from the signal generator (SG) of GSS is reduced to the power level of actual GPS signals by the attenuator in the distribution unit, and then flows into the input port of the GCPM thermally controlled box, the Septentrio receiver, and finally the PC. The settings for system gain and temperature are both the same as those used for external antenna measurements of the direct GPS signal.

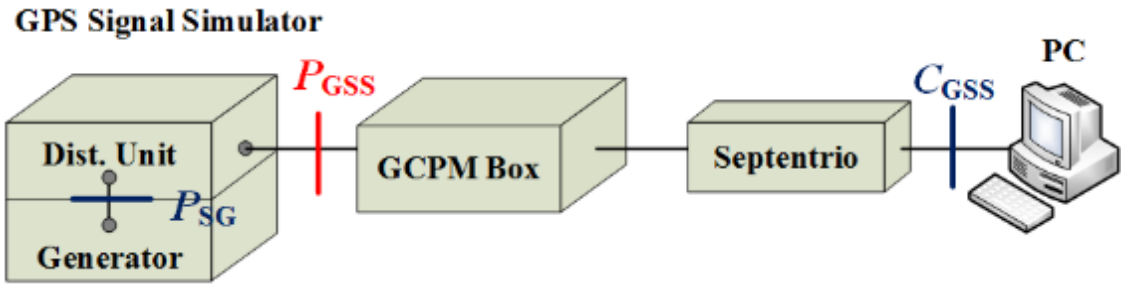

Figure II.9 The measurement setup of the single PRN calibration

The output power of the signal generator P_{SG} is measured by a calibrated power meter and is used to determine the power of the reference signal P_{GSS} at the input port of the GCPM box. The measured output counts of the Septentrio receiver C_{GSS} are plotted vs. P_{GSS} in Figure II.10. The calibration scale factor S_G, is determined as the (power in)/(counts out) slope within the effective dynamic range of the input signal, to be

$$S_G = \frac{P_{GSS}}{C_{GSS}} = 6.10 \times 10^{-21}\ Watt/CT \qquad (2.3)$$

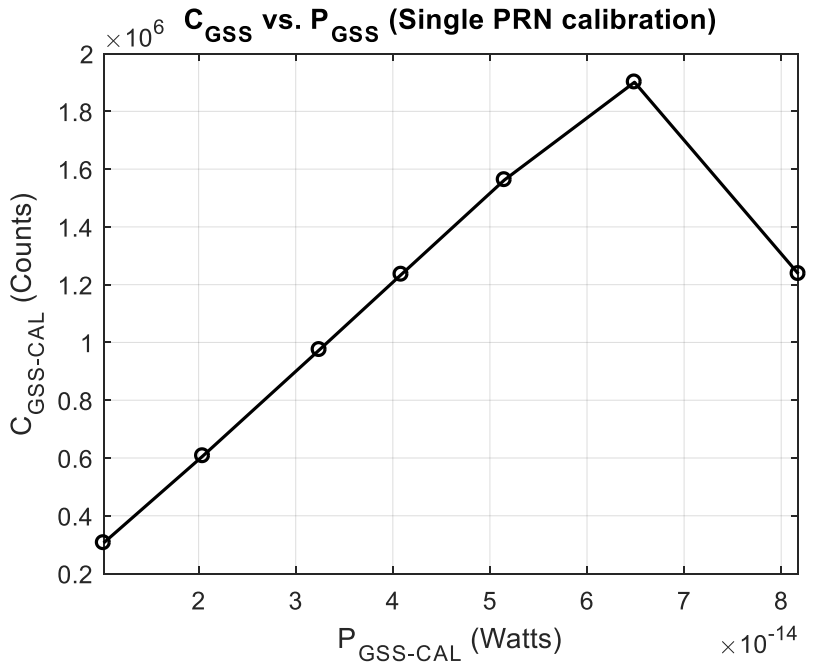

Figure II.10 Post-correlated counts C_{GSS} vs. input power P_{GSS}

The negative slope shows the non-linearity when the input GSS power is too high ($P_{GSS} = -130.87$ dBW). It is probably caused by digitizer overload in the GPS receiver.

The received power is then calibrated using

$$P_R = \mathrm{S}_G C_{GPS} \tag{2.4}$$

where C_{GPS} is the measured post-correlated counts when switched to the external antenna and P_R is the received power referenced to the input port of the GCPM box.

Note that this scaling factor is only applicable to this specific configuration of circuit elements and the current settings of system temperature and receiver gain.

2.5 System Performance and Verification

2.5.1 Stability of Temperature Control

Figure II.11 illustrates the system temperature control over 1 hour. The controller is turned on at ~10 minutes, and then the system starts heating. The temperatures of the ambient load (located on the thermal plate) and thermal plate increase to the set point (50 ℃) within 10 minutes. Because the GCPM box is open, the temperatures vary somewhat with ambient temperature changes. After the GCPM cover is closed and the closed-loop PID temperature controller is activated at ~30 minutes, the temperatures of the ambient load and thermal plate quickly stabilize to the set point temperature. It should be noted that the base plate is not heated and is weakly coupled to the ambient environmental temperature.

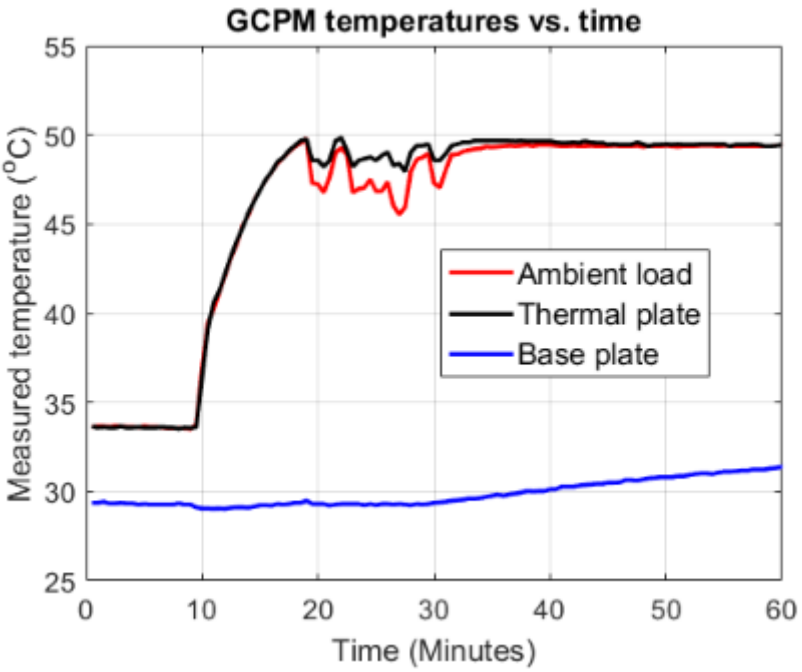

Figure II.11 Measured temperatures with PID controller turned on

Figure II.12 shows long-term measurements over 50 days starting from February 2nd, 2018 with a 10 minute sampling increment. The temperature of the base plate (no thermal control) shows the ambient diurnal variation. In contrast, the temperature of the ambient load has a mean value 49.06 ℃ with standard deviation 0.09 ℃; the temperature of the thermal plate has a mean value 49.17 ℃ with standard deviation 0.08 ℃. The GCPM system clearly shows stable temperature control, resulting in a stable LNA gain and system noise figure.

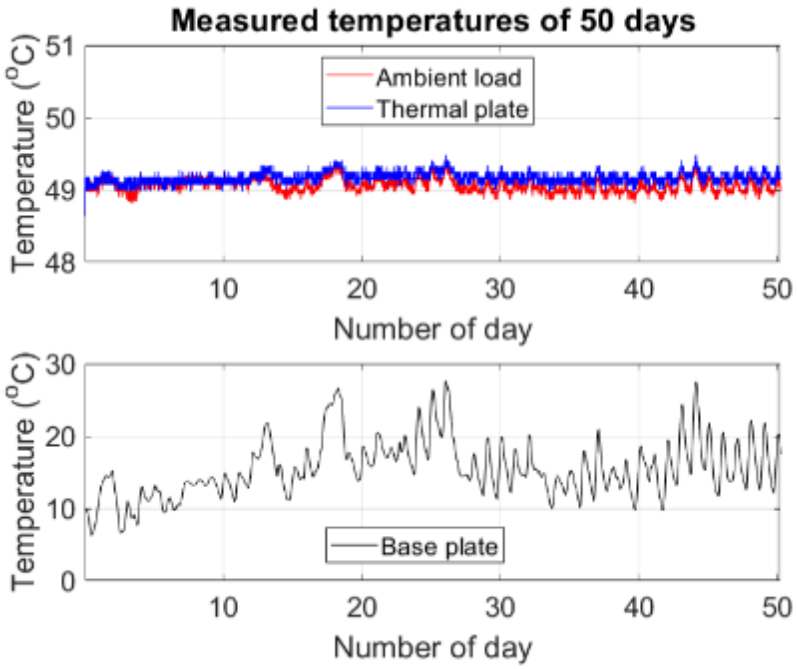

Figure II.12 Long term measured temperatures

2.5.2 Repeatability of Received Power

In Figure II.13, independent measurements on two consecutive days for three different PRNs of IIR, IIR-M and IIF block types are plotted. The timelines are shifted by 4 minutes to account for orbit precession time differences. The received power P_R is referenced to the RF input of the GCPM box based on the single PRN calibration in Subsection 2.4.2. A 60 seconds moving

average is applied. The measured power is very repeatable, including most of the observed fine structures.

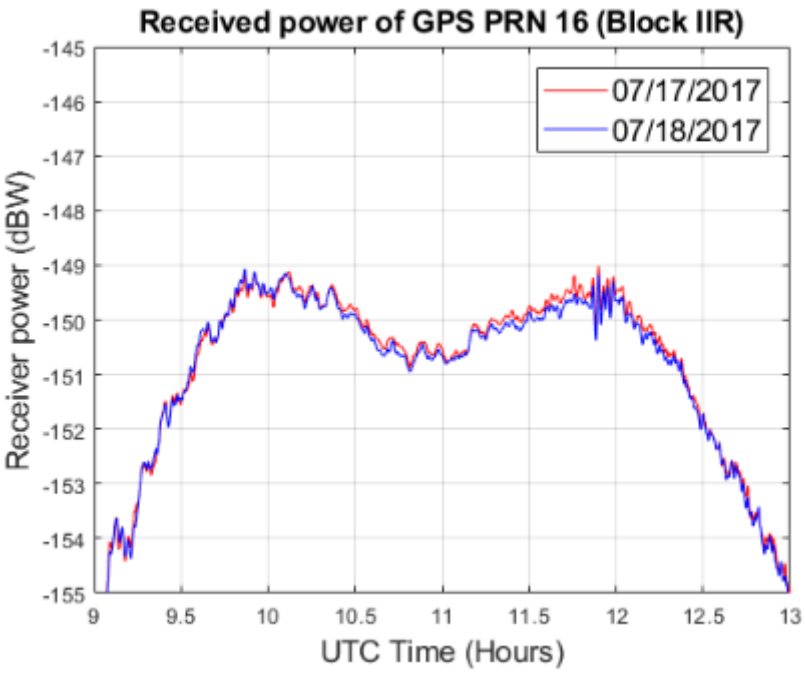

(a)

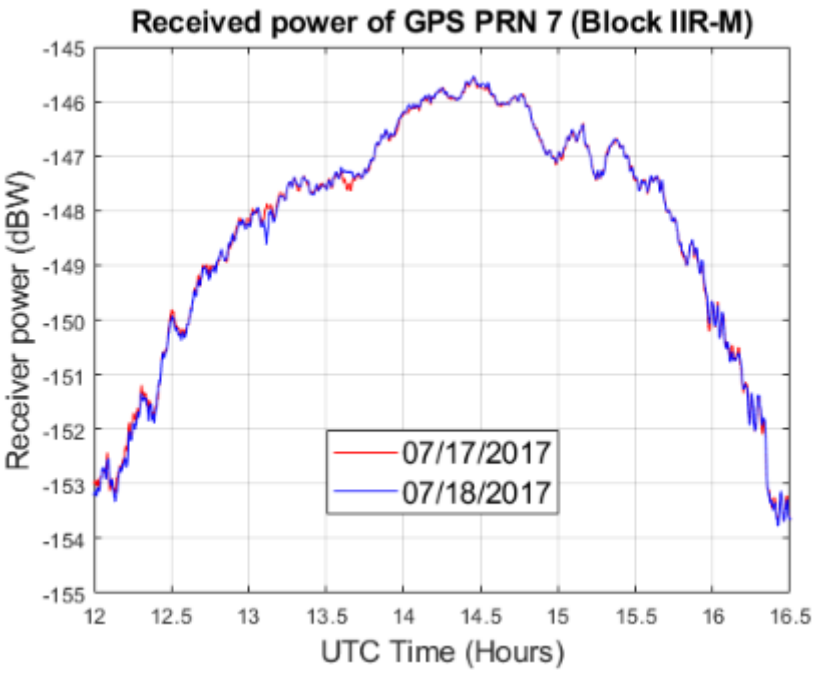

(b)

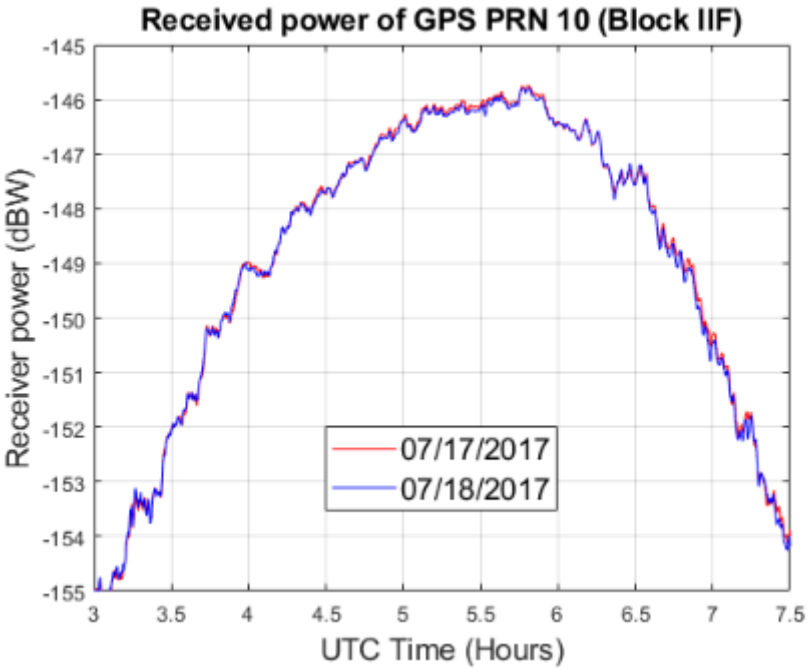

(c)

Figure II.13 Received power P_R: (a). GPS PRN 16 (Block IIR); (b). GPS PRN 7 (Block IIR-M); (c). GPS PRN 10 (Block IIF)

2.5.3 Verification with Independent Measurement

The EIRP measured by the GCPM on July 30th, 2017 is compared with an independent measurement on March 23rd, 2017 by DLR/GSOC using a calibrated 30 m dish antenna with 50 dB L-band gain, as reported in [111].

Figure II.14 shows the measured EIRP ($P_T G_T$) for GPS PRN 29 on July 30th, 2017 after correcting for cable loss, receiver antenna gain and the propagation loss from the calibrated received power P_R. The EIRPs of ascending and descending orbits separate from each other because of the azimuth asymmetry of the antenna gain pattern. The raw data from DLR was processed by applying a -3.0 dB code power relation to the total L1 transmission power (computed using the code power measurement methodology [121] and the power allocation factor given in [111]) and adding a bias correction factor of 0.8 dB. The systematic bias may be caused by the

differences between the hardware and the calibration methods of the two different GPS receiver systems.

The measured EIRPs and the reprocessed DLR EIRPs match quite well. The difference may be caused by systematic calibration errors and/or the different cuts through the obviously non-symmetric satellite antenna pattern. For CYGNSS L1b algorithm, this EIRP bias is a relative error and does not affect the calibration results when the EIRPs are calibrated using a single system, GCPM.

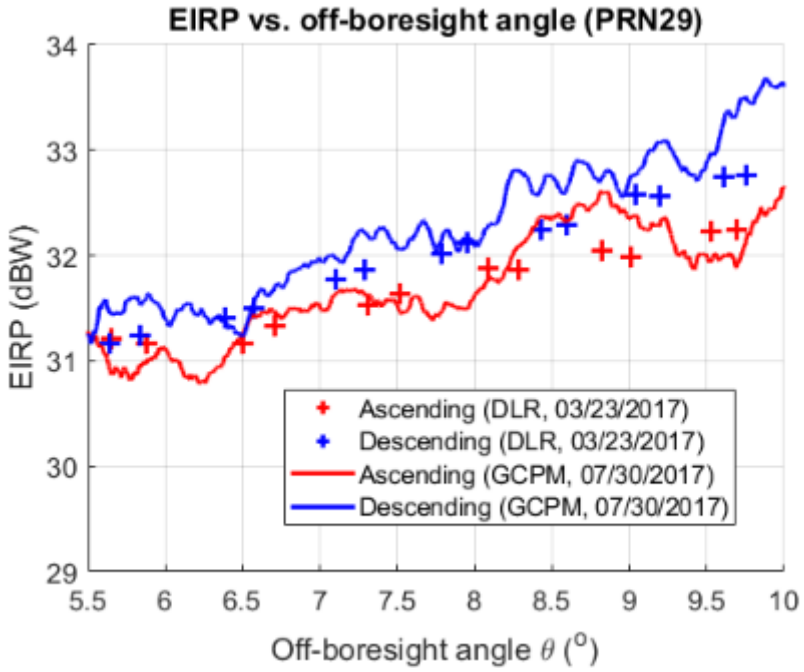

Figure II.14 Comparison of DLR data (03/23/2017) and GCPM measurement (07/30/2018) for GPS PRN 29: EIRP vs. GPS off-boresight angle
(Credit: DLR raw data is provided by Mr. Steffen Thoelert from DLR, Germany)

2.6 Calibration of GPS Transmit Power and EIRP

2.6.1 Calibration of GPS Transmit Power (L1 C/A)

Using the optimal search algorithm described in Section 2.2, an estimate of the GPS transmit power P_T is determined by minimizing the appropriate cost function. By averaging 32 days of estimates of P_T, we determine our best estimate of the GPS transmit power for the entire constellation. The period is from GPS Day 17198 to 17239 except 17202, 17203, 17205, 17215, 17216, 17223, 17227, 17229, 17234, and 17237, of which the data quality was affected by rain. The detailed values of estimated transmit powers are summarized in Table II-3. The results are plotted in Figure II.15. In the figure, the transmit power shows a block-type dependence, and the variation among different GPS transmitters is about 4 dB.

The estimated GPS transmit power has been applied to the CYGNSS L1 calibration for v2.0 data, and been shown by the CYGNSS Cal/Val and Science teams to have successfully reduced the PRN dependence of L1 NBRCS and L2 wind speed calibration [107], [122].

It should be noted that: 1). the estimated power values are indeed an ‘effective transmit power’, as the product of the exact transmit power and the transmit system gain correction factor (GCF). If the readers are interested in the exact transmit power, they need to take into account the GCF in reference [115]; 2). The accuracy of the estimated power values is dependent on the accuracy of the baseline pattern (5th order power series of transmit antenna gain in [105]) used in the forward model simulation. They will be further updated when the full transmit antenna pattern are retrieved using the direct GPS signal measured by the CYGNSS zenith antenna.

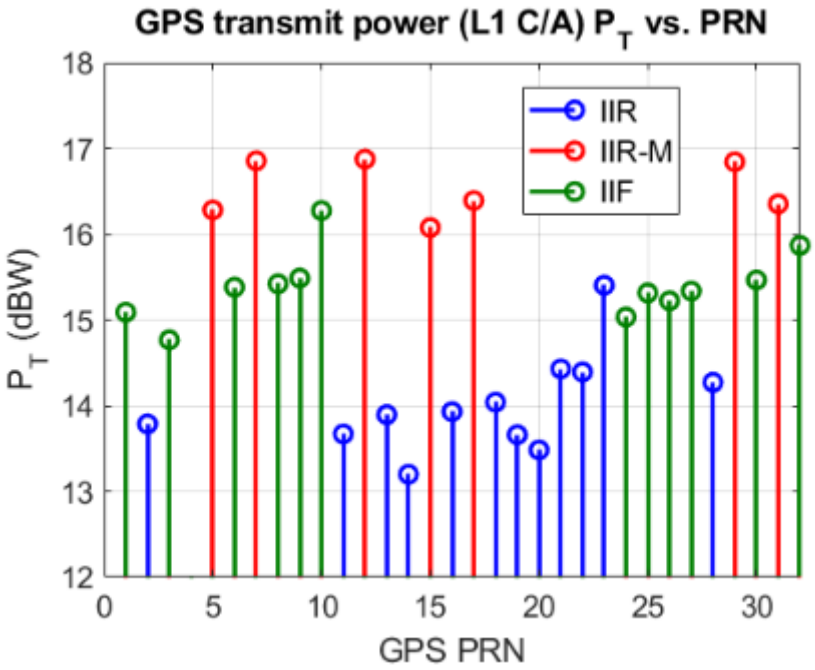

Figure II.15 GPS transmit power (L1 C/A) vs. PRN

Table II-3 GPS transmit power (L1 C/A)

PRN	P_T (dBW)	Block	PRN	P_T (dBW)	Block
1	15.09	IIF	17	16.39	IIR-M
2	13.79	IIR	18	14.04	IIR
3	14.77	IIF	19	13.66	IIR
4	/	/	20	13.48	IIR
5	16.28	IIR-M	21	14.43	IIR
6	15.38	IIF	22	14.39	IIR
7	16.86	IIR-M	23	15.41	IIR
8	15.42	IIF	24	15.03	IIF
9	15.49	IIF	25	15.32	IIF
10	16.28	IIF	26	15.22	IIF
11	13.67	IIR	27	15.34	IIF
12	16.88	IIR-M	28	14.27	IIR
13	13.89	IIR	29	16.84	IIR-M
14	13.20	IIR	30	15.47	IIF
15	16.08	IIR-M	31	16.35	IIR-M
16	13.93	IIR	32	15.87	IIF

2.6.2 Calibration of EIRP

Figure II.16 (a) shows the cuts through the transmit antenna pattern of GPS PRN 16 as seen from GCPM ground station on July 17th, 2017. Figure II.16 (b) compares the calibrated GPS EIRP of PRN 16 (black curve, using calibrated P_T and baseline pattern in [105] for G_T) and the measured EIRPs (red and blue curves computed directly from the GCPM received signal). They agree very well and demonstrate the effectiveness of the estimated GPS transmit power.

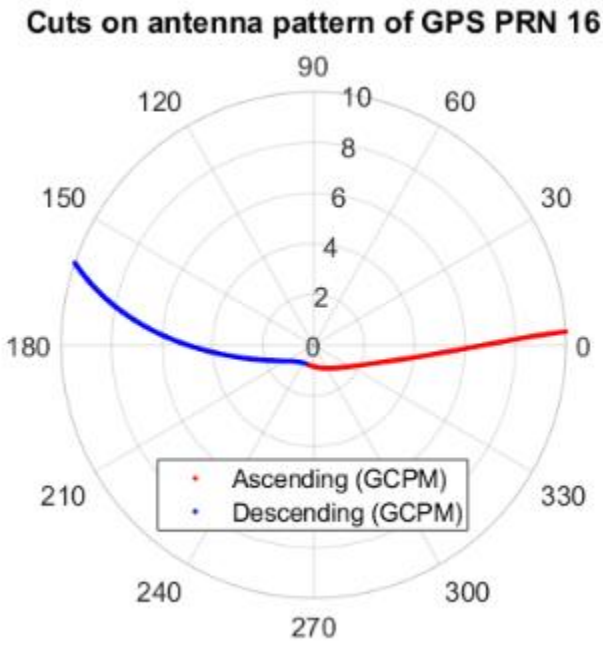

(a)

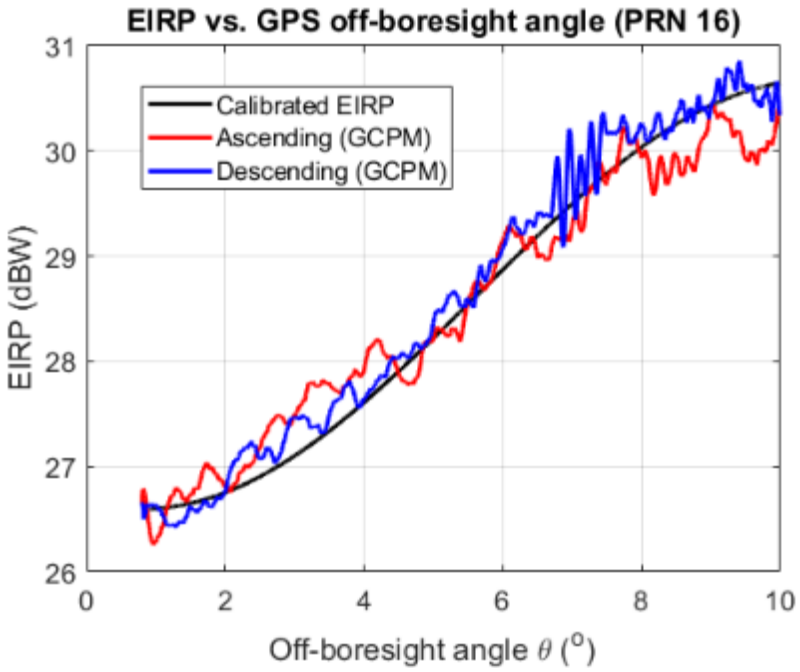

(b)

Figure II.16 GCPM's measurement (PRN 16, Block IIR): (a). Cuts through the antenna pattern; (b). Calibrated and measured EIRPs

2.6.3 Demonstration of Antenna Pattern Asymmetry

Figure II.17 (a) shows the cuts through the transmit antenna pattern of GPS PRN 18 as seen from GCPM ground station on July 17th, 2017. There are two distinct EIRPs of ascending and descending orbits in the 1st and 2nd quadrants, representing the antenna gain pattern at different azimuth angles. In Figure II.17 (b), the two branches of the measured EIRPs separate from one another. This is evidence of an antenna pattern azimuthal asymmetry.

These results demonstrate the need for inclusion of the azimuth dependence of the antenna gain as well as the spacecraft yaw attitude [116], [117] in the CYGNSS L1b algorithm.

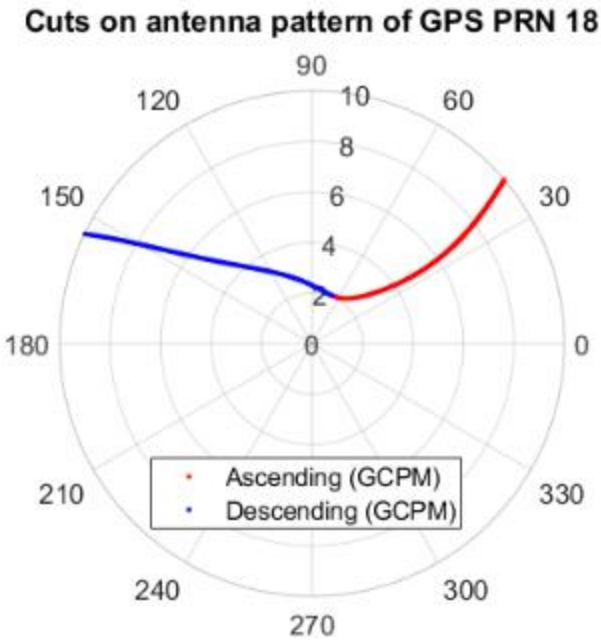

(a)

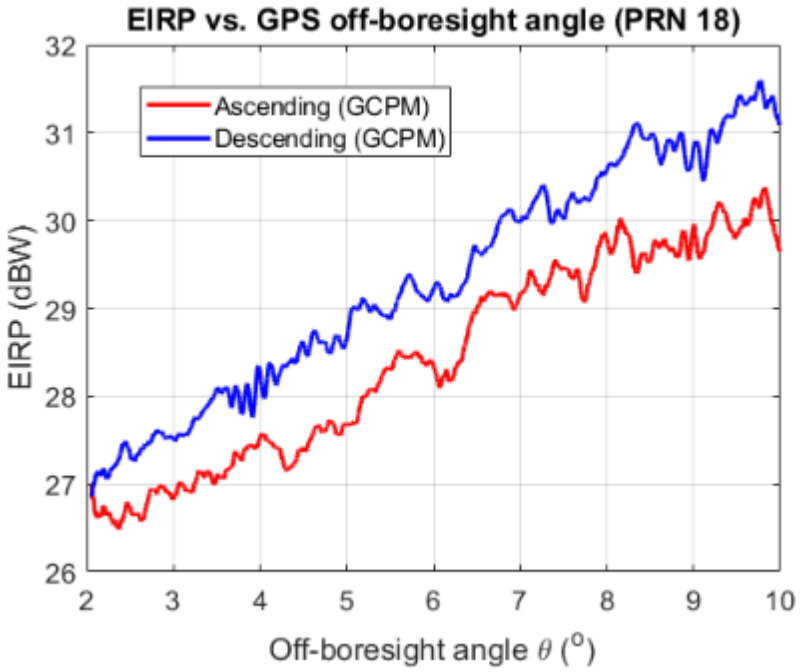

(b)

Figure II.17 GCPM's measurement (PRN 18, Block IIR): (a). Cuts through the antenna pattern; (b). Measured EIRPs

CHAPTER III

Measuring GPS and CYGNSS Antenna Gain Pattern with a Spaceborne Antenna Range

3.1 Introduction

The second primary determiner of EIRP is the transmit antenna gain. The gain is defined as the product of the directivity and the gain correction factor (GCF). However, the available to public knowledge of the GPS antenna patterns are very limited. The first published GPS L-band antenna patterns included four azimuthal cuts of the relative gain from a Block IIA antenna [123]. Measurements from the AMSAT experiment showed that the main lobes on the Block IIR satellites were slightly narrower than the Block II/IIA patterns and that some side-lobe levels for Block IIR satellites were significantly higher than expected [124]. This demonstrated that the gain pattern could be significantly affected by the space vehicle (SV) on which it was mounted. Over the next 2 decades, the only publicly available GPS antenna patterns are the 20 measurements for Block IIR and IIR-M satellites collected during prelaunch testing and published by Lockheed Martin in 2015 [115]. There are no comparable publicly available datasets for the Block II/IIA/IIF/III satellites. The published patterns have been used to determine the transmit power of GPS satellites in various ground-based experiment. Azimuthal asymmetry in the patterns has been observed by these experiments. Additional studies have shown that the published pre-launch patterns are not of sufficient accuracy to meet the requirements of some GNSS-R scientific investigations [125].

On orbit determination of GPS transmit antenna gain patterns was attempted previously by the GPS Antenna Characterization Experiment (GPS ACE), a research collaboration between the Aerospace Corporation and NASA Goddard Space Flight Center (GSFC). GPS ACE characterized the side-lobe portion of GPS L1 antenna patterns using receivers in a geosynchronous equatorial orbit (GEO) [126]. Notably, the main beam (on-Earth) portion of the GPS antenna pattern was not characterized. The work presented here expands upon the approach initially developed by GPS ACE using GPS receivers deployed on the constellation of CYGNSS satellites in Low Earth Orbit (LEO), rather than in GEO. This measurement geometry allows for sampling of the transmitted signal throughout the main beam portion of the GPS antenna pattern. The link equation for the received signal power is inverted to determine the GPS transmit antenna gain pattern. Additionally, the receive antenna pattern on each CYGNSS satellite can also be determined by inversion of the link equation. Because the two solutions are coupled by a common link equation, an iterative retrieval procedure is developed which estimates both patterns sequentially. Details of the iterative procedure, and of its convergence properties and robustness, are detailed in the following sections.

Much of the work presented in this chapter is reported in [127]–[129].

3.2 Spaceborne Antenna Range Measurements

3.2.1 Constellations of GPS and CYGNSS

Table III-1 summarizes the basic information of the GPS and CYGNSS constellations.

The GPS constellation of satellites are all in Medium Earth Orbit (MEO) at 20,180 km altitude. There are currently 31 operational satellites consisting of 4 different SV designs (referred to as block types). There are 8 Block IIR, 7 Block IIR-M, 12 Block IIF, and 4 Block III. For Block

IIR and IIR-M SVs, there are two antenna designs used. The 31 satellites are distributed over 6 evenly spaced orbit planes and their orbit period is approximately 12 hours.

The CYGNSS constellation of 8 satellites are all in LEO at 520 km altitude. They share a common orbit plane, and the orbit period is approximately 95 minutes. Each spacecraft carries a navigation receiver connected to a zenith-mounted antenna that receives direct GPS L1 C/A code signals for navigation. Two science receivers connected to nadir-mounted antennas also receive reflected GPS signals from the Earth surface for remote sensing applications. While calibration of these nadir GPS antennas is important for a number of science applications, it is not the focus of this work.

Table III-1 GPS and CYGNSS constellations

Constellation	GPS	CYGNSS
Orbit	MEO	LEO
Height (km)	20180	~ 520
Inclination (º)	55	37
Period	11 hours 58 minutes	~ 1.5 hours
# of satellites	31 active	8
Block Type	IIR, IIR-M, IIF, III	Uniform

The CYGNSS zenith navigation antenna is a half-wave dipole patch. Its gain pattern was measured in an anechoic chamber prior to launch while mounted on a satellite mock-up. Those measurements revealed that the pattern is affected by coupling and multipath from nearby structures on the spacecraft. The measured pattern cannot be assumed to be an accurate representation of the on-orbit patterns owing to mechanical tolerances and limits on repeatability that are associated with final assembly of the spacecraft. For these reasons, the on-orbits patterns may differ from the pre-launch pattern and from one another.

3.2.2 Spaceborne Antenna Measurement Range

The GPS and CYGNSS satellites have precisely known positions and orientations. They are in orbit well above any atmospheric propagation effects and are well isolated from multipath effects. In this sense, measurements between the two satellites form an ideal "spaceborne antenna range". It provides a unique opportunity for precise determination of the GPS transmit and CYGNSS receive antenna gain patterns which includes the effects of satellite structures on their patterns. Figure III.1 depicts the antenna measurement setup. From an antenna range perspective, the GPS antenna can be viewed as the illuminating source and the CYGNSS antenna, as the antenna under test (AUT). By reciprocity, the GPS antenna can also be viewed as the AUT if the CYGNSS antenna pattern is known.

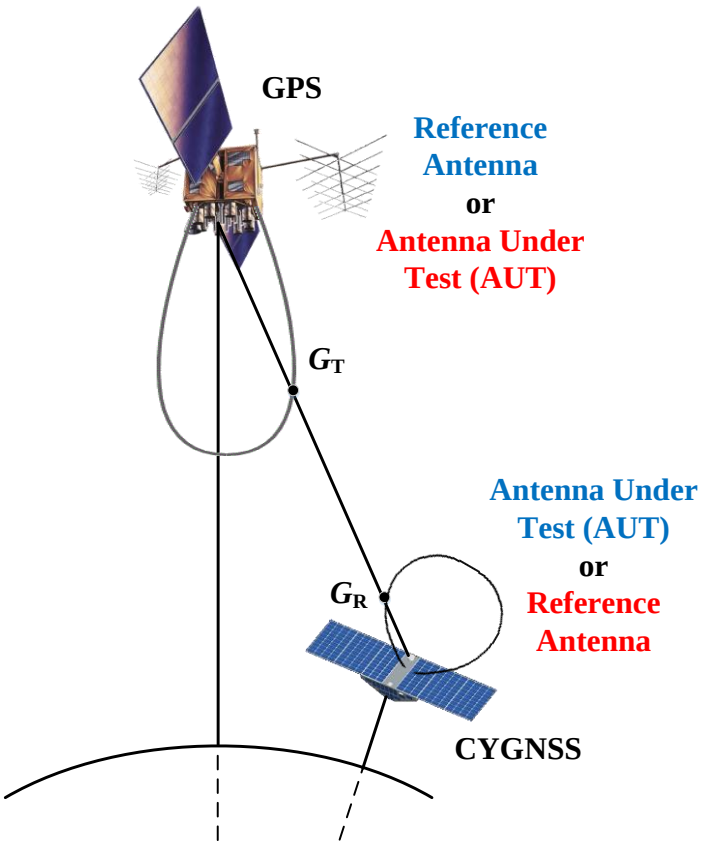

Figure III.1 Spaceborne antenna range measurement system formed by constellations of GPS and CYGNSS satellites

3.2.3 Range Unique Angular Sampling Capability of the Spaceborne Range

As a side note, determination of the GPS patterns using ground-based receivers has also been considered. However, the highly repeatable 12-hour GPS orbit results in measurements made at a fixed ground location that cut through nearly identical slices of the GPS pattern day-after-day and month-after-month. This is illustrated in Figure III.2 (a), which shows the location in the GPS antenna coordinate system of all samples made by a ground-based receiver over a 100 day period. In the figure, the radial coordinate is the angular distance from the antenna boresight and the azimuthal coordinate is the azimuthal angle about the boresight direction, with 0° referenced to the +X axis in the GPS satellite reference frame. A more detailed description of the coordinate system can be found in [115]. For the results shown in Figure III.2 (a), the receiver was located in Ann Arbor, MI and the GPS satellite is SVN 54, but the results are similar for any fixed location and specific SV. A large network of well-calibrated ground stations distributed across the globe would be required to adequately sample a full GPS pattern. For this reason, use of the orbiting CYGNSS receivers is an attractive alternative.

Compared to using a ground-based receiver to calibrate GNSS antennas, there is a distinct advantage in angular sampling when using a spaceborne receiver [130]. Figure III.2 (b) shows the location of all samples made of a single GPS antenna pattern (in the GPS antenna coordinate system) by the 8 CYGNSS satellites in one day, and Figure III.2 (c) shows the sampling distribution after 1 week. The GPS pattern is much more fully sampled by the CYGNSS satellites in one week than the ground-based system was able to in 100 days. For the work presented here, we use approximately 2 years of samples by the constellation of CYGNSS satellites for even better pattern coverage. The spaceborne antenna range system provides nearly gap-free measurements of the GPS satellite antenna pattern over all azimuth angles and out to an off-boresight angle of ~15.2

deg. The Earth horizon is located at ~13.8 deg in the GPS satellite antenna coordinate system and CYGNSS is able to measure the GPS satellite transmit gain pattern as it extends into the LEO space service volume due to its 520 km orbit altitude.

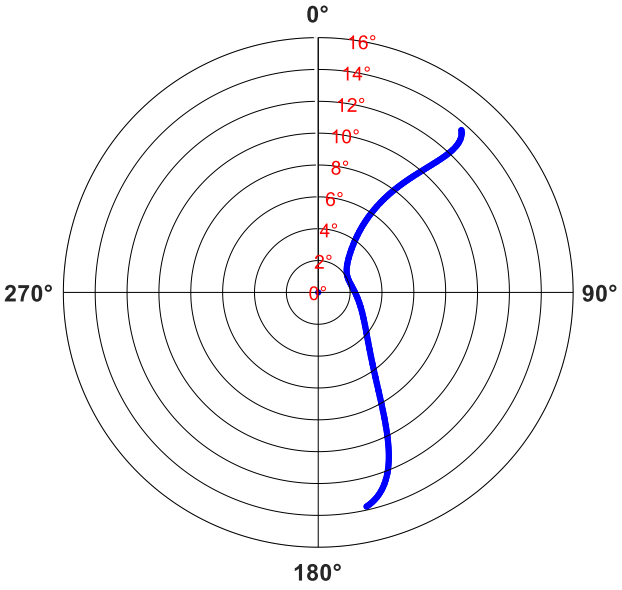

(a)

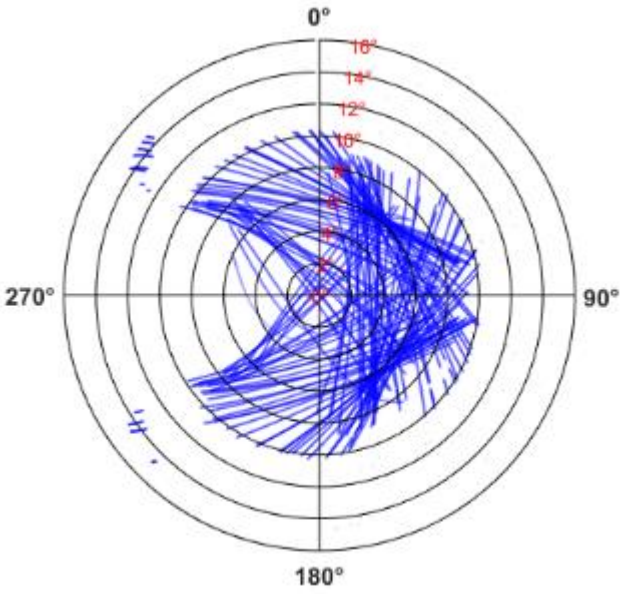

(b)

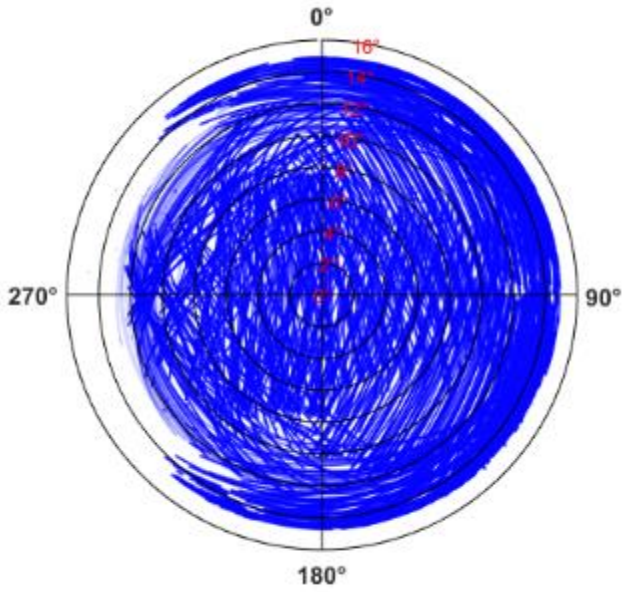

(c)

Figure III.2 Location in the GPS antenna coordinate system of gain pattern measurements made by: (a) A ground-based receiver over 100 days; (b) 8 CYGNSS satellites in one day; (c) 8 CYGNSS satellites in 1 week

3.2.4 Sampling Density of GPS Satellite and CYGNSS Satellite Antenna Patterns

In this work, antenna patterns are estimated using measurements made by the spaceborne antenna range over a long time interval, to further improve the sampling distribution, to allow for detection of outlier data samples, and to average out the effects of measurement noise. Both GPS and CYGNSS antennas are jointly estimated, and they can each be treated as the AUT at different stages of the analysis.

Figure III.3 shows the sampling density for a particular GPS satellite antenna from 2018 DOY 213 to 2020 DOY 182 using measurements from all 8 CYGNSS satellites. The sampling density is shown in the GPS satellite antenna coordinate system, and it accounts for the orientation of the GPS satellite, including its periodic change in yaw state [116], [117], using NASA GIPSY-X software [131]. In the figure, the angular resolution of sampling density is 0.5×0.5 deg and the color map denotes the number of samples in each bin.

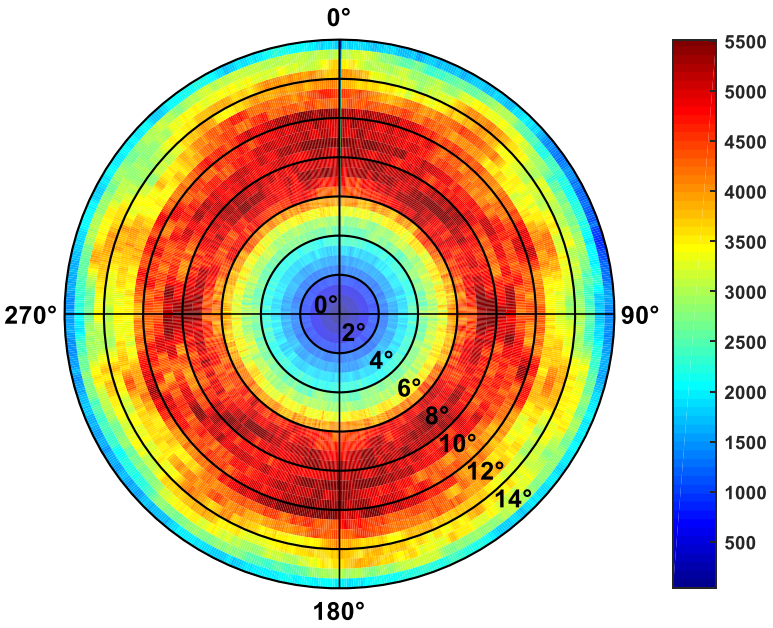

Figure III.3 Sampling density over GPS antenna pattern using ~ 2 years' data

Figure III.4 shows the sampling density of a single CYGNSS antenna pattern in its coordinate system, using all data from the same time period as Figure III.3. Measurements in this figure are accumulated over a subset of GPS SVNs: 41, 43, 44, 45, 46, 51, and 56. This particular subset of GPS SVs is used because: 1) they correspond to older block types which have been found to exhibit less variability in their transmit power level than the more recent block types [109], [119]; and 2) their antenna pattern have less azimuthal variability, according to the published patterns in [115]. The angular resolution in Figure III.4 and in the estimated CYGNSS antenna patterns is 1×1 deg.

The distribution of samples of the CYGNSS patterns is much less uniform than that of the GPS patterns. Samples are concentrated in the vicinity of azimuthal angles 90 and 270 deg, which correspond to the starboard and port directions relative to the forward motion of the CYGNSS satellites. This uneven sampling density results from a property of the CYGNSS GPS receivers, which records signals from GPS transmitters for which the signal reflected from the Earth surface

enters the nadir science antenna in its main beam. The science antennas are fan beams pointed in the spacecraft's starboard and port directions. Only measurements of direct signals received by the zenith antenna that correspond to reflected signals received by the nadir antennas are downlinked to the ground. This restriction on the distribution of samples of the zenith pattern means that, unlike with the GPS patterns, its gain cannot be determined uniformly across the entire main beam. Fortuitously, it is only in the portions of the main beam that are well sampled that accurate antenna gain knowledge is required for purposes of CYGNSS science data calibration.

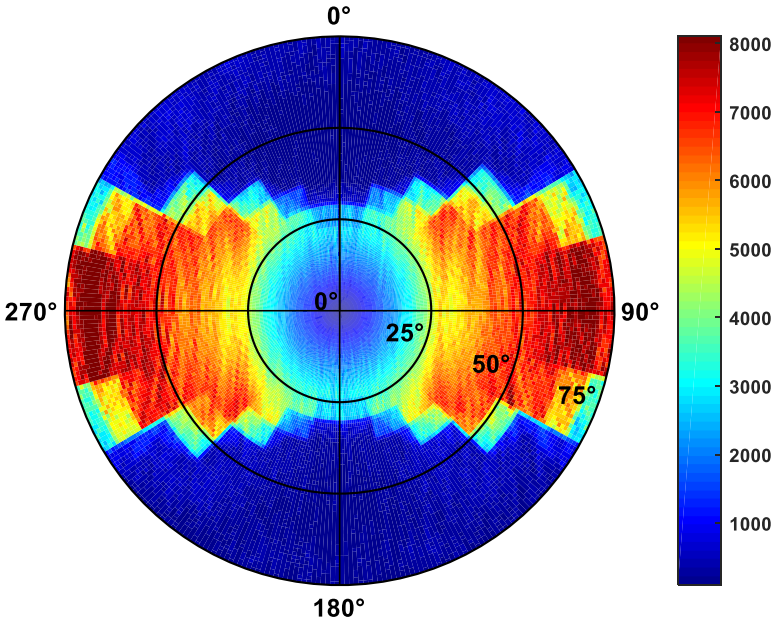

Figure III.4 Sampling density over CYGNSS zenith antenna pattern using ~ 2 years' data

3.2.5 Calibration of Received Power of Zenith Channel

The received power referenced to the output port of the CYGNSS zenith antenna, P_R, can be determined from P_z, the calibrated power at the input port of the receiver, by correcting for the gain of the zenith low noise amplifier (LNA), G_{LNA}, according to

$$P_R = \frac{P_Z}{G_{LNA}(T_{LNA})} \tag{3.1}$$

where T_{LNA} is the temperature of the zenith LNA. G_{LNA} is calculated using a pre-launch look-up table (LUT) of gain vs. physical temperature. P_Z is converted from raw counts to power in watts based on the hardware calibration experiment described in the Appendix.

The Friis transmission equation expresses the relationship between the received power and the gain of the transmit and receive antennas according to

$$P_R = \frac{\lambda^2}{(4\pi R)^2} P_T G_T(\theta_T, \phi_T) G_R(\theta_R, \phi_R) \tag{3.2a}$$

$$G_R(\theta_T, \phi_T) = \frac{(4\pi R)^2}{\lambda^2} \frac{P_R}{P_T G_T(\theta_R, \phi_R)} \tag{3.2b}$$

$$G_T(\theta_T, \phi_T) = \frac{(4\pi R)^2}{\lambda^2} \frac{P_R}{P_T G_R(\theta_R, \phi_R)} \tag{3.2c}$$

where G_T is the gain of the GPS transmit antenna, G_R is the gain of the zenith receiver antenna, θ_T and ϕ_T are the off-boresight and azimuthal angles of the transmit antenna in the GPS antenna coordinate system; θ_R and ϕ_R are the off-boresight and azimuthal angles of the receive antenna in the CYGNSS antenna coordinate system; R is the distance from the transmitter to the receiver, λ is the wavelength for GPS L1 signals, and P_T is the transmit power of the GPS satellite.

Eq. (3.2b) and (3.2c) are used to compute the gain of the GPS transmit antenna and CYGNSS receive antenna in the following sections.

3.3 Estimation of CYGNSS and GPS Satellite Antenna Patterns

Either the GPS or the CYGNSS antenna can be considered the antenna under test (AUT). Depending on which one it is, one or the other of Eq. (3.2b) or (3.2c) is used to estimate the gain. Therefore, the estimation of one of the gain patterns presupposes knowledge of the other one. Both

patterns can be estimated sequentially. The CYGNSS receive pattern, G_R, is estimated first by assuming that the published pre-launch GPS pattern is G_T. Next, the GPS pattern is estimated by assuming that the CYGNSS pattern is the G_R that was just determined. If the new GPS pattern is identical to the pre-launch pattern, then the estimation process is complete. As will be shown below, this turns out not to be the case, and an iterative procedure is developed instead which can jointly estimate both patterns. It should be noted that the analysis presented here assumes the polarization of the transmitted signal and the receive antenna in the direction of the transmitted signal are both right hand circular and matched. In practice, the cross-pol levels of both the transmit and receive antennas may vary, especially away from their boresight directions, there may not be an exact polarization match between them, and the mismatch that exists may vary depending on the relative orientations of the GPS and CYGNSS satellites. This can introduce apparent variations into the gain patterns derived from the measurements of received power that are actually variations in the polarization mismatch. This effect is believed to be small but has not been characterized quantitatively.

3.3.1 Estimation of CYGNSS Antenna Patterns

There are eight CYGNSS spacecraft, which are designated FM1-FM8. Although all spacecraft and GPS antennas are similar, small differences in each antenna combined with differences in the deployment of surrounding satellite structures results in significant gain pattern differences. For this reason, each receive antenna pattern is determined independently. For each one, the pattern can be estimated using many different GPS SVs as the transmitter. We use the subset of seven GPS SVs noted above, because their transmit power level P_T is most stable over time. Examples of the resulting G_R patterns for FM1 using SVN 43 and 46 are shown in Figure

III.5 (a) and (b), respectively. Several characteristics of the two patterns are noteworthy. Both are well sampled over the azimuthal ranges 75-105 deg and 255-285 deg for reasons discussed above. The two gain patterns are generally consistent in these two sectors. Outside of the sectors, the sampling density varies due to differences in the individual orbits of the GPS satellites and some angular regions are sampled better by one SV than the other. For this reason, it is desirable to combine together patterns estimated using multiple SVs to create a single, well-sampled composite pattern. Before doing so, it is prudent to test whether the patterns are consistent with one another within the angular region in which they overlap.

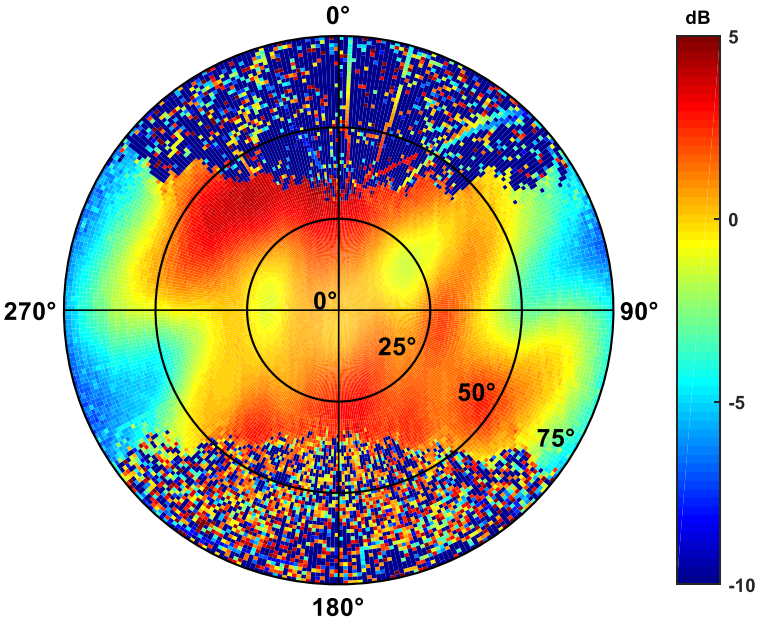

(a)

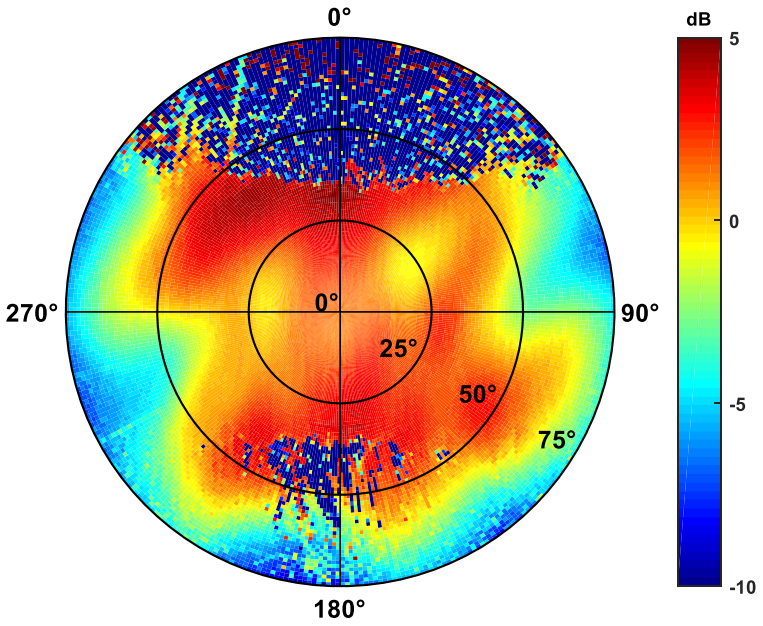

(b)

Figure III.5 Example of the retrieved zenith gain pattern (FM1) using each GPS signals. (a) SVN 46; (b) SVN 43

The average value of G_R over the two well-sampled sectors is considered individually for each FM derived from each SV. This value, referred to as the normalized integrated gain, G_{NI}, is given by

$$\bar{G}_{NI} = \sum_{\theta_i=25}^{70} \left[\sum_{\phi_i=75}^{105} \bar{G}_R(\theta_i, \phi_i) \sin\theta_i + \sum_{\phi_i=255}^{285} \bar{G}_R(\theta_i, \phi_i) \sin\theta_i \right] \Delta\theta\Delta\phi \qquad (3.3)$$

where θ_i and ϕ_i are the off-boresight and azimuthal angles and the discretized average is computed over ϕ_i within ± 15 deg of the port and starboard directions and over θ_i within 25-70 deg. $\Delta\theta$ and $\Delta\phi$ are the resolution over off-boresight and azimuth. These are the two sectors with consistently high sampling density for all SVs. N is the total number of pixels used.

A comparison of $\bar{G}_{NI}$ for the eight CYGNSS FMs and 7 GPS SVs is shown in Figure III.6 (a). The different colors indicate different FMs and the x-axis is the GPS SVN. A shift in the

average gain is evident between SVs that is consistent across all FMs. The most likely cause of the shift is errors in the assumed GPS transmit power levels of the individual SVs. The values used for P_T are based on previous measurements made by a ground-based GPS power monitor system, as reported in [114]. The shifts in G_{NI} for a fixed FM as SVN is varied represent differences in the error in P_T. It is not possible with this analysis to determine absolute values for each P_T, but it is possible to adjust their individual values so that any remaining error is common to all seven SVs. This is done by assuming the average value of P_T across all seven SVs is correct and then rescaling the individual values so that G_{NI} is consistent. The result is shown in Figure III.6 (b), which is computed in the same way as Figure III.6 (a) after the individual values of P_T have been adjusted. Once the P_T adjustment has been made, the individual G_R patterns derived from each SV can now be combined together into a single pattern. The result is shown in Figure III.7 for FM1. Similar G_R patterns are computed in the same way for each FM.

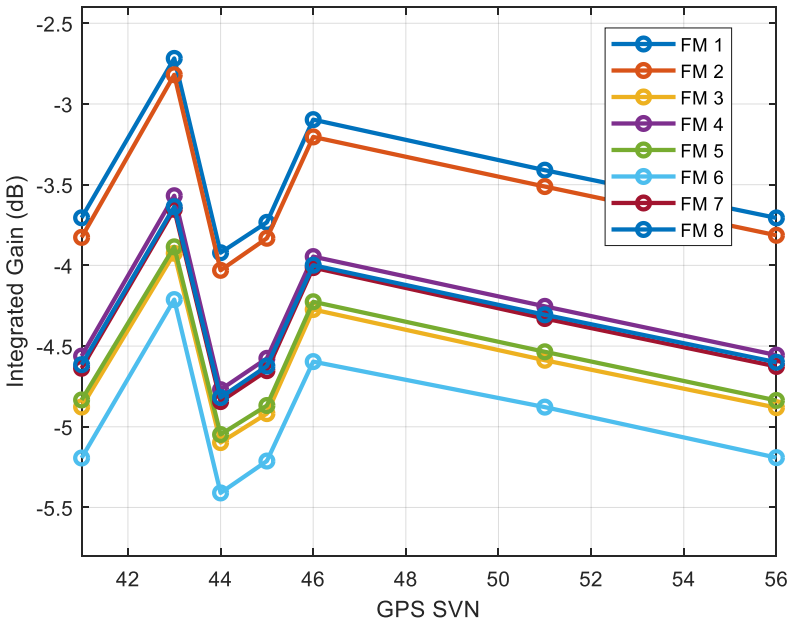

(a)

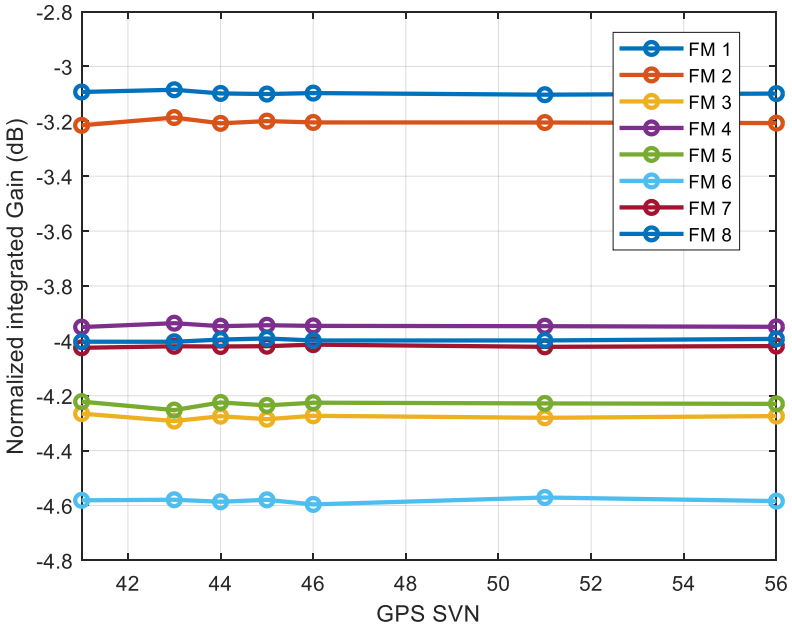

(b)

Figure III.6 Normalized integrated gain G_{NI} vs. GPS SVN for 8 FMs: (a) Raw calculation; (b) Bias removed

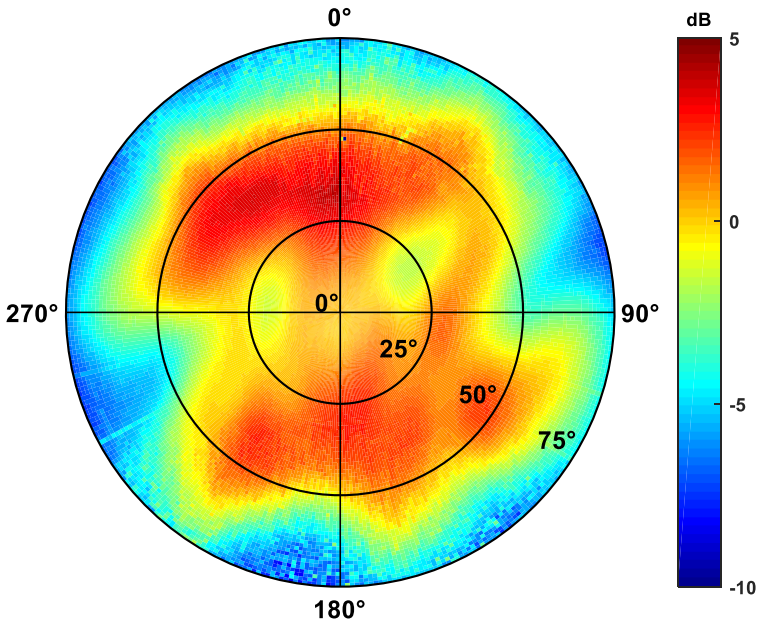

Figure III.7 Example of the retrieved zenith gain pattern (FM1) using 7 SVs

3.3.2 Estimation of GPS Antenna Patterns

The GPS antenna pattern, G_T in (3.2), can be similarly derived from the measurements given knowledge of G_R. In this case, measurements using all eight CYGNSS FMs are combined together to estimate G_T for a single GPS SV. When the eight FM patterns derived in the previous section are assumed for GR, the resulting GT pattern for SV 56 is shown in Figure III.8 (a). The computed pattern is considered reliable at off-boresight angles of less than 12 deg. Above this angle, the low gain of the receive antenna reduces the received signal strength significantly. Recall that the published pre-launch G_T pattern was assumed when solving for G_R. If the new G_T pattern was the same as the pre-launch one, then the measurements of P_R and the two patterns, G_R and G_T, will all be consistent with (3.2). But that is not in fact the case. This is illustrated in Figure III.8 (b), which plots the difference between the pre-launch G_T pattern and the one derived here. Note that the published pre-launch patterns are only available with a coarse 2×10 deg resolution so the pattern derived here has been smoothed to that same resolution to compute the difference.

Figure III.8 (b) shows clear signs of structural differences between the two antenna patterns, as opposed to unstructured, random differences that might be attributed to measurement noise. One possible explanation for the difference is that the pre-launch pattern is not accurate. If this is the case, then the newly estimated GPS pattern may be more accurate than the pre-launch one. To that end, an iterative solution is considered next which updates estimates of G_R and G_T at each iteration. The objective is for the iterative process to converge to a pair of patterns that are mutually consistent with the measured values of P_R, as stipulated by the relationship in (3.2).

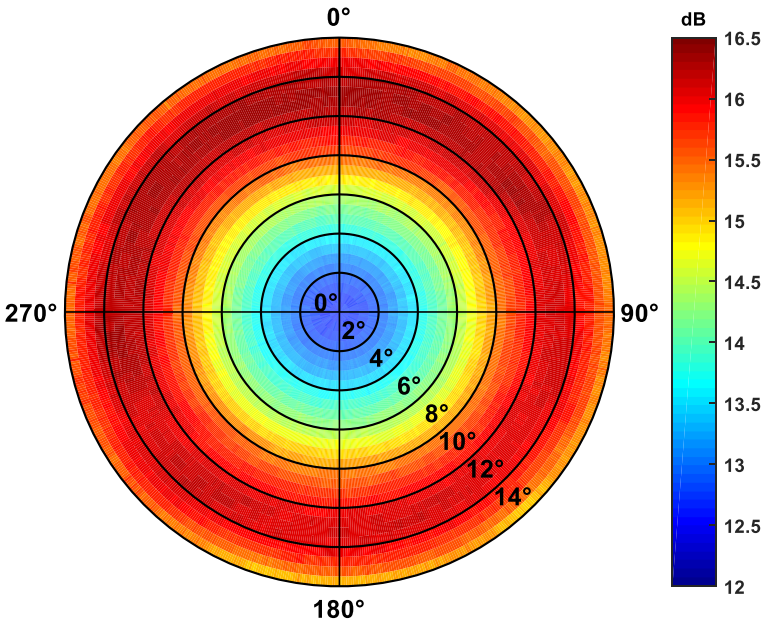

(a)

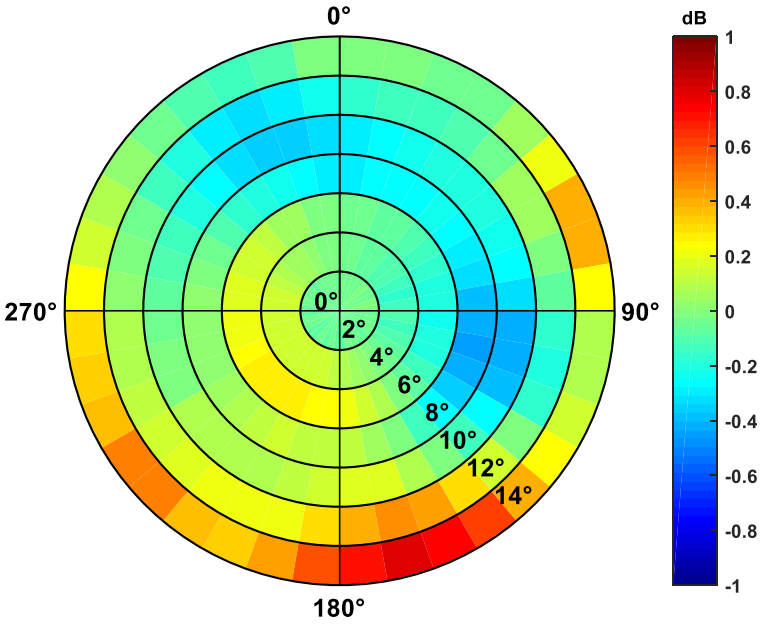

(b)

Figure III.8 (a) GPS SVN 56 antenna gain pattern derived after one iteration of the spaceborne antenna range analysis procedure. (b) Difference between the published pre-launch pattern for SVN 56 and the pattern shown in (a)

3.4 Joint Estimation of CYGNSS and GPS Antenna Patterns

3.4.1 Overview of Iterative Retrieval Approach

Our approach to jointly estimate the GPS and CYGNSS antenna patterns is outlined in the flowchart in Figure III.9. Each CYGNSS pattern is estimated using Eq. (3.2b) and measurements with the seven GPS SVs given above. Then each GPS pattern is estimated using Eq. (3.2c) and measurements with the 8 CYGNSS FMs. Details of the data processing performed at each iteration were described in Section 3.3. An additional constraint is imposed on the GPS patterns at each iteration in order to stabilize the iterative retrieval process. The average value of the gain pattern, averaged over all azimuth angles and all off-boresight angles from 0 to 15.2 deg, is forced to agree with the average of the published pre-launch pattern by applying a single multiplicative scale factor to the entire pattern. The iterative process converges and the two sets of antenna patterns are finalized when changes in the patterns from one iteration to the next become negligible.

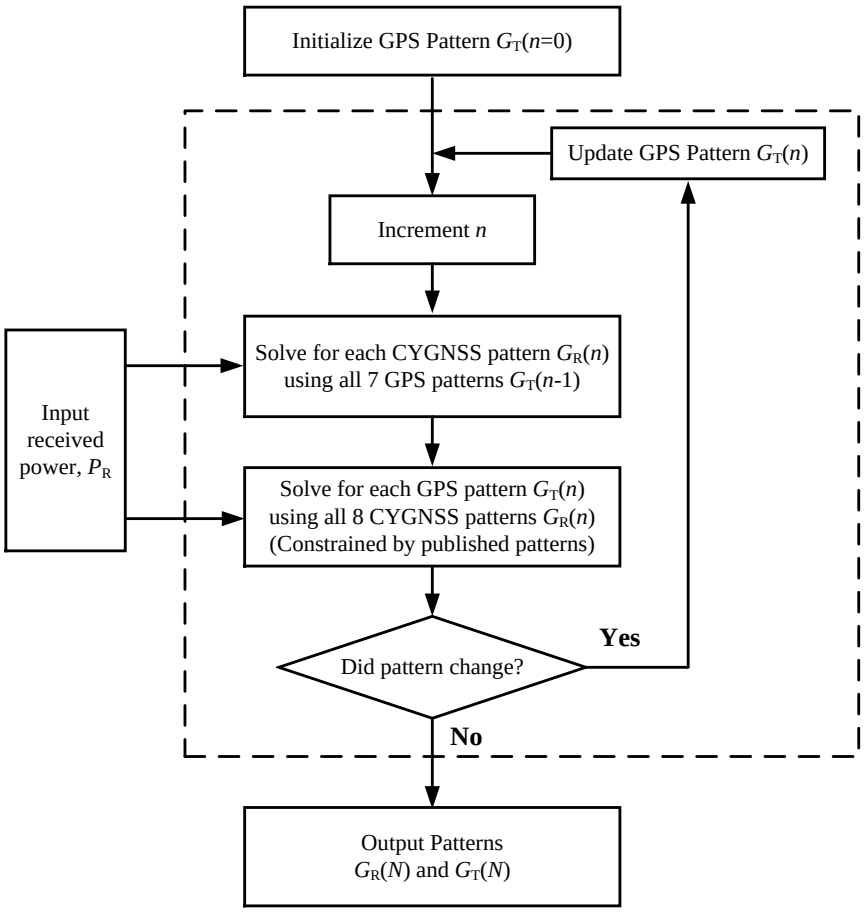

Figure III.9 Flowchart of iterative solution to the GPS and CYGNSS antenna patterns

3.4.2 Test for Convergence

The root-mean-square difference in gain between the N and (N-1) iterations for the 8 CYGNSS patterns is shown in Figure III.10 (a), and that for the 7 GPS patterns is shown in Figure III.10 (b). The iterative process converges after about 50 iterations. The gain patterns of the zenith antennas and GPS antennas are then finalized.

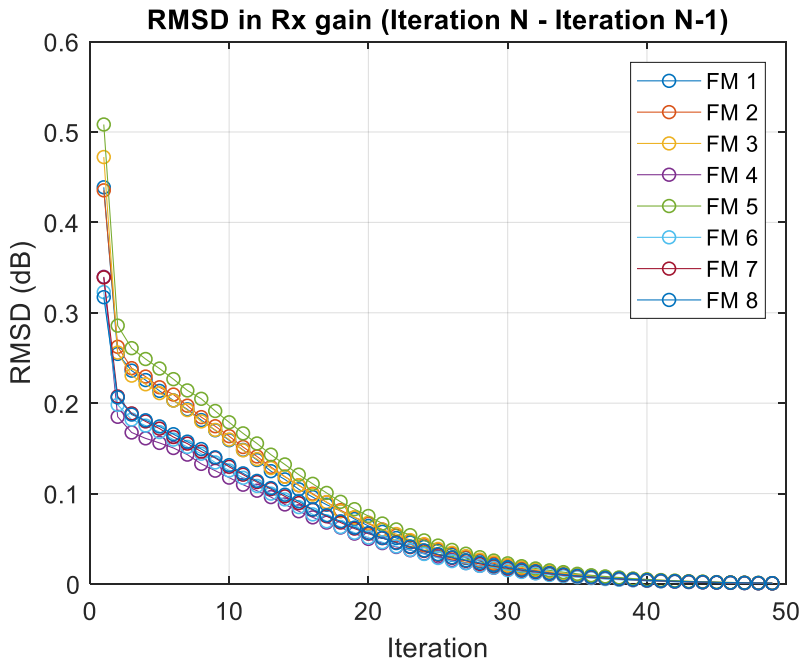

(a)

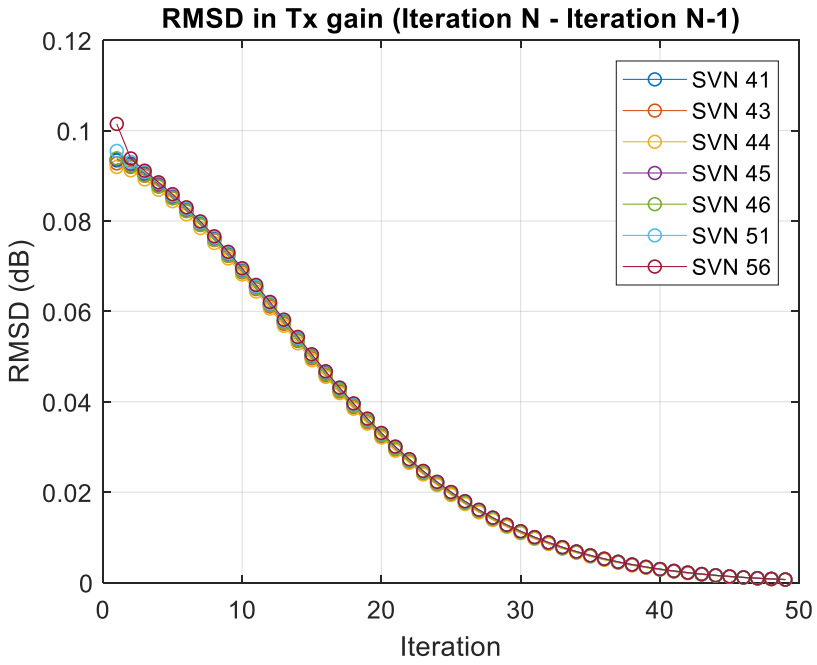

(b)

Figure III.10 Convergence vs. iteration. (a) RMSD of gain pattern difference for CYGNSS zenith antenna; (b) RMSD of gain pattern difference for GPS transmit antenna

3.4.3 Sensitivity to First Guess GPS Antenna Pattern

The iterative process described above depends on an initial guess for the GPS antenna pattern at the first iteration. If the overall approach is sound, the final result should be independent of this initial guess. To test the sensitivity of the final pattern to the first guess, the initial pattern was varied in a number of ways and the final pattern compared. Figure III.11 graphically illustrates the variations made in the first guess pattern by plotting the azimuthally averaged GPS gain vs. off-boresight angle for the original pre-launch pattern and for all of the variations considered. The original pattern is shown as a black solid line labeled “LM pattern” (for Lockheed-Martin). The red and blue solid lines correspond to increases and decreases in the LM pattern by 10%. The red and blue dashed lines correspond to tapered increases and decreases, in which the change grows with off-boresight angle. Finally, the dashed black line corresponds to an assumed isotropic antenna with the same average gain value as the original LM pattern. Figure III.11 shows the variation in patterns for GPS SVN 46. Similar perturbations were applied to all 7 GPS patterns.

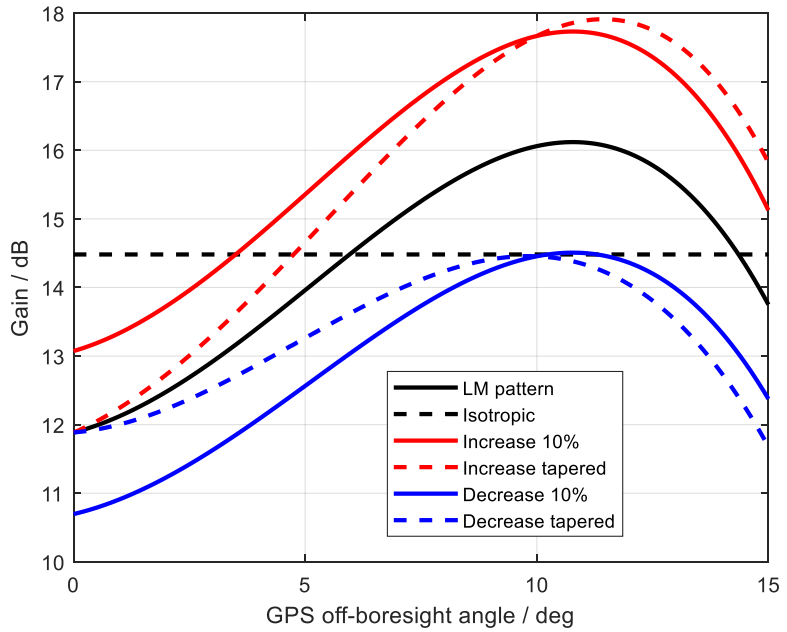

Figure III.11 Initial pattern of the GPS transmitter (example: SVN 46)

To evaluate the behavior of the iterative solution as a function of the first guess GPS pattern, three points in the pattern were examined. The first is in the boresight direction ($\theta = \phi = 0°$), the second is at a local maximum in the pattern at ($\theta = 40°$, $\phi = 48°$), and the third is at a local maximum in the pattern at ($\theta = 21°$, $\phi = 186°$). The gain at these three points vs. iteration number is shown in Figure III.12 for each of the first guess patterns. For the first few iterations, the gain values can be seen to depend strongly on the first guess. However, in each case, they eventually converge to the same value, regardless of the first guess. The final gain patterns estimated for each of the 8 CYGNSS antennas were also examined and found to be nearly identical, regardless of the first guess GPS pattern that was assumed. This strongly suggests that the iterative solution is robust and does not depend on the first guess.

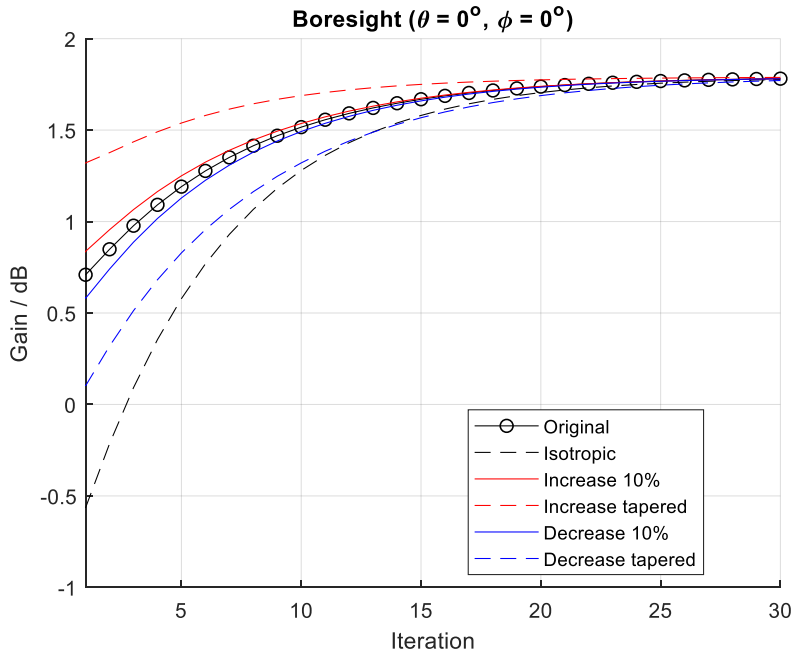

(a)

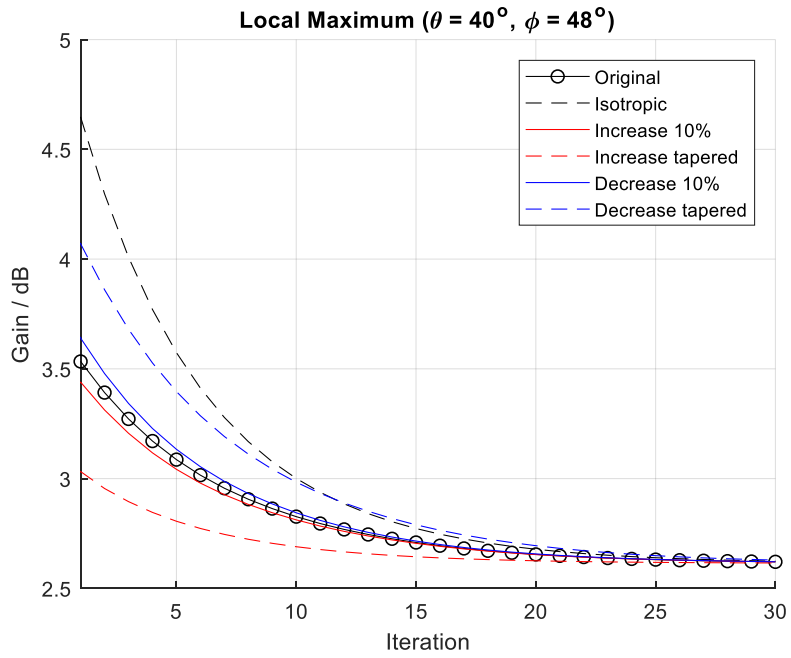

(b)

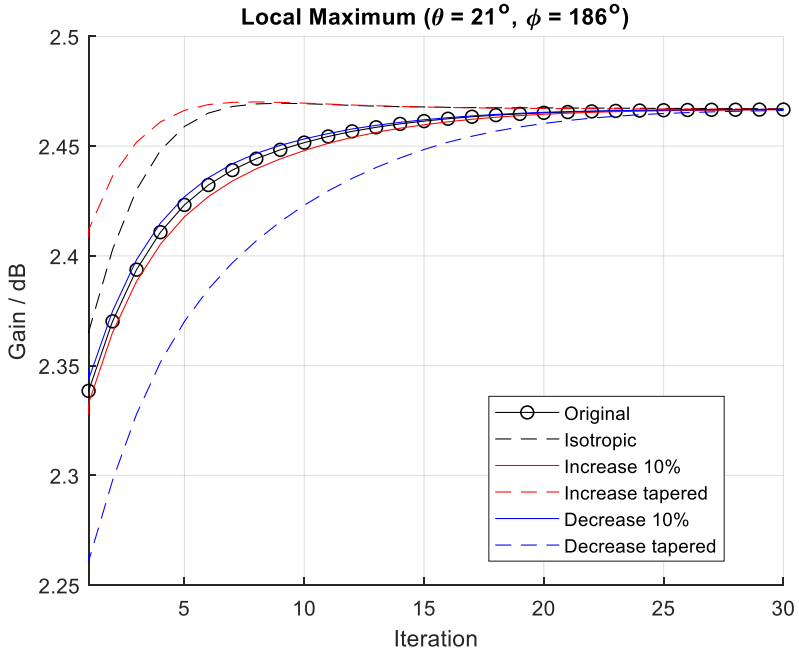

(c)

Figure III.12 Estimated gain of the GPS satellite antenna pattern in 3 different directions (a), (b), and (c) versus iteration number that demonstrates common convergence from different initial patterns (indicated in different line types)

3.5 Estimated Antenna Patterns and Discussion

3.5.1 Comparison of GPS Antenna Patterns

Figure III.13 compares the published pre-launch pattern and the iteratively retrieved pattern for GPS SVN 56. The retrieved pattern shows azimuthal asymmetry features which are generally consistent with those of the pre-launch pattern. However, because of its much higher angular resolution, small features can be seen in the retrieved pattern that cannot be resolved by the pre-pre-launch one. Some of those features may be caused by noise in the measurements and retrieval process. They can be smoothed out by a moving average with a proper window size. Final sets of the retrieved GPS antenna patterns are under development.

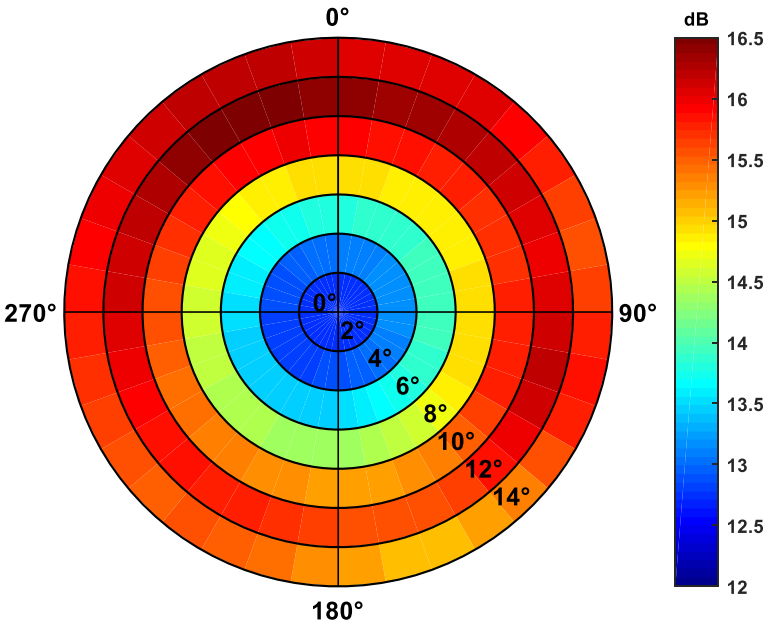

(a)

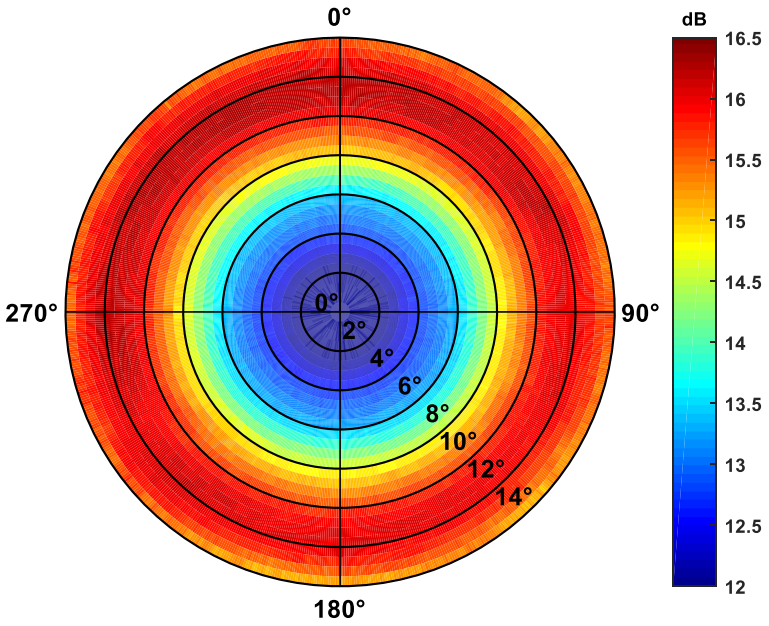

(b)

Figure III.13 Comparison of GPS antenna patterns of SVN 56. (a) published pattern; (b) retrieved pattern

3.5.2 Comparison of CYGNSS antenna patterns

Figure III.14 compares the pre-launch measured pattern of the CYGNSS antenna mounted on a spacecraft mock-up and the iteratively retrieved pattern for CYGNSS FM1. Note that the pre-launch measured pattern is re-scaled to remove a calibration offset. The pre-launch and retrieved patterns show similar general features; however, there are a number of small but significant differences between them. Preliminary studies of the principal-plane cuts of the pre-launch measured pattern and the on-orbit retrieved patterns support the notion that antenna patterns should be independently determined for each of the CYGNSS spacecraft while on-orbit in their operational environment. Final sets of the retrieved zenith antenna patterns are under development.

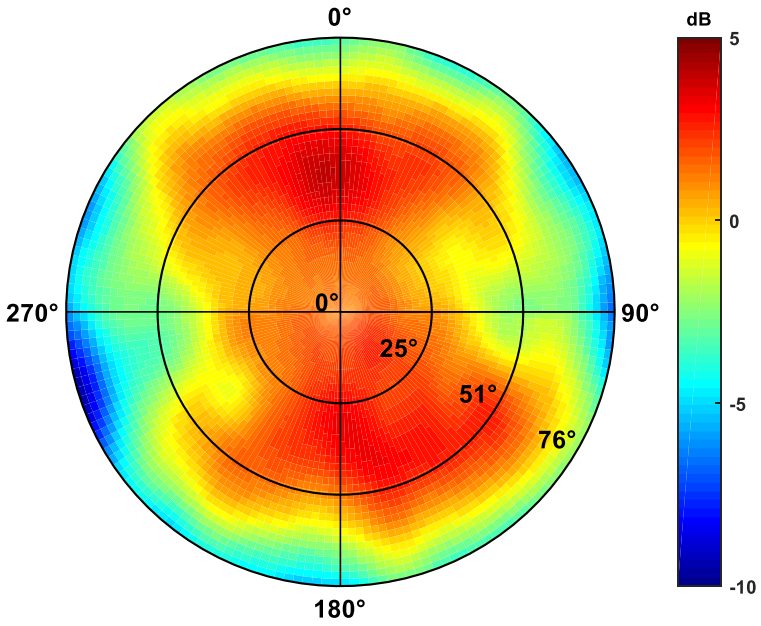

(a)

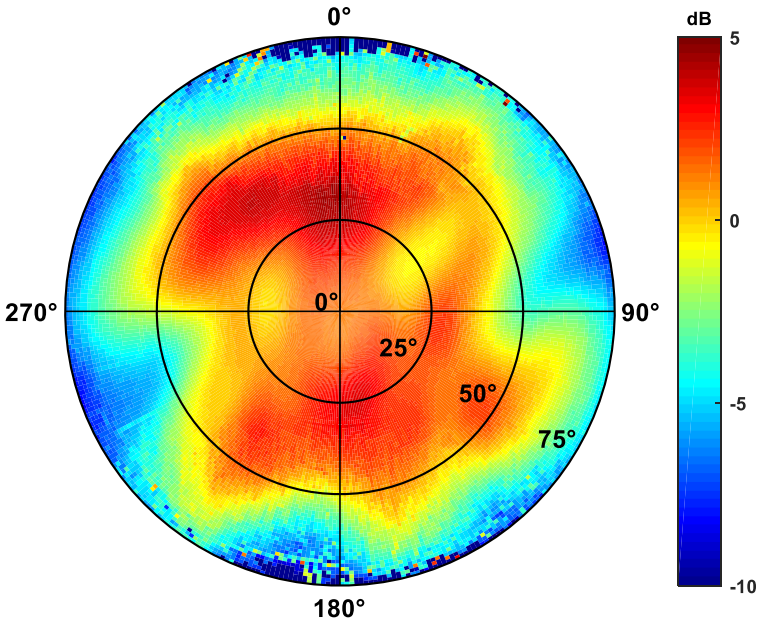

(b)

Figure III.14 Comparison of (a) Scaled pre-launch measured pattern using a satellite mock-up; (b) Retrieved pattern of CYGNSS FM 1

3.5.3 Summary of Calibration Results

Table III-2 summarizes the limited knowledge of the GPS and CYGNSS antenna patterns prior to the work presented here, and the improvements that have been made. Specifically: 1) For CYGNSS antennas, 8 calibrated gain patterns were characterized in their operational environment, compared with only 1 pre-launch measured pattern using a single, crude CYGNSS satellite mock-up; 2) For GPS antennas, more than 31 GPS patterns are calibrated precisely (0.5×0.5 degrees) and accurately when the antennas are mounted on the satellites and in their operational environment, compared with only 20 published pre-launch measured patterns with rather coarse (2×10 deg) angular resolution.

Table III-2 Improvement of antenna pattern characterization

Antenna	Before	After
GPS	20 pre-launch measured patterns with limited angular resolution (2×10 degrees)	>31 calibrated patterns with antenna in its operational environment (0.5×0.5 degrees)
CYGNSS	1 pre-launch measured pattern using a spacecraft mock-up	8 calibrated patterns in its operational environment

3.6 Appendix: End-to-end Calibration of the Zenith Measurements

The zenith channel of the CYGNSS receiver was designed for navigation, so there was no previous calibration technique developed to convert the received signal strength, measured in raw counts, into power in watts. In addition, the navigation receiver's automatic gain control (AGC) was initially enabled to ensure a consistent power level for navigation purposes, making it

impossible to calibrate the direct signal. Since 1 August 2018, AGC was been disabled and a constant gain value has been set for all 8 CYGNSS FMs.

An end-to-end calibration experiment using an engineering model (EM) of the CYGNSS Delay-Doppler Mapping Receiver (DMR), a low noise amplifier (LNA) and a GPS signal simulator (GSS) was conducted to emulate the on-orbit measurement, as shown in Figure III.15 (a). The calibration experiment setup is given in Figure III.15 (b). The GSS generates a simulated GPS signal and the power level is measured by a power meter. It is then attenuated to the power level experienced on-orbit and input to the EM LNA. All the cable losses and cascaded attenuators are measured by a vector network analyzer.

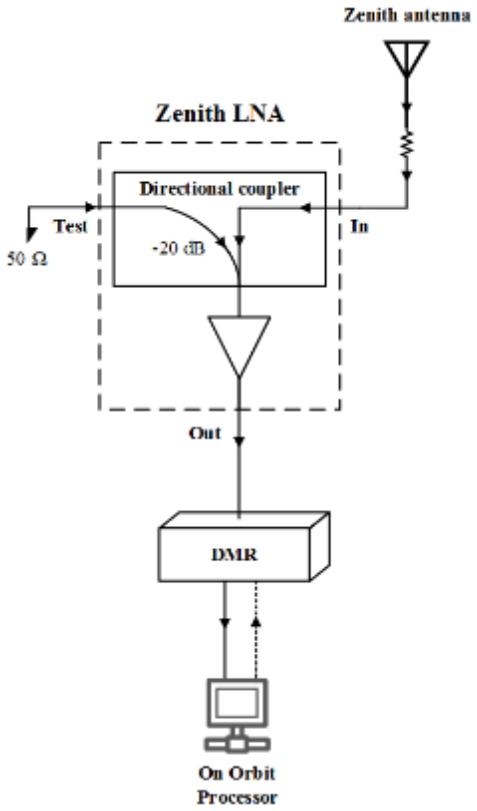

(a)

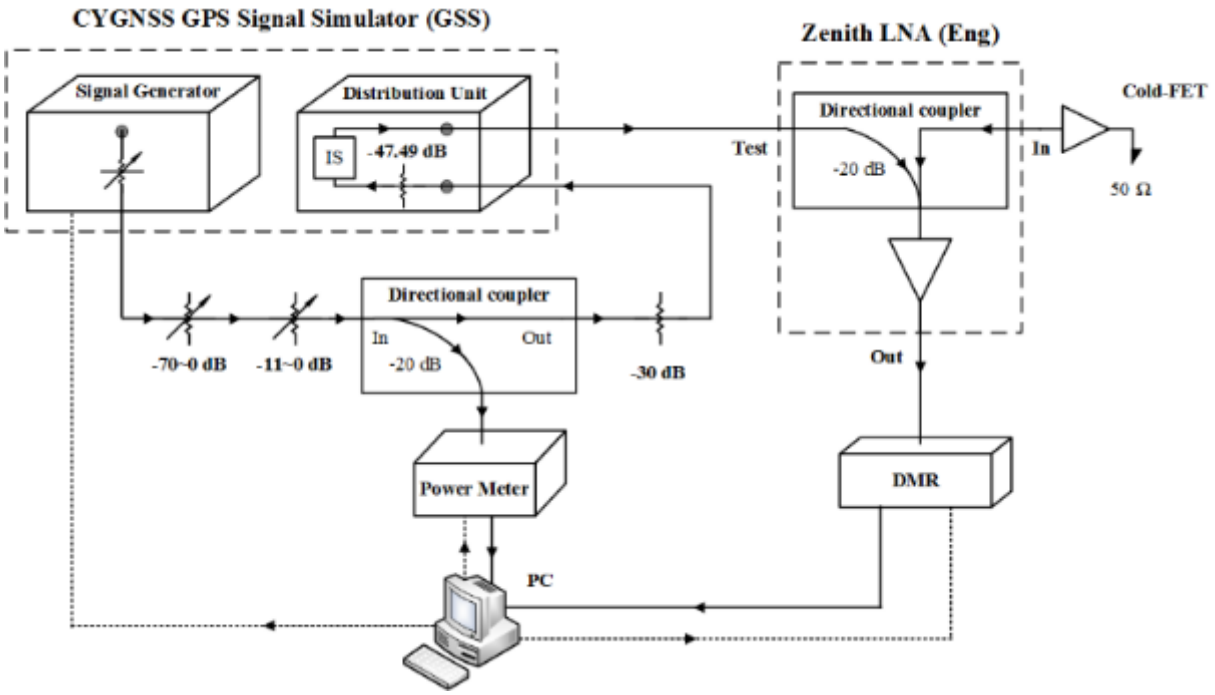

(b)

Figure III.15 (a). On-orbit configuration of the CYGNSS zenith measurement; (b). Configuration of DMR-GSS end-to-end calibration experiment

Two variable attenuators (70 dB and 11 dB) are used to adjust the power level of the input signal. The input power to the DMR is known, and the output counts are measured, as shown in Figure III.16. A second-order power series is fit to the calibration data to convert the raw engineering counts measured by the receiver into power in dBW referenced to the input port of the DMR. After incorporating the gain of the LNA and cable loss, the received power referenced to the output port of the antenna can be determined.

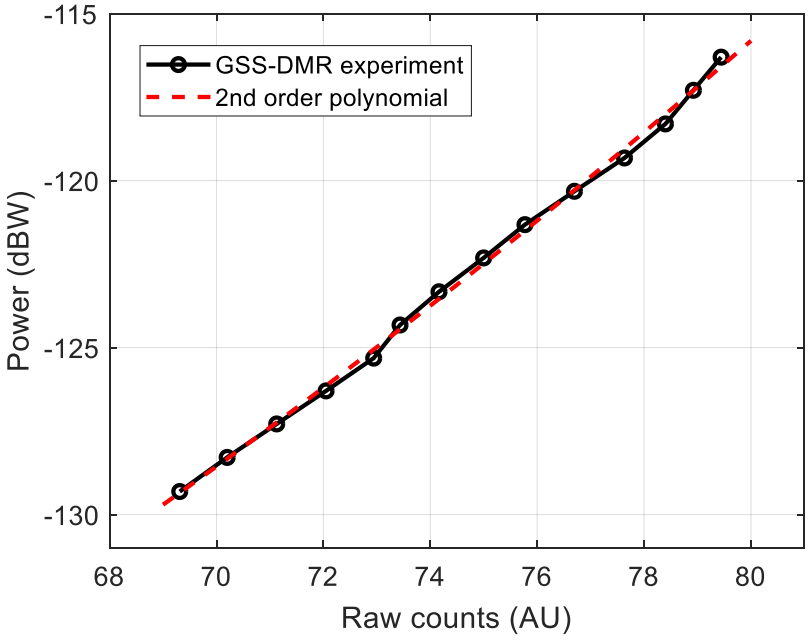

Figure III.16 A second-order polynomial fitting to the DMR-GSS calibration data

A second order power series expression was determined from this experiment, as given in Table III-3. It converts the raw counts (C_Z in dB) measured by the navigation receiver into power at the input port of the receiver (P_Z in dB watts) as given by

$$P_Z = \mathrm{a}C_Z^2 + bC_Z + c \tag{3.4}$$

Table III-3 Zenith counts to power conversion coefficients

Coefficient	Value
a	0.011897
b	-0.50994
c	-1.51160e+02

CHAPTER IV

Measuring GPS EIRP in Real-Time with a Spaceborne Receiver System

4.1 Introduction

As discussed in Subsection 1.5.2, the flex power mode of the Block IIR-M and IIF GPS satellites was developed and implemented to redistribute the transmit power between the individual signal components of the GPS signal for increased protection against jamming in certain regions. From January 27, 2017 to Feb 13, 2020, Block IIF GPS satellites have implemented a geographically driven flex power mode, which enables a ~ 2.5 dB increase and decrease in the L1 C/A code's power with every orbit [109]. Such unpredictable flex power events prevent us from assigning a correct transmit power level for Block IIF satellites. Therefore, observations from all IIF satellites are flagged out in the v2.1 dataset. This reduces the CYGNSS measurement coverage by approximately 37% and affects the revisit time of the mission. This will limit the mission's potential in many high-level scientific applications, for example, tracking hurricane intensity and flood inundation after landfall, resolving diurnal variations in ocean surface winds and heat flux, and capturing the rapid dry down response of soil moisture to extreme precipitation events.

The secondary error of GPS EIRP estimate comes from the transmit antenna gain. The published pre-launch measured antenna patterns are not sufficient for the CYGNSS Level 1 calibration. The retrieved GPS antenna gain patterns using the spaceborne range measurement demonstrate the azimuthal asymmetry of GPS antenna gain. This brings additional error if using

an off-boresight azimuthal averaged estimate or if not properly corrected for spacecraft yaw attitude maneuvers [116], [117], [131]. The limited knowledge and possible measurement error of the directivity reduce confidence in the estimate of antenna gain and, thus, the GPS EIRP. An absolute calibration algorithm would require replacement of simple off-boresight models with full GPS antenna pattern estimates and GPS satellite yaw state modelling for each transmitter. It is extremely difficult to estimate the full pattern using limited ground-based GPS receivers. Also, knowledge of the GPS satellite orientation is complicated by its recurring yaw maneuvers. It is possible but would be rather cumbersome to implement and would increase data latency in order to obtain the necessary GPS satellite yaw states.

To summarize, a calibration technique is needed to solve or mitigate the above two issues with GPS EIRP knowledge. It should be able to 1) detect and correct for power fluctuations in all GPS transmitters and 2) reduce calibration errors due to the azimuthal asymmetry of the GPS antenna gain pattern.

Much of the work reported in this chapter has been derived from [132]–[134].

4.2 Methodology

4.2.1 Overview of the Dynamic EIRP Calibration

CYGNSS L1a calibration converts each bin in the Level 0 DDM from raw counts to units of watts. Then the CYGNSS L1b calibration generates two data products associated with each L1a DDM: 1) a bin-by-bin calculation of the surface BRCS, or σ, and 2) bin-by-bin values of the effective scattering areas. With other metadata, these two intermediate variables are used to compute the NBRCS [104] as

$$\bar{\sigma}(\hat{\tau},\hat{f}) = \frac{P_g(\hat{\tau},\hat{f})(4\pi)^3}{E_S\lambda^2 G_S^R R_S^{Total}} \tag{4.1}$$

where $P_g(\hat{\tau}, \hat{f})$ is the Level 1a calibrated signal power at a specific delay ($\hat{\tau}$) and Doppler ($\hat{f}$) bin, E_S is the GPS EIRP in the direction of the specular reflection point, λ is the wavelength for GPS L1 signals, G_S^R is the receiver antenna gain at the specular point, and R_S^{Total} is the total range loss from the transmitter to the surface plus the surface to the receiver at the specular point.

Dynamic EIRP calibration uses measurement made by the CYGNSS direct (zenith) channel to solve for GPS EIRP in the direction of the zenith antenna (E_Z). E_S is then estimated from E_Z and a correction is made to the Level 1 NBRCS calibration. The measurement geometry is illustrated in Figure IV.1.

In this way, 8 CYGNSS zenith receivers are converted into 8 real-time GPS power monitor systems. By making direct, temporally coincident estimates of the GPS EIRP, this dynamic EIRP calibration algorithm can instantaneously detect and correct for power fluctuations in all GPS block transmitters. This approach also reduces errors due to GPS antenna gain azimuthal asymmetry because the azimuthal angles of the zenith and nadir propagation paths are the same.

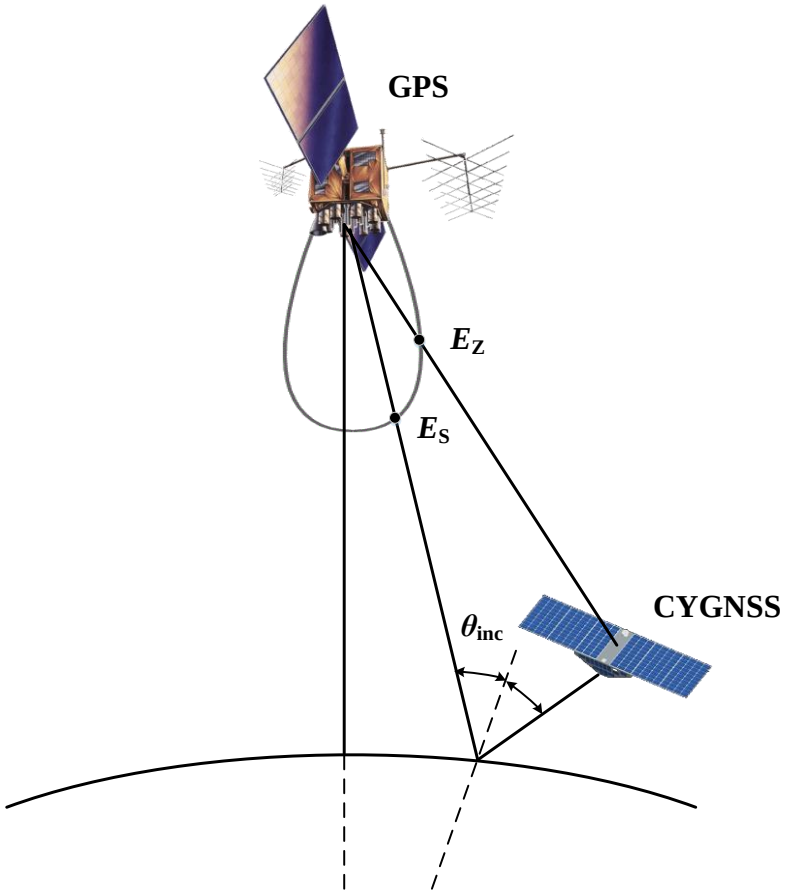

Figure IV.1 Concept of the dynamic EIRP calibration algorithm (GPS antenna nominally points toward center of Earth). E_Z and E_S are the GPS EIRP in the direction of the CYGNSS satellite and the specular reflection point, respectively

4.2.2 Calibration of the CYGNSS Zenith Signal

The zenith channel of the GPS receiver on CYGNSS was originally intended for navigation only, so there was no calibration capability included to convert the raw counts of the direct navigation signal into power in watts. In addition, the zenith channel contains an automatic gain control (AGC) feature. Although the AGC ensures a consistent signal power level for navigation data processing purposes, the state of the AGC at any given time is not recorded by the receiver, which prohibits calibration of the direct-path GPS signal power. As of August 1, 2018, the AGC feature has been disabled, and a constant gain value used, for all 8 CYGNSS flight models (FMs).

Prior to this change, the ability to perform navigation functions properly over the full dynamic range of expected signal levels was verified.

Calibration of the zenith navigation receiver for power measurements was done using an engineering model (EM) of the CYGNSS receiver together with a GPS signal simulator (GSS) to emulate the on-orbit measurements [129]. A second order power series expression was determined from the EM+GSS measurements, as given in Table III-3. It converts the raw counts (C_Z in dB) measured by the zenith channel of the receiver into power at the input port of the receiver (P_Z is originally computed in dB watts and then converted to a linear scale). The received power referenced to the output port of the zenith navigation antenna, P_R, can be determined from P_Z after correcting for the gain of the zenith low noise amplifier (LNA) G_{LNA} according to

$$P_R = \frac{P_Z}{G_{LNA}(T_{LNA})} \tag{4.2}$$

where T_{LNA} is the temperature of the LNA. G_{LNA} is calculated using a pre-launch look-up table (LUT) of gain vs. physical temperature.

4.2.3 Characterization of CYGNSS Zenith Antenna Pattern

The accuracy of the estimated GPS EIRP depends on knowledge of the CYGNSS zenith antenna gain pattern, $G_R(\theta, \phi)$. Prior to launch, antenna measurements were performed in an anechoic chamber using a zenith antenna installed on an approximate CYGNSS satellite mock-up. Those measurements indicated that the antenna pattern was extremely sensitive to coupling and multipath from nearby satellite structures (e.g., the solar panels and other electrical elements) which were not deployed or positioned with sufficient repeatability between spacecraft. For this reason, it was concluded that the chamber measurements would be inadequate to accurately

represent the CYGNSS zenith antenna patterns on the actual satellites and an on-orbit determination of the patterns would be necessary.

The CYGNSS zenith antennas were characterized on-orbit using a large collection of CYGNSS measurements of the direct GPS signal strength made by a subset of the GPS satellites for which the transmit power level does not change appreciably over time. Individual CYGNSS antenna gain patterns were determined for each of the eight satellites, as described in [129]. One example of the resulting pattern (for CYGNSS FM 1) is shown in Figure IV.2 (a). Since the CYGNSS receivers only record direct measurements from GPS satellites for which a reflected measurement is also made, the measurement density used to estimate the antenna patterns is not uniformly distributed across the pattern. An example measurement density is shown in Figure IV.2 (b). Only portions of the antenna pattern with high sampling density are used for Level 1 calibration of the reflected signal.

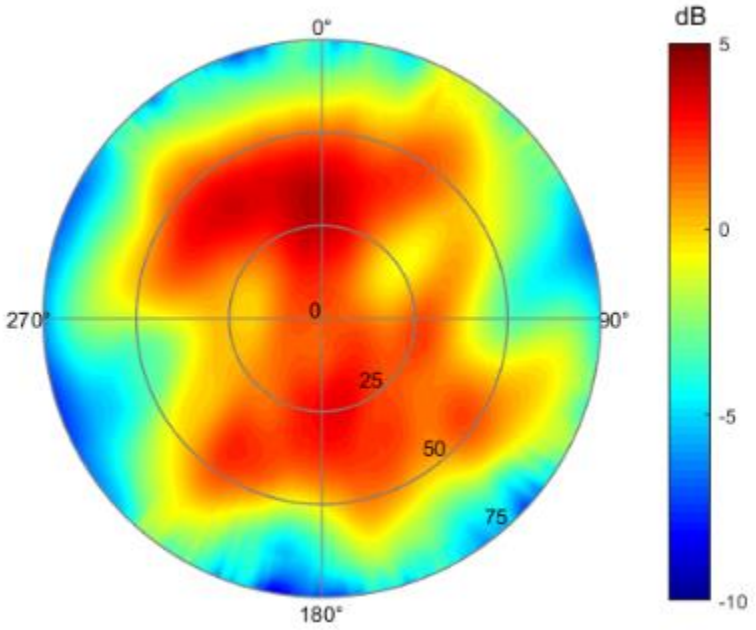

(a)

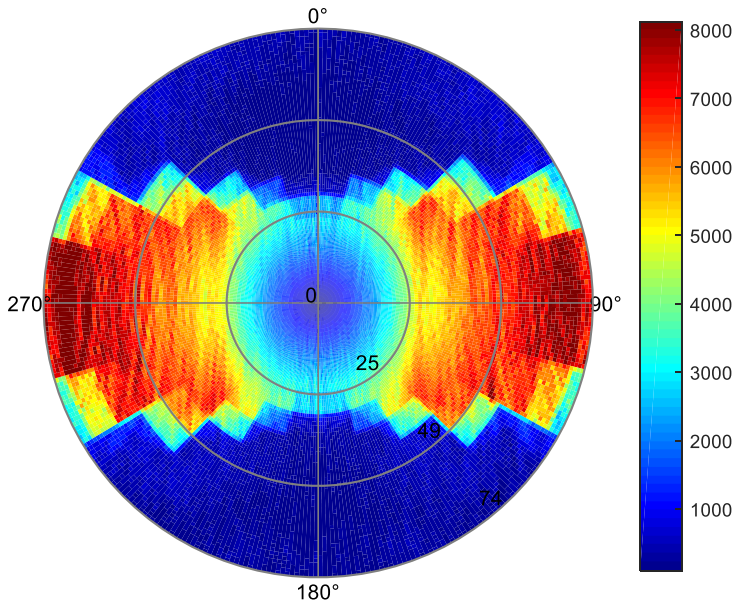

(b)

Figure IV.2 (a) Gain pattern of the CYGNSS FM 1 zenith antenna that receives direct GPS signals; (b) Sampling density of direct-signal GPS measurements used to estimate the zenith antenna gain pattern

4.2.4 Estimating GPS EIRP toward the CYGNSS Satellite

The Friis transmission equation can be rearranged to solve for E_Z, the GPS satellite EIRP in the direction of the CYGNSS satellite, as

$$E_Z = \frac{(4\pi R)^2}{\lambda^2} \frac{P_R}{G_R(\theta_R, \phi_R)} \tag{4.3}$$

where R is the range from the GPS satellite to the CYGNSS satellite, λ = 0.19 m is the GPS signal wavelength, P_R is the received power of the GPS signal as calculated by (4.2), G_R is the gain pattern of the receive antenna, and θ_R and ϕ_R are the off-boresight and azimuthal angles of the GPS satellite in the receive antenna reference frame.

4.2.5 Zenith-to-Specular Ratio (ZSR) Function

The time varying EIRP for a particular GPS satellite is the product of its transmit power P_T at time t and its realized antenna gain $G_T(\theta, \phi)$,

$$E(t, \theta, \phi) = P_T(t) G_T(\theta, \phi) \tag{4.4}$$

where the elevation and azimuth angles (θ, ϕ) specify a direction in the GPS antenna reference frame.

For the geometric arrangement of the GPS satellite, CYGNSS satellite, and specular reflection point depicted in Figure IV.1, we define the zenith-to-specular ratio (ZSR) as the ratio of the GPS satellite EIRP in two specific directions,

$$ZSR \triangleq \frac{E_Z}{E_S} = \frac{E(t, \theta_Z, \phi_Z)}{E(t, \theta_S, \phi_S)} \tag{4.5}$$

where (θ_Z, ϕ_Z) is the direction to the CYGNSS satellite and (θ_S, ϕ_S) is the direction to the specular reflection point.

Ultimately, our goal is to determine E_S, the GPS EIRP in the direction of the specular reflection point, from measurements of E_Z, the GPS EIRP in the direction of the CYGNSS satellite. To accomplish this, we develop an approximation of the ZSR function, $\widehat{ZSR}$, and use it to scale E_Z, as given by

$$E_S \simeq \frac{E_Z}{\widehat{ZSR}} \tag{4.6}$$

The derivation of $\widehat{ZSR}$ is detailed below.

To begin, substituting (4.4) into (4.5) removes the dependence on GPS transmit power. The ZSR is equal to the time-independent ratio of GPS antenna gain in two directions, or

$$ZSR(\theta_Z, \theta_S, \phi_Z, \phi_S) = \frac{P_T(t) G_T(\theta_Z, \phi_Z)}{P_T(t) G_T(\theta_S, \phi_S)} = \frac{G_T(\theta_Z, \phi_Z)}{G_T(\theta_S, \phi_S)} \tag{4.7}$$

Next, two approximations are made to simplify the form of (4.7). First, it is observed that, for specular reflection geometries, the azimuth angles ϕ_Z and ϕ_S are nearly identical. Therefore, we can rewrite the ZSR as a function of a single azimuth angle ϕ, or

$$ZSR(\theta_Z, \theta_S, \phi_Z, \phi_S) \simeq ZSR(\theta_Z, \theta_S, \phi) \tag{4.8}$$

where $\phi = \phi_Z = \phi_S$.

Second, it is observed that both of the elevation angles, θ_Z and θ_S, are (within a small fraction of a degree) related in a one-to-one fashion to the specular incidence angle θ_{inc}, or

$$\theta_Z \simeq \theta_Z(\theta_{inc}) \tag{4.9}$$

$$\theta_S \simeq \theta_S(\theta_{inc}) \tag{4.10}$$

Note that the relationships in (4.9) and (4.10) are only valid for a limited range of CYGNSS satellite altitudes. As CYGNSS satellite altitudes change over the life of the mission, the functional relationships may need to be recalculated. Using (4.9) and (4.10), the ZSR is approximated as

$$ZSR(\theta_Z, \theta_S, \phi_Z, \phi_S) \simeq \frac{G_T(\theta_Z(\theta_{inc}), \phi)}{G_T(\theta_S(\theta_{inc}), \phi)} \tag{4.11}$$

At this point, the ZSR is expressed as a function of two parameters, the specular incidence angle, θ_{inc}, and the azimuthal angle of the specular reflection point in the GPS antenna reference frame, ϕ. If one examines the published GPS antenna patterns, they can be seen to exhibit significant variation in both elevation and azimuth. However, the relative dependence of gain on elevation at a fixed azimuth angle does not change significantly with azimuth. For that reason, the ZSR function is more weakly dependent on azimuth angle than is the gain itself. This suggests that the azimuthally dependent ZSR function in (4.11) can be approximated by its average value over all azimuth angles, as given by

$$\widehat{ZSR}(\theta_{inc}) \triangleq \frac{1}{2\pi} \int_0^{2\pi} \frac{G_T(\theta_Z(\theta_{inc}), \phi)}{G_T(\theta_S(\theta_{inc}), \phi)} d\phi \tag{4.12}$$

In practice, the integral in (4.12) is performed numerically by averaging over 36 discrete cuts of the patterns in 10 deg azimuthal increments.

The approximated ZSR is now a function of a single parameter, θ_{inc}, the specular incidence angle. It is evaluated separately for each GPS satellite. The resulting ZSR functions for all GPS satellites are shown in Figure IV.3, color coded by block type and antenna design. Commonality in their behavior for a given block type and antenna design can be clearly seen. These ZSR functions were calculated using the pre-launch measured GPS antenna patterns from [115]. For this work, the pattern data was smoothed and interpolated by fitting a power series polynomial to each azimuth cut of the published pattern (36 cuts in total).

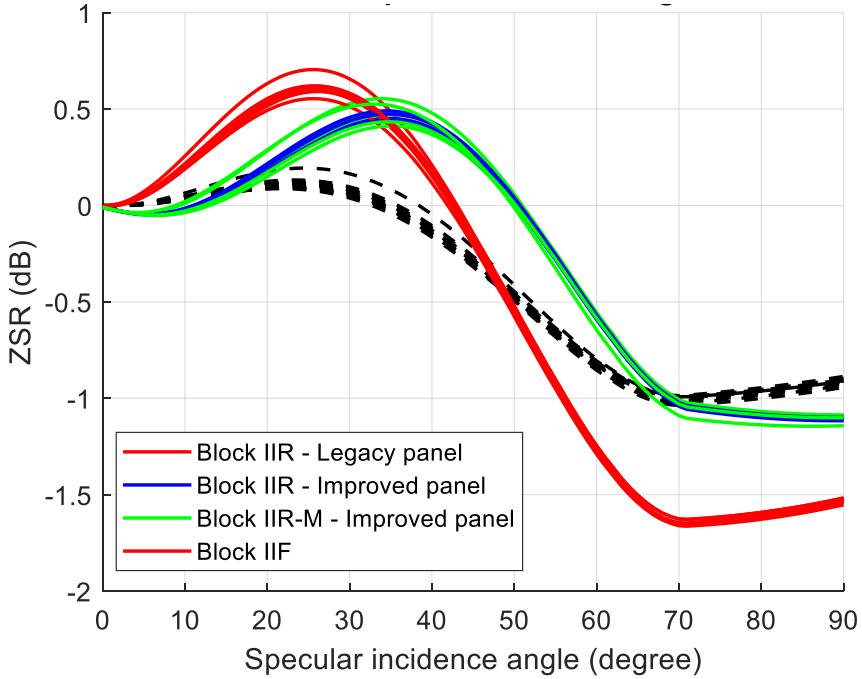

Figure IV.3 Calculated ZSR functions for each GPS satellite (grouped based on satellite block type)

One key aspect of the ZSR approximation in (4.12) is that it can be used without knowledge of the GPS satellite yaw state, which is difficult to obtain in practice. The accuracy of the

approximation relies on the weak azimuthal dependence of the ZSR function given in (4.11). To demonstrate the validity of the approximation, Figure IV.4 quantifies the azimuthal variation of the ZSR. Although results are only shown for a single GPS satellite, spacecraft vehicle number (SVN) 56, the results for other SVNs are similar. Azimuthal variations in the ZSR (solid blue curve) are characterized by the standard deviation (taken in dB) over all azimuth angles at a particular specular incidence angle. It can be observed that the standard deviation of the error is very small and is ~ 0.1 dB or less over most incidence angles. For comparison, Figure IV.4 also shows the standard deviation of the GPS antenna gain pattern (dashed red curve), which is mapped to specular incidence angle for comparison with the ZSR function. The standard deviation of the gain pattern can be seen to rise to 0.2 dB at ~20 deg incidence and 0.3 dB at ~55 deg incidence. If the GPS antenna gain pattern was used directly to estimate EIRP and the yaw state of the GPS satellite was not known, these standard deviation values would represent 1-sigma uncertainties in the antenna gain and, ultimately, in the derived science data products. The azimuthal dependence of the ZSR is significantly weaker than that of the antenna gain. For example, at 55 deg. incidence, the standard deviation is ~0.1 dB, or roughly one-third that of the gain. By using the ZSR function rather than the antenna gain directly, the sensitivity of EIRP estimates to lack of knowledge of the yaw state of a GPS satellite has been reduced by roughly a factor of 3.

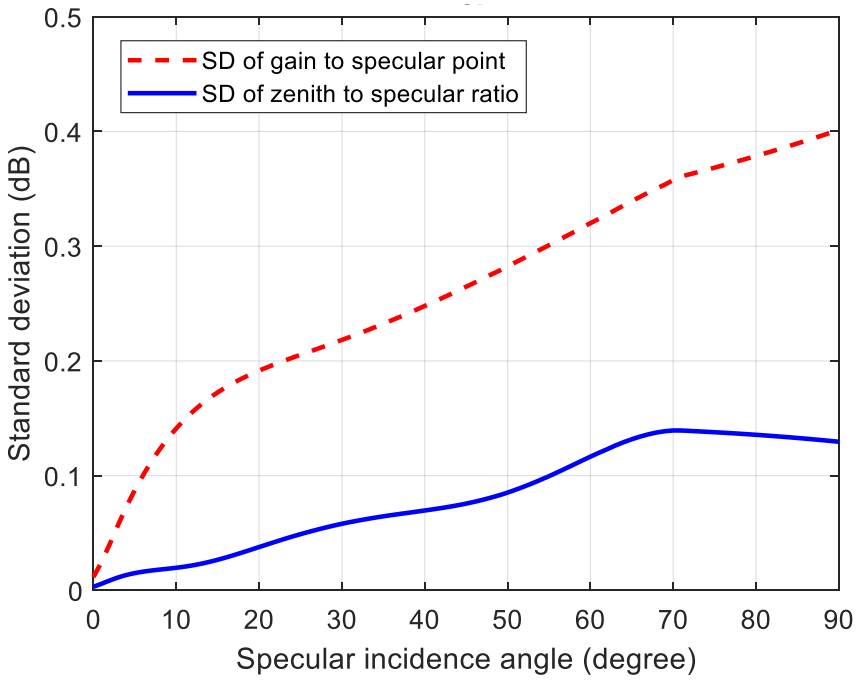

Figure IV.4 Standard deviation of the azimuthal variation of the ZSR function (blue) and GPS satellite gain pattern (dashed red) as a function of specular incidence angle

4.2.6 Estimating GPS EIRP toward the Specular Point

The estimated GPS satellite EIRP in the specular point direction is calculated as

$$E_S = \frac{E_Z}{\widehat{ZSR}(\theta_{inc})} \tag{4.13}$$

By combining (4.2), (4.3) and (4.13), E_S can be expressed as

$$E_S = \frac{(4\pi R)^2}{\lambda^2} \frac{P_Z}{G_{LNA}(T_{LNA}) G_R(\theta_R, \phi_R) \widehat{ZSR}(\theta_{inc})} \tag{4.14}$$

and is used in the CYGNSS L1b calibration algorithm to estimate NBRCS from the CYGNSS measurements using (4.1).

4.3 Error Analysis of EIRP Estimate

Analysis of the uncertainty associated with estimates of the GPS EIRP are made in two ways, using a bottom-up decomposition of the estimation algorithm into its component sources of

error and by analyzing Monte Carlo trials of the end-to-end computation. In both cases, the individual sources of error are assumed to be independent and uncorrelated.

4.3.1 Quantifying Error Terms

The terms in (4.14) which are subject to errors are defined below and their standard deviations are listed in Table IV-1:

1) ΔR: Error in knowledge of the distance between the GPS transmitter and the zenith receiver. This is primarily due to the errors in the accuracy of the positioning.

2) ΔP_z: Error in the converted zenith power at the DMR input port. This is due to errors in the raw counts C_Z and the second-order polynomial coefficients derived from the DMR-GSS calibration experiment.

3) ΔG_{LNA}: Error in the zenith receiver gain. This is due to errors in the measured amplifier temperature and in the pre-launch look up table of gain vs. physical temperature.

4) ΔG_R: Error in the zenith antenna gain. This is primarily due to errors in the pattern estimation procedure and in the interpolation process.

5) ΔZSR: Error in the GPS antenna ZSR function. This is due to errors in the gain pattern, the mapping from the GPS off-boresight angles to the specular incidence angle, and the azimuthal variability of ZSR functions. Note that ΔZSR depends on incidence angle and a typical value is selected for the range of incidence angles with highest density of CYGNSS observables.

Table IV-1 Error analysis input parameters

Error Term	1-sigma Error Magnitude
ΔR	10 m
ΔP_z	0.18 dB
ΔG_{LNA}	0.1 dB
ΔG_R	0.2 dB
ΔZSR	0.15 dB

4.3.2 Root of Sum of Squares (RSS) Error

Using the error analysis approach in [104], [135], the RSS of the individual error sources can be calculated as

$$\Delta E_S = \left[\sum_{i=1}^{5} [E(q_i)]^2\right]^{1/2} \tag{4.15}$$

where q_i is the respective error parameter of the five variables in (4.14), and the individual error terms can be estimated by taking the partial derivative of the equation, such that each error team can be quantized as

$$E(q_i) = \left|\frac{\partial E_s}{\partial q_i}\right| \Delta q_i \tag{4.16}$$

where each term can be expressed as

$$E_S(R) = 2R\frac{(4\pi)^2}{\lambda^2}\frac{P_Z}{G_{LNA}G_R}\frac{1}{ZSR}\Delta R \tag{4.17a}$$

$$E_S(P_Z) = \frac{(4\pi R)^2}{\lambda^2}\frac{1}{G_{LNA}G_R}\frac{1}{ZSR}\Delta P_Z \tag{4.17b}$$

$$E_S(G_{LNA}) = \frac{(4\pi R)^2}{\lambda^2}\frac{P_Z}{G_{LNA}^2 G_R}\frac{1}{ZSR}\Delta G_{LNA} \tag{4.17c}$$

$$E_S(G_R) = \frac{(4\pi R)^2}{\lambda^2}\frac{P_Z}{G_{LNA}G_R^2}\frac{1}{ZSR}\Delta G_R \tag{4.17d}$$

$$E_S(ZSR) = \frac{(4\pi R)^2}{\lambda^2}\frac{P_Z}{G_{LNA}G_R}\frac{1}{ZSR^2}\Delta R \tag{4.17e}$$

It is noted that the error terms in Table IV-1, except ΔR, are relative errors. Let $\Delta R = \alpha_R R$, $\Delta P_z = \alpha_P P_z$, $\Delta G_{LNA} = \alpha_{GLNA}\, G_{LNA}$, $\Delta G_R = \alpha_{GR} G_R$, $\Delta ZSR = \alpha_{ZSR} ZSR$, and (4.17) can be written as

$$E_S(R) = 2\alpha_R E_S \tag{4.18a}$$

$$E_S(P_Z) = \alpha_P E_S \tag{4.18b}$$

$$E_S(G_{LNA}) = \alpha_{GLNA} E_S \tag{4.18c}$$

$$E_S(G_R) = \alpha_{GR} E_S \tag{4.18d}$$

$$E_S(ZSR) = \alpha_{ZSR} E_S \tag{4.18e}$$

Therefore, the relative error of E_S can be calculated as

$$\frac{\Delta E_S}{E_S} = \sqrt{4\alpha_R^2 + \alpha_P^2 + \alpha_{GLNA}^2 + \alpha_{GR}^2 + \alpha_{ZSR}^2} \tag{4.19}$$

The error coefficient for the range α_R is calculated using 1 day's data measured by CYGNSS flight model (FM) 1. Because the range *R* between GPS and CYGNSS satellites is of the order of 10^7 meter, this error is extremely small. The final RSS error of the EIRP estimate to specular point is 0.3185 dB.

4.3.3 Error Estimate Using Monte Carlo Simulation

To independently verify the RSS error approach, a Monte Carlo simulation is also conducted. Error sources are assumed to be independent and uncorrelated. Random noise is generated using a Gaussian distribution with zero-mean and 1-σ uncertainty (error magnitude in Table IV-1). The noise is added to each variable and input to (4.14) to calculate the model prediction. The population of model outcomes is then analyzed to determine the overall error.

A single estimate of the standard deviation of the specular EIRP, E_S, is derived from 10^6 realizations of (4.14). This is then repeated 10^4 times and those estimates are averaged together. The final error estimate of E_S using this Monte Carlo approach is 0.3239 dB, which agrees closely with the RSS approach.

4.3.4 Error Analysis Discussion

The two approaches to error analysis agree well, with both estimating ~0.32 dB relative error. This reduces the 0.4 dB error term of $E(P_T) + E(G_T)$ in v2.1 L1 calibration [104] by about 20%. Besides, the 0.4 dB error does not consider flex power events which can introduce much larger errors, thus the improvement could possibly be larger.

It should be noted that: 1) the error term is dependent on the specular incidence angle because the ZSR function has a dependence on the geometry; 2) there are very small errors caused by the empirical mapping of the two GPS off-boresight angles to the specular incidence angle; 3) the antenna gain patterns of the CYGNSS zenith antenna and GPS antenna are retrieved using measured direct signal, so there may exist interdependent relationships between these variables. These issues will be studied and investigated as future work.

4.4 Calibration of GPS EIRP

4.4.1 Detection of GPS Flex Power Events

Figure IV.5 shows an example of multiple ground tracks of E_Z, the EIRP toward the zenith antenna, for observations by CYGNSS FM01 of GPS SVN 63 transmissions. The color scale denotes the EIRP in dBW. A flex power change of around 2.5 dB is clearly evident. The repeatability of these flex power events over a long time span demonstrates that it is a

geographically-driven commanded change, as shown in [109]. This also demonstrates that the CYGNSS zenith signal, as a spaceborne power monitor system, provides a measurement of flex power that is of comparable accuracy to the two ground-based GPS stations.

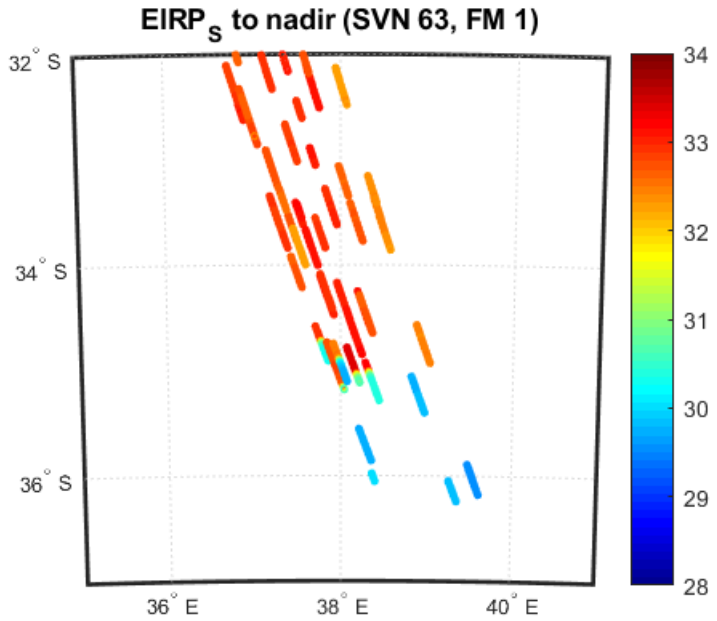

Figure IV.5 EIRP to zenith E_Z estimated using the zenith signal

4.4.2 The Global Map of GPS EIRP

The geolocation of GPS flex power events can be illustrated by considering the global distribution of EIRP measured by CYGNSS. For Block IIF SVs, there are two flex power modes: mode 1 changes the power of both C/A and P(Y) codes, while mode 4 changes the P(Y) code but not C/A code [112].

Figure IV.6 shows a global map of GPS EIRP to the specular point, E_s, for SVN 68, a block IIF SV, running in flex power mode 1 (Year 2019, DOY 276-365) and 4 (Year 2020, DOY 46-135), respectively. The estimated GPS EIRPs measured by all 8 CYGNSS FMs are binned based on the geolocation of the specular point and averaged in 2 deg latitude by 4 deg longitude

cells with all specular incidence angles included. In Figure IV.6 (a), there are distinct levels of EIRP over different regions, which are caused by the flex power mode 1 as described in [112]. This agrees very well with the flex power mode detected by DLR's independent measurement in [109]. In Figure IV.6 (b), when the power of the C/A code does not change with every orbit, the geographical dependence disappears. Note that this EIRP global map is for all specular incidence angles, so it includes the GPS off-boresight angle for the entire range of the Earth service volume (13.8 degrees off-boresight). That causes the variations in the observed EIRP.

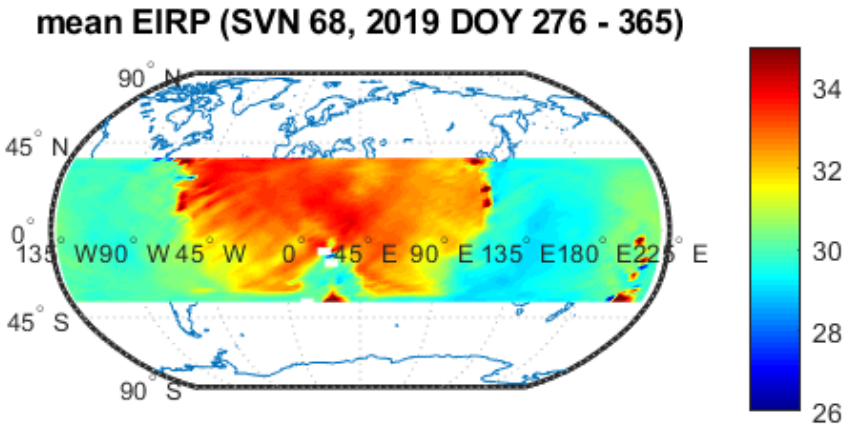

(a)

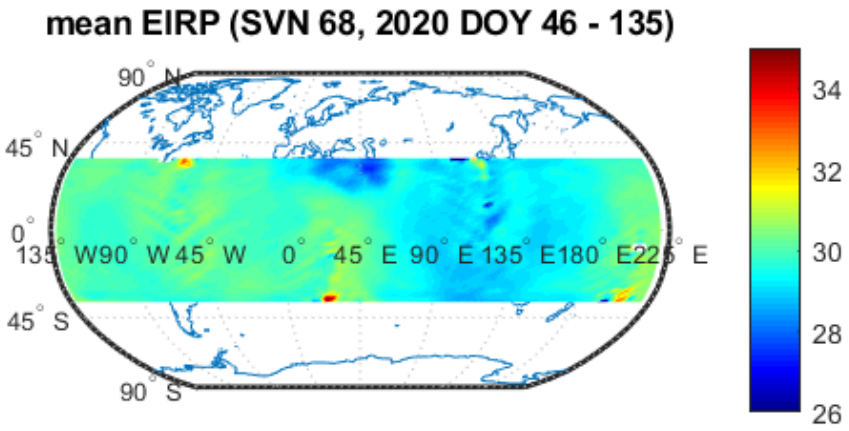

(b)

Figure IV.6 Average map of estimated EIRP to the specular point of GPS SVN 68: (a). Flex power mode 1, Year 2019 DOY 276 - 365; (d) Flex power mode 4, Year 2020 DOY 46 - 135

4.5 Impacts on CYGNSS Level 1 Calibration

4.5.1 Case Study of the GPS Flex Power

An example of the impact of a flex power transition (GPS year 2018, DOY 213; measured by CYGNSS FM 7) is shown in Figure IV.7. The GPS transmit power increases by ~ 2.5 dB, as measured by the zenith received power (black dashed line).

In Figure IV.7, the nadir science measurements are over open ocean, which has a relatively stable surface wind speed (~7 m/s). The red line shows the version 2.1 (v2.1) calibrated Level 1 NBRCS (using the static LUT for the GPS EIRP estimation) and features an abrupt change as the zenith power changes. The non-physical behavior of the NRBCS shows that the change in transmit power has not been correctly accounted for. The version 3.0 (v3.0) NBRCS (using the dynamic EIRP calibration) is shown to be insensitive to the change in transmit power. Note that measurements made during a flex power event, when the EIRP is rapidly changing, are flagged and removed by data quality control measures, causing a gap in the NBRCS time series.

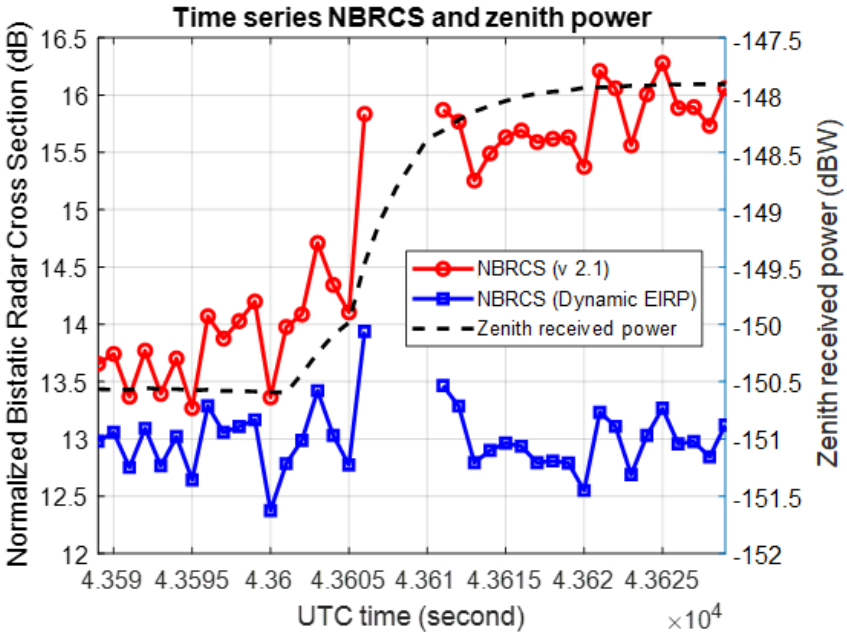

Figure IV.7 A case study of the NBRCS calibration during the GPS flex power

4.5.2 Time-Series Plot of the Level 1 NBRCS

Figure IV.8 presents a time-series daily average of the v3.0 GPS EIRP and NBRCS with signal source SVN 68 (Block IIF) from Year 2018 DOY 213 to Year 2020 DOY 319. Clearly, when the flex power mode changes from mode 1 to mode 4 on February 14, 2020 (as denoted by the red dashed line), the average NRBCS does not show any significant change. This demonstrated that the Block IIF data are correctly calibrated and can be included in the official Level 1 data products for higher level applications.

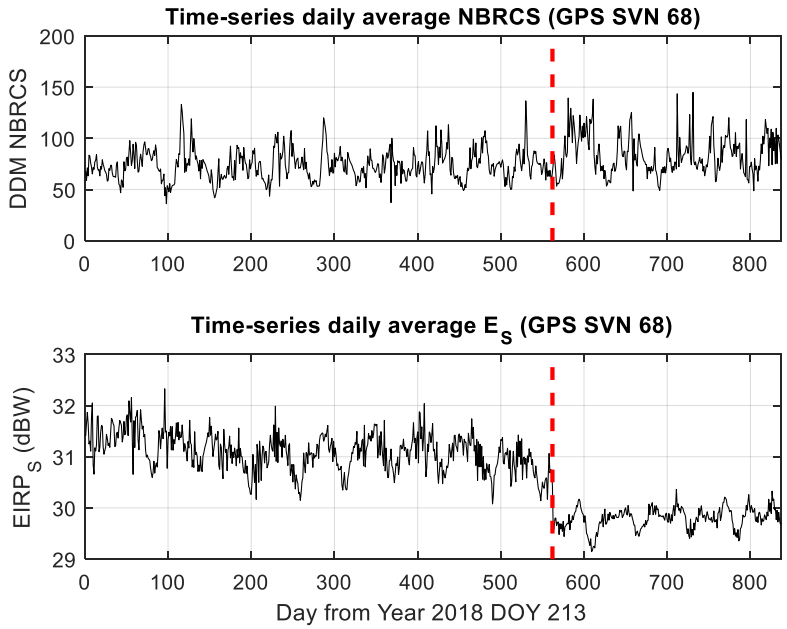

Figure IV.8 Time-series daily average of the GPS EIRP and NBRCS of SVN 68

4.5.3 Improved Daily Coverage with Block IIF Data

Figure IV.9 presents a daily coverage map without and with Block IIF data. Clearly, by recovering observations from the GPS IIF Block satellites and including them in the science data products, CYGNSS provides more nearly gap-free measurements for improved science data coverage.

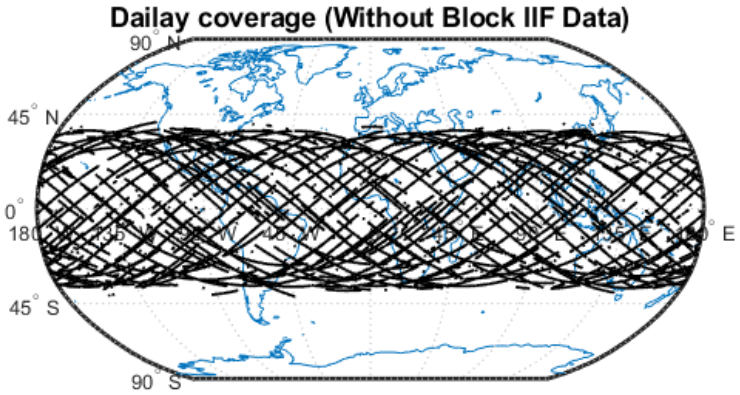

(a)

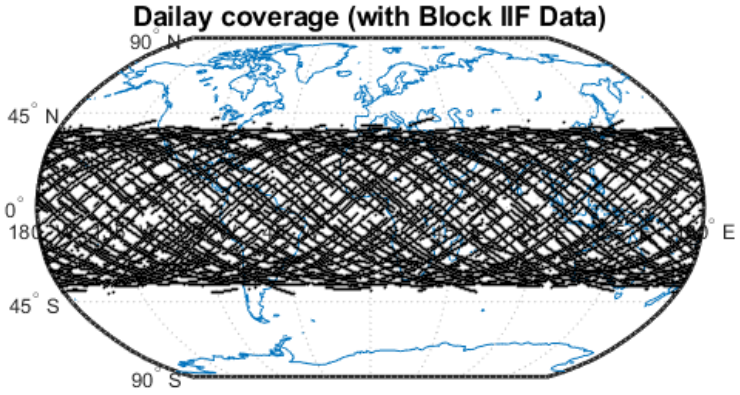

(b)

Figure IV.9 Daily coverage of CYGNSS measurements (a) Without Block IIF data; (b) With Block IIF data

CHAPTER V

Level 1 End-to-End Calibration Using MSS Inter-Comparison

5.1 Introduction

The objective of this research is to develop an independent Level 1 observables that can be used to diagnose the calibration errors existing in the CYGNSS Level 1 calibration. A correction to the receiver antenna gain pattern was previously derived using anomalies in the NBRCS observations; this correction was applied as part of the V2.1 Level 1 calibration algorithm. However, it is noted that this NBRCS anomaly is considered to be dependent only on the wind speed and specular incidence angle, which may not be true in all cases. It has been demonstrated that the error in wind speeds retrieved from GNSS-Reflectometry (GNSS-R) observations is strongly correlated with the significant wave height (SWH) of the ocean. Hence, there is a necessity to take into account the sea state influence, especially the non-local swell contribution to the ocean surface roughness. A physics-based approach is therefore proposed in this paper to examine potential calibration errors and to further improve the Level 1 calibration. Rather than using the NBRCS anomaly, this approach is based on comparison of the sea surface mss estimated by CYGNSS and a reference mss produced by wave models or in-situ measurements. This method enables us to determine potential anomalies observed in CYGNSS's mss that can then be compared with calibration errors existing in the NBRCS. These studies should help to further improve the calibration quality and the accuracy of Level 2 data products, including both mss and wind speed.

Much of the work reported in this chapter has been published in [136].

5.2 Connection between the BRCS, mss and Surface Elevation Spectrum

GNSS-R sensor measures the specular bistatic scattering from the ocean surface. Usually only the near specular region is used for wind speed retrieval. The measured BRCS is interpreted in terms of the Kirchhoff approximation in the geometrical optics limit (KAGO) [22] (less applicable for winds < 5 m/s)

$$\sigma_0 = \frac{|R|^2}{2\sigma_u\sigma_c} \tag{5.1}$$

where R is the Fresnel reflection coefficient for circular polarization (which is a function of q, weak function of surface temperature and or salinity), $2\sigma_u\sigma_c$ is the surface "mss". "u" and "c" refer to upwind and crosswind, respectively.

The BRCS is proportional to 1/mss, or, more accurately: We can model the up and cross wind mean square slope (mss) as a weighted integration over the sea surface spectrum.

$$\sigma_{s_{u,c}}^2 = \langle s_{u,c}^2 \rangle = \iint\limits_{\kappa<\kappa_*} \kappa_{u,c}^2 \Psi(\vec{\kappa}) d^2\kappa = \int\limits_0^{\kappa_*} k^3 dk \int\limits_{-\pi}^{\pi} \Psi(k,\varphi) \begin{matrix}\cos^2\varphi \\ \sin^2\varphi\end{matrix} d\varphi \tag{5.2}$$

The integration is over wavenumber κ and azimuth, excluding wavenumbers larger than

$$\kappa_* = \frac{2\pi \cos\theta_{inc}}{3\,\lambda} \tag{5.3}$$

where θ_{inc} is the specular incidence angle and λ is the wavelength for the GPS L1 signal.

This means that any waves in the sea surface shorter than this cutoff wavenumber do not contribute in computing the slope variance, meaning, only "long" waves matter. The dependence on the indent angle is shown in Figure V.1.

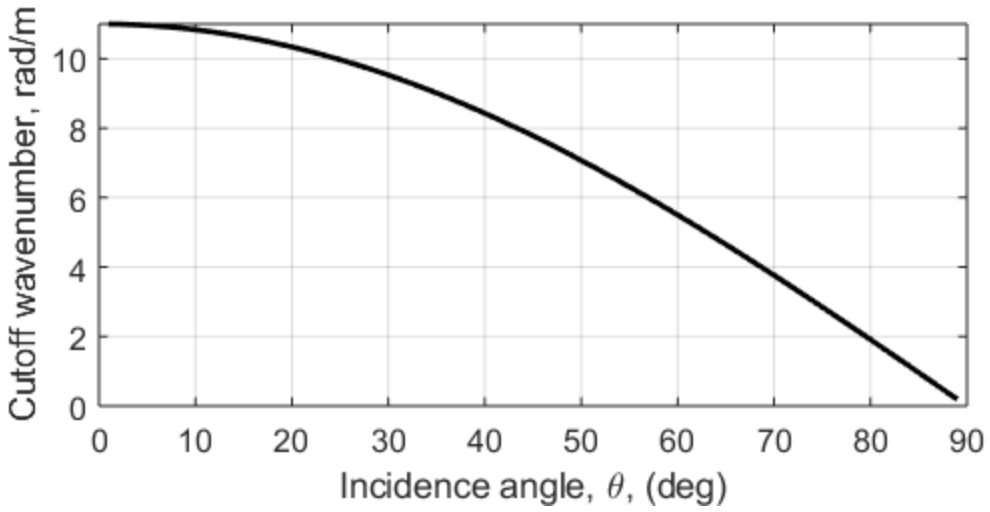

Figure V.1 Cutoff wavenumber's dependence on the incidence angle. Courtesy: Valery Zavorotny

5.3 Modeling a Reference mss: WW3 mss with High-Frequency Tail Extension

The idea is to obtain an mss product either from models or in-situ measurements to compare with the CYGNSS mss as a method for detecting potential calibration errors. One resource is the IFREMER WW3 model predicted mss. However, this WW3 implementation has a fixed cutoff frequency at κ_{WW3} = 2.1 rad/m in resolving the sea surface spectrum [137], [138], while the CYGNSS-observed mss should be sensitive to contributions from sea waves up to the cutoff frequency. Therefore an extension over the high-frequency spectrum tail is needed.

5.3.1 WaveWatch III (WW3) mss

WAVEWATCH III is a third generation wave model developed at NOAA/NCEP. Figure V.2 shows an example of the surface plot of an energy density spectrum showing spectral partitions for windsea and three swell trains. The WW3 mss includes the contributions from the different wave partitions include both windsea and non-local swell.

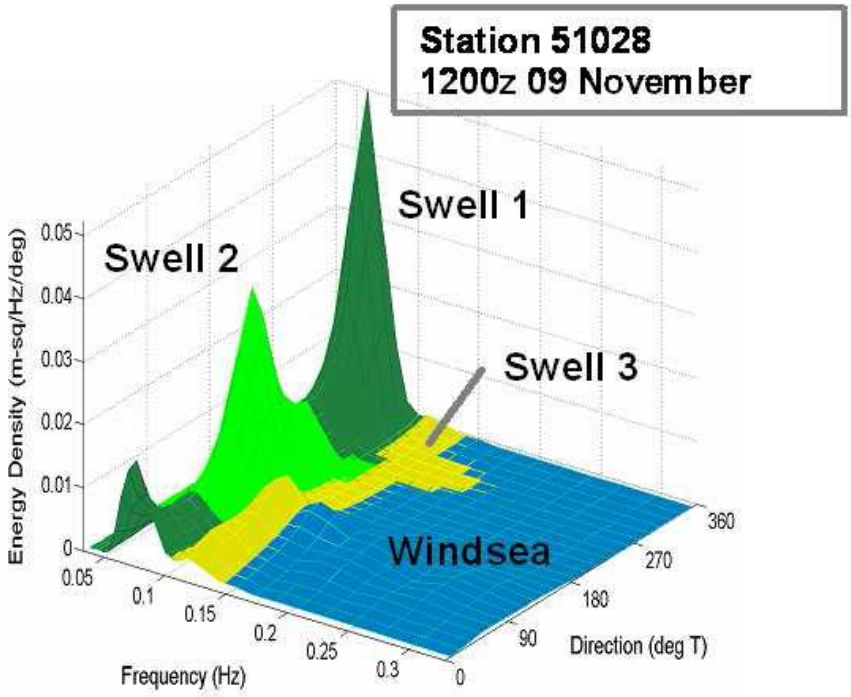

Figure V.2 Surface plot of an energy density spectrum: A snapshot of hindcasted conditions at Christmas Island (NOAA buoy 51028) at 12:00 UTC on November 9, 2000 [137]

The WW3 mss has a clear dependence on the inverse wave age, a parameter describing the sea state development. The inverse wave age Ω could be estimated using

$$\Omega = \frac{U_c}{c_{p0}} = \frac{2\pi U_{10} cos\theta_{ww}}{gT_{p0}} \tag{5.4}$$

where θ_{ww} is the angle between wave and wind directions, and T_{p0} is the wave period at the spectral peak for the wind-sea partition.

5.3.2 Modeling of High Frequency Tail Using Elfouhaily et al. Spectrum

However, this WW3 implementation has a fixed cutoff frequency at κ_{WW3} = 2.1 rad/m in resolving the sea surface spectrum [137], while the CYGNSS-observed mss should be sensitive to contributions from sea waves up to the cutoff wavenumber discussed in Section 5.2. The typical value of κ_{CY} is from 4 to 12 rad/m.

For a typical case, swell portions of the wave spectrum are narrower in wavenumber, have an amplitude that exceeds that of wind generated waves in the same spectral region, and have a peak wavenumber that resides in the low-frequency (long-wave) region. The wind-sea portion of the spectrum in contrast is wider in wavenumber space, but has a smaller amplitude whose peak position is in the high-frequency (short-wave) region [138].

To compare the WW3 and CYGNSS estimated mss, we need to add the portion of wave spectrum (high-frequency 'tail') generated by the local wind from κ_{WW3} to κ_{CY}, represented by the contributions of surface roughness from the blue curve to the magenta or red curves shown in Figure V.3.

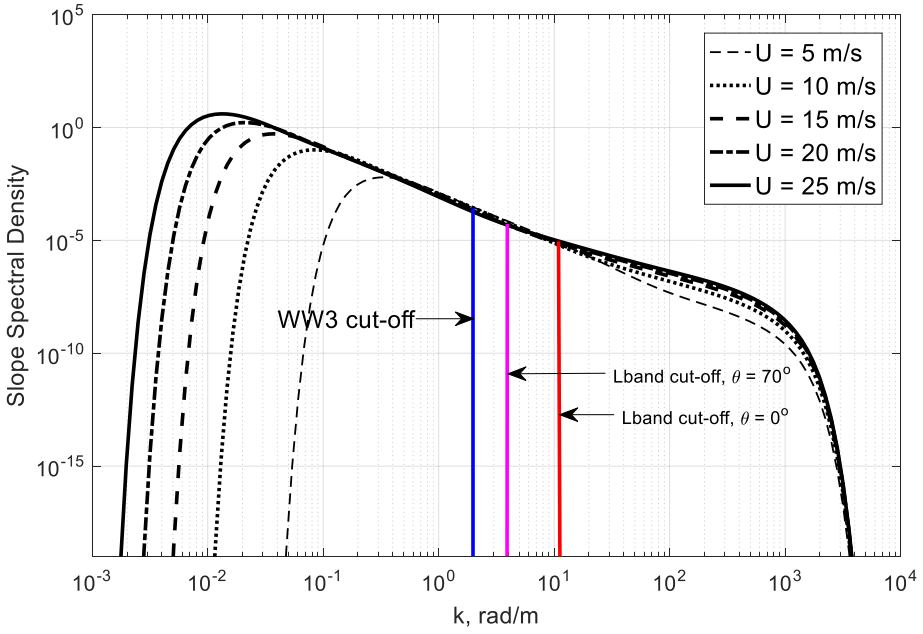

Figure V.3 Slope spectral density for different wind speed conditions (cutoff wavenumbers of WW3 and L-band GNSS-R observations). Courtesy: Valery Zavorotny

Currently, the Elfouhaily et al. spectrum [102] is used to model this spectrum.

$$\Psi_{local}(\vec{\kappa}) = k^{-4}\mathrm{B}(k)\mathrm{D}(k,\phi) \tag{5.5}$$

where *B* is the curvature spectrum and *D* is directional part of the spectrum.

This spectrum is for the waves generated by local wind (2.5 m/s < U_{10}< 24 m/s), and is a function of the fetch; a swell spectrum can be added to capture contributions of any non-local waves.

Three parameters are inputs to the model: the "ground-truth" wind speed (from the ECMWF winds that force the WW3 prediction), the specular incidence angle (determining the cutoff frequency), and the inverse wave age Ω_0 for the wind-sea.

Empirical models of ocean wave spectra predict that the inverse wave age Ω_0 of local wind seas at finite fetch can be larger than the asymptotic value of 0.84 for infinite fetch [102]. The calculation of Ω_0 using wind speeds and wave periods T_{p0} from IFREMER WW3 data on average support this; however, a portion of realizations yield values of Ω_0 smaller than 0.84, which could be caused by uncontrolled swell contribution into the partition 0 (windsea) spectrum and other complicated factors of wind-sea interaction [139]. For those cases, since we are not able to use the Elfouhaily et al. spectrum to generate the local wind spectra, we remove such cases from the datasets used to assess the calibration process.

5.3.3 Modified WW3 mss with High-frequency Tail Extension

The modified WW3 mss is calculated by taking into account the directivity of waves [140] as

$$mss_{mWW3} = 2[mss_{WW3,x}mss_{WW3,y} + mss_{E,x}mss_{E,y} + (mss_{E,x}mss_{WW3,y} + mss_{WW3,x}mss_{E,y})cos^2\Delta\theta + \left(mss_{WW3,x}mss_{E,x} + mss_{WW3,y}mss_{E,y}\right)sin^2\Delta\theta]^{\frac{1}{2}} \quad (5.6)$$

where the subscript 'WW3' means WaveWatch III, 'E' means the modeled high-frequency "tail" mss using the Elfouhaily et al. spectrum, and $\Delta\theta$ is the angular difference between directions of both the wind and the mss distribution.

5.4 mss Ratio for Calibration Diagnostics

The mss ratio (mssR) is calculated as follows:

$$mssR = \frac{mss_{CY}}{mss_{mWW3}} \tag{5.7}$$

The dataset used is a subset of the CYGNSS v 3.0 data from days 001 to 334 for the Year 2019. The mss ratio is calculated for individual GPS PRN and CYGNSS Flight Model (FM) numbers to examine the dependence on these parameters. The ratio is also mapped to the receiver antenna coordinate system and binned 1 by 1 degree, and the average within each bin over the dataset is examined.

5.4.1 mss Ratio for Individual PRN and FM

Figure V.4 shows the mss ratio of CYGNSS FM1 with GPS transmitter PRN11. The histogram shows that there could be potential calibration error on the receive antenna pattern, as patterns are observed in these plots that differ for the starboard and port sides. The mean mssR is calculated using a weighted average by the measurement density. Mean mssR for starboard and port antennas are computed separately.

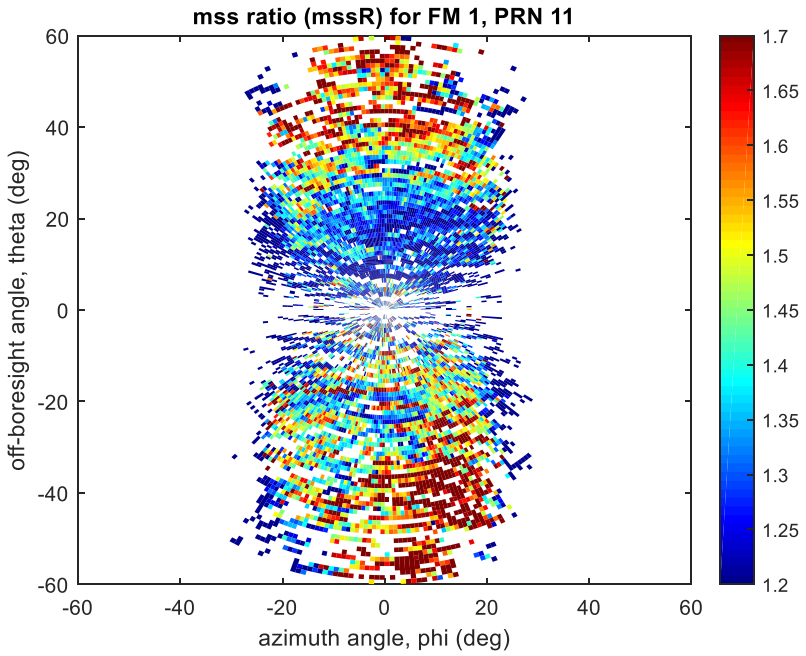

Figure V.4 mssR for FM1/PRN11

5.4.2 Mean mssR for Individual PRN and FM

Figure V.5 shows the mean mssR of starboard and port versus GPS for all CYGNSS flight model (FM), with differing colors labeling distinct FM in this case. We can use them to diagnose possible calibration issues existing in the GPS EIRP and the gain of receiver antenna and receiver system. The differences between the starboard and port channels can be identified through inter-comparison of two mean mssR sets.

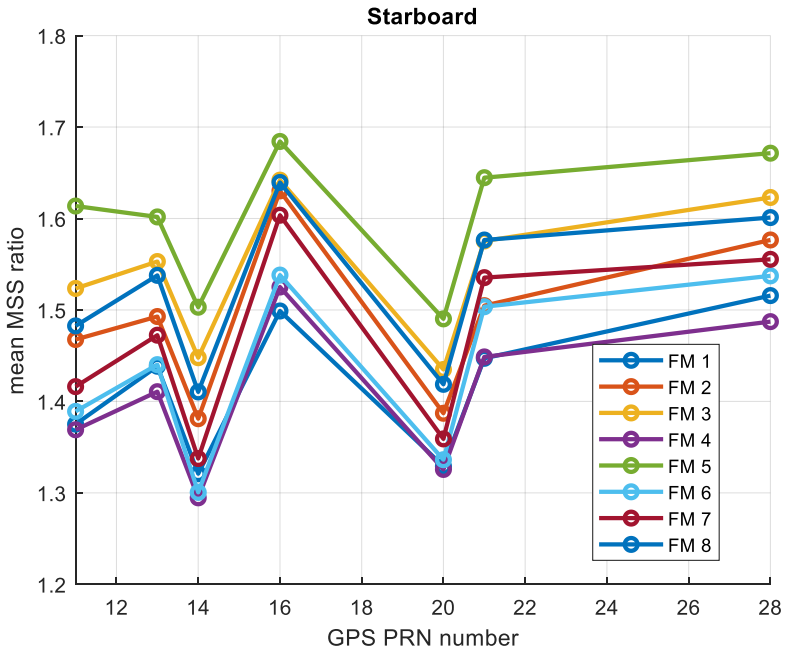

(a)

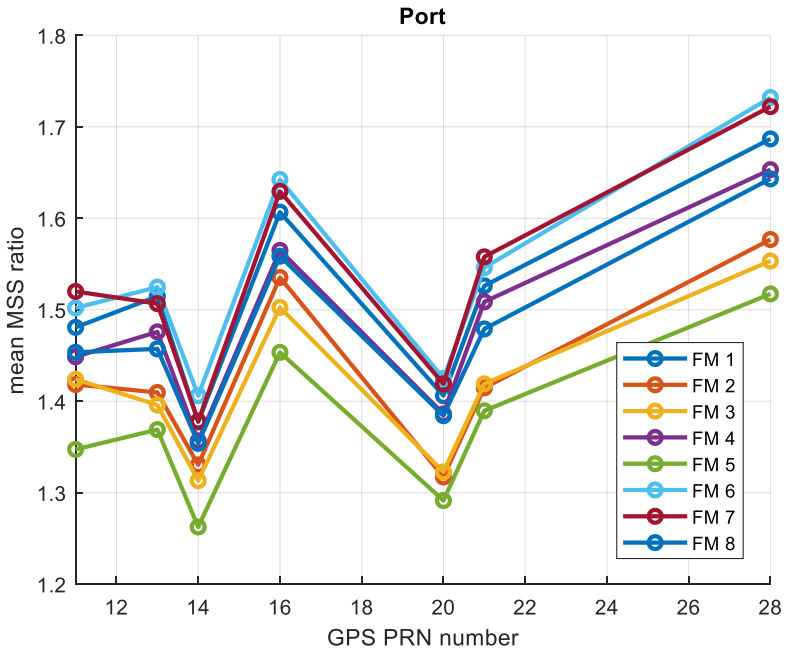

(b)

Figure V.5 Mean mssR vs. GPS PRN for all CYGNSS FMs. (a) Starboard; (b) Port

5.4.3 Normalized mss Ratio for FM Using Multiple PRNs

The next step is to remove the bias of the individual mssR map (normalized by its mean mssR) and then merge the normalized maps of multiple PRNs/FM pairs by a weighted average with the measurement density. This allows us to calculate a correction map to the receiver antenna gain pattern. The normalized mssR for FM1 using seven Block IIR PRNs are computed from two independent data subsets of the entire dataset. As shown in Figure V.6, the repeatability of the two normalized mssR maps demonstrates that it is an engineering calibration issue that needs to be resolved for the receiver antenna pattern.

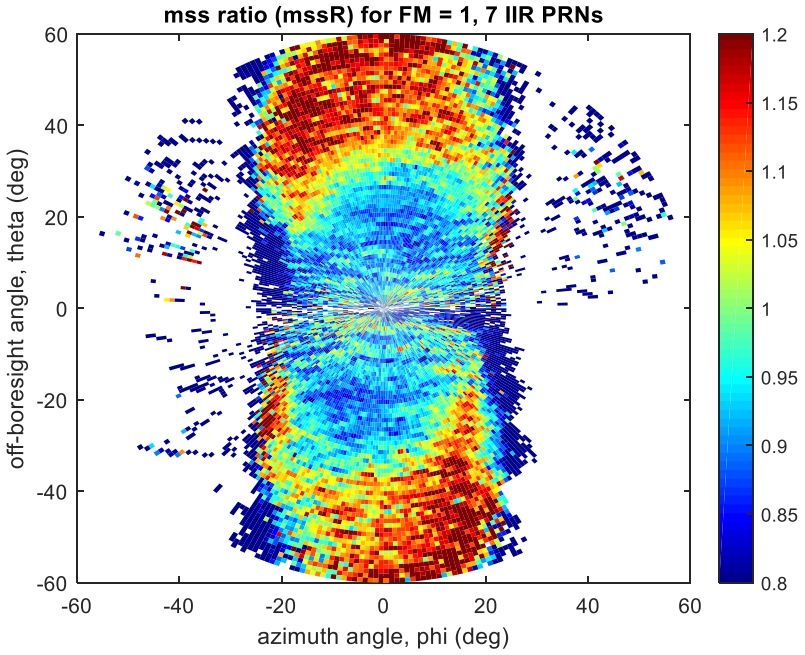

(a)

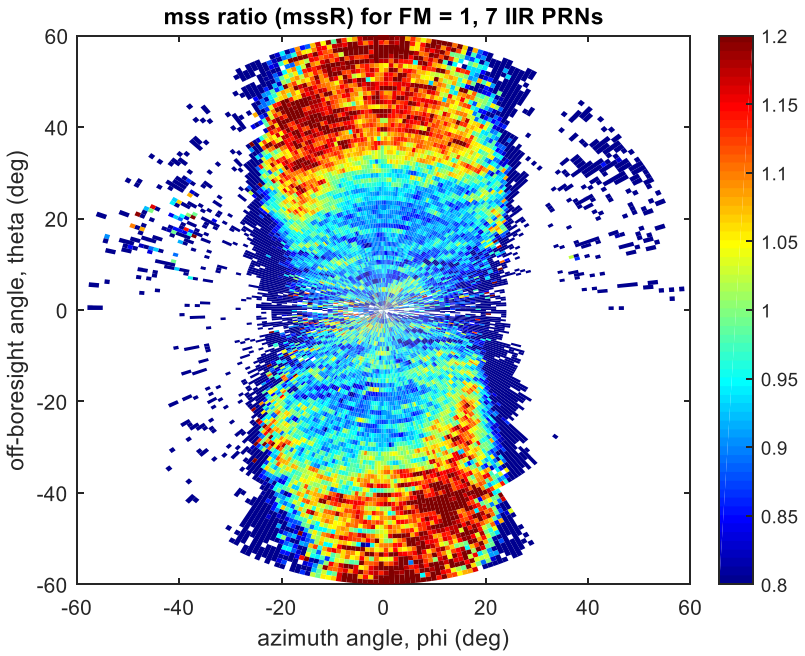

(b)

Figure V.6 Normalized mssR for FM1 using 7 Block IIR PRNs. (a) Calculated from data subset 1; (b) Calculated from data subset 2. Notice that the color scaled is symmetric about unity

5.5 Discussion on Modeling the Wave Tail

In this development, the Elfouhaily et al. spectrum is used to model the high frequency tail of the spectrum. However, that method lacks validation with in-situ measurements and also has a limitation with respect to the wind speed and inverse wave age.

The CYGNSS wave-model working group is currently investigating possibilities of developing a more accurate model for the high-frequency tail of the spectrum and validating the modeling using buoy measurements. The alternate approach under consideration include the spectrum integration method [141], [142], the Unified Wave INterface-Coupled Model (UWIN-CM) [143], and in-situ buoy observations, etc. This aims to provide more accurate matchup mss for improving CYGNSS Level 1 calibration and also for validation of CYGNSS's Level 2 mss product.

CHAPTER VI

Conclusions

6.1 Contributions

This dissertation focuses on engineering calibration and physical principles of GNSS-reflectometry for Earth remote sensing. The engineering calibration methods presented in this dissertation make significant contributions to the spatial coverage, calibration quality of the measured NBRCS and the geophysical data products produced by the NASA CYGNSS mission. The research is also useful to the system design, science investigation and engineering calibration of future GNSS-reflectometry missions.

A GPS constellation power monitor (GCPM) system has been designed, built, calibrated, and operated to estimate the transmit power (L1 C/A) and antenna pattern of each GPS satellite and to determine the EIRP of GPS signals. The measured GPS received power has been found to be highly repeatable. The measured EIRPs are verified by DLR/GSOC's independent measurements using a calibrated 30 m dish antenna with 50 dB L-band gain. The GPS transmit power (L1 C/A) of the full constellation was successfully estimated and applied to the CYGNSS L1b algorithm. It significantly reduces the PRN dependence of CYGNSS L1 and L2 data products. The advantages of the GCPM include: 1). low cost, high robustness; 2). stable control of temperature and system gain; 3). continuous full constellation monitoring. The system design and absolute power calibration scheme are helpful to the future design and implementation of GNSS receiver system.

An iterative approach is proposed to retrieve gain patterns of GPS and CYGNSS antennas using spaceborne measurement. Actual on-orbit data are used to determine the patterns in their operational environment. This cannot be practically achieved prior to launch using ground-based systems. A high-resolution map of the complete on-Earth portion of the GPS antenna's main beam results. A robustness test suggests that the procedure converges to a final set of patterns that is independent of first guess assumptions about the patterns. The new GPS and CYGNSS patterns have been incorporated into the science data processing algorithms used by the CYGNSS mission and have resulted in improved calibration performance.

A dynamic EIRP calibration approach is proposed to address the calibration issue brought by the flex power mode of the Block IIF and IIR-M satellites. CYGNSS direct signal measurements (originally intended for navigation use only) are calibrated and used to compute GPS transmitter EIRP in the direction of the CYGNSS spacecraft. By applying corrections to the direct signal EIRP, it is used to estimate the GPS EIRP in the direction of the specular reflection point. This dynamic EIRP calibration algorithm instantaneously detects and corrects for power fluctuations in all GPS transmitters and significantly reduces errors due to the azimuthal asymmetry of the GPS antenna gain patterns. Error analysis shows that the error in EIRP estimate is about 0.32 dB. The dynamic EIRP calibration successfully detects power fluctuations and corrects them in the calibration of nadir science measurements. This approach allows observations with Block IIF transmitters (approximately 37% of the entire dataset) to be included in the standard data products and further improves the calibration quality.

An approach for using modified WaveWatch III predicted mss to improve CYGNSS Level 1 calibration is proposed. The reference mss is produced by adding a high frequency tail (modeled using the Elfouhaily et al. spectrum) to the WW3 mss. By comparing the ratio of CYGNSS

measured mss and modified WW3 mss, it has been shown that the mean ratio has a dependence on both GPS PRNs and CYGNSS FMs, as well as each FM's starboard and port channels. The normalized mss ratio map from multiple PRNs calculated from two independent data subsets are strongly repeatable. Therefore it should be an engineering correction factor to be applied on the receiver antenna gain pattern. These indicate potential calibration errors existing in the characterization of the GPS transmitters and the CYGNSS receivers. By correcting these errors, this approach will help to improve the data quality of the CYGNSS Level 1 calibration and the Level 2 wind speed and mss products.

6.2 Future Work

Future work on antenna pattern calibration will focus on the following topics. 1) Identifying calibration error sources, including: a) time variations of the GPS transmit power; b) aging of the CYGNSS receiver system, which could introduce time-dependent errors in calibration of the received power, P_R; c) radio frequency interference (RFI) in the CYGNSS received signal (also possibly time dependent). 2) Making appropriate empirical corrections and revisiting the iterative retrieval process. 3) Conducting absolute calibration of antenna gain patterns for all GPS transmitters. 4) Validating the retrieved patterns with independent measurements. In combination with the GCPM, the zenith measurements can be used to absolutely calibrate the transmit power and antenna gain patterns for entire GPS constellation.

For the dynamic EIRP calibration algorithm, it is useful to analyze the wind speed retrieval errors from measurements taken: 1) in different regions of the zenith antenna pattern: higher gain vs lower gain, quadrants, and off-boresight; and 2) in different ranges of the specular incidence angle, which is related to the ZSR function and GPS antenna pattern. Future work includes

applying the following improvements: 1) use refined zenith antenna gain pattern and GPS ZSR functions 2) implement a two dimensional ZSR function for EIRP correction, depending on both off-boresight angles rather than the specular incidence angles (avoiding the empirical mapping); and 3) conduct an error analysis considering the inter-dependent relationship between the five sources of error.

Future work on the Level 1 end-to-end calibration algorithm will focus on: 1) validation of the high-frequency tail with independent wave models or in-situ measurement; 2) selection algorithm of the effective reference mss product to be used in the calibration diagnostics; 3) identifying the calibration errors in the zenith and nadir channels; and 4) applying corresponding corrections to the CYGNSS Level 1 calibration and assessing the performance improvement on both Level 1 calibration and Level 2 geophysical data products.

6.3 Summary of Research Publications

6.3.1 Journal Publications

T. Wang, C. Ruf, A. O'Brien, S. Gleason, D. McKague, B. Block, and A. Russel, "Measurement of GPS and CYGNSS Antenna Gain Patterns with a Spaceborne Antenna Range," submitted to *IEEE Transactions on Antennas and Propagation*, under review.

T. Wang, C. Ruf, S. Gleason, A. O'Brien, D. McKague, B. Block, and A. Russel, "Dynamic Calibration of GPS Effective Isotropic Radiated Power for GNSS-Reflectometry Earth Remote Sensing," submitted to *IEEE Transactions on Geoscience and Remote Sensing*, under review.

T. Wang, C. Ruf, B. Block, D. McKague, and S. Gleason, "Design and Performance of a GPS Constellation Power Monitor System for Improved CYGNSS L1b Calibration," *IEEE*

Journal of Selected Topics in Applied Earth Observations and Remote Sensing, vol. 12, no. 1, pp. 26-36, Jan. 2019.

6.3.2 Conference Publications

T. Wang, C. Ruf, "Measuring GPS EIRP in Real-Time with a Spaceborne GNSS-Reflectometry Remote Sensing System," 2021 United States National Committee of URSI National Radio Science Meeting (USNC-URSI NRSM), Boulder, CO, USA, 2021, pp. 146-147. (Ernest K. Smith USNC-URSI Student Prize: Second Place in Student Paper Competition)

C.K. Shum, Y. Zhang, Y. Yi, H. Ge, M. Ge, T. Wang, E. Cardellach, S. Gleason, W. Li, J. Johnson, C. Kuo, A. O'Brien, C. Ruf, Y. Xiao, and X. Wang, "Precision Orbit Determination for NASA's CYGNSS 8-Satellite Constellation Mission to Enable GNSS Altimetry Studies," 43rd COSPAR Scientific Assembly, Sydney, Australia, Jan 28 – Feb 4 2021.

T. Wang, C. Ruf, S. Gleason, D. McKague, A. O'Brien, and B. Block, "Monitoring GPS EIRP for CYGNSS Level 1 Calibration," 2020 IEEE International Geoscience and Remote Sensing Symposium, Virtual Conference.

T. Wang, V. U. Zavorotny, J. Johnson, Y. Yi, C. Ruf, S. Gleason, D. McKague, P. Hwang, E. Rogers, S. Chen, Y. Pan, and T. Bakker, "Improvement of CYGNSS Level 1 Calibration Using Modeling and Measurements of Ocean Surface Mean Square Slope," 2020 IEEE International Geoscience and Remote Sensing Symposium, Virtual Conference.

H. Carreno-Luengo, A. Camps, N. Flouri, M. Martin-Neira, C. Ruf, T. Wang, S. J. Khalsa, M. Clarizia, J. Reynolds, J. Johnson, A. O'Brien, L. Galdi, M. di Bisceglie, A. Dielacher, P. Jales, M. Unwin, L. King, and Giuseppe Foti, "The GRSS Standard for GNSS-Reflectometry," 2020 IEEE International Geoscience and Remote Sensing Symposium, Virtual Conference.

T. Wang, C. Ruf, V. U. Zavorotny, J. Johnson, and Y. Yi, "NASA Cyclone Global Navigation Satellite System: From Characterization of GPS EIRP to Physical Oceanography," 2019 American Geophysical Union (AGU) Fall Meeting, San Francisco, CA, 9-13 Dec 2019. (Invited Paper)

T. Wang, H. Huang, and W. Gu, "Investigation of Methane Emission in Permafrost Using In-situ Measurements and Satellite Remote Sensing Data for Climate Change Education," 2019 American Geophysical Union (AGU) Fall Meeting, San Francisco, CA, 9-13 Dec 2019.

T. Wang, C. Ruf, S. Gleason, B. Block, D. McKague, and A. O'Brien, "A Real-Time EIRP Level 1 Calibration Algorithm for the CYGNSS Mission Using the Zenith Measurements," 2019 IEEE International Geoscience and Remote Sensing Symposium, Yokohama, Japan, July 28 - August 2, 2019.

T. Wang, V. U. Zavorotny, J. Johnson, Y. Yi, and C. Ruf, "Integration of CYGNSS Wind and Wave Observations with the WaveWatch III Numerical Model," 2019 IEEE International Geoscience and Remote Sensing Symposium, Yokohama, Japan, July 28 - August 2, 2019.

T. Wang, C. Ruf, B. Block, and A. O'Brien, "Measuring GPS Transmit Antenna Pattern Using On-Orbit Receivers," 2019 IEEE International Symposium on Antennas and Propagation and USNC-URSI Radio Science Meeting, Atlanta, GA, 7-12 July 2019. (Honorable Mention in Student Paper Competition)

T. Wang, C. Ruf, S. Gleason, B. Block, D. McKague, and A. O'Brien, "Characterization of GPS EIRP and CYGNSS Ocean Level 1 Calibration Update," 2019 IEEE Specialist Meeting on Reflectometry using GNSS and other Signals of Opportunity, Benevento, Italy, 20–22 May, 2019.

V. U. Zavorotny, T. Wang, J. Johnson, Y. Yi, and C. Ruf, “Approaches of Incorporating Wave Model Information into CYGNSS Wind Speed Retrieval,” 2019 IEEE Specialist Meeting on Reflectometry using GNSS and other Signals of Opportunity, Benevento, Italy, 20–22 May, 2019.

T. Wang, C. Ruf, S. Gleason, D. McKague, and A. O’Brien, “CYGNSS Constellation Ocean Level 1 Calibration and Wind Speed Retrieval Update,” 2018 USNC-URSI National Radio Science Meeting, Boulder, CO, 9-12 Jan 2019.

T. Wang, V. U. Zavorotny, J. Johnson, C. Ruf, and Y. Yi, “Investigation of Ocean Surface Wind and Wave Coupling Using CYGNSS Observations,” 2018 American Geophysical Union (AGU) Fall Meeting, Washington, D.C., 10-14 Dec 2018. (Outstanding Student Presentation Award)

T. Wang, C. Ruf, B. Block, D. McKague, and S. Gleason, “Characterization of GPS L1 EIRP: Transmit Power and Antenna Gain Pattern,” 31th International Technical Meeting of the Satellite Division of the Institute of Navigation (ION GNSS+), Miami, FL, 24-28 Sep 2018.

T. Wang, V. U. Zavorotny, J. Johnson, C. Ruf, and Y. Yi, “Modeling of Sea State Conditions for Improvement of CYGNSS L2 Wind Speed Retrievals,” Proc. 2018 International Geoscience and Remote Sensing Symposium, Valencia, SPAIN, July 22-27 July 2018.

T. Wang, C. Ruf, B. Block, and D. McKague, “Characterization of the Transmit Power and Antenna Pattern of the GPS Constellation for the CYGNSS Mission,” Proc. 2018 International Geoscience and Remote Sensing Symposium, Valencia, SPAIN, 22-27 July 2018. (IEEE Mikio Takagi Student Prize: First Place in Student Paper Competition, Invited Paper)

T. Wang, C. Ruf, S. Gleason, B. Block, D. McKague, and D. Provost, “Development of GPS Constellation Power Monitor System for High Accuracy Calibration/Validation of the

CYGNSS L1b Data," Proc. 2017 International Geoscience and Remote Sensing Symposium, Fort Worth, TX, 23-28 July 2017. (Finalist of Student Paper Competition)

T. Wang, C. Ruf, S. Gleason, B. Block, D. McKague, and D. Provost, "Implementation and Calibration of GPS Constellation Power Monitor System for High Accuracy Calibration/ Validation of CYGNSS L1b Data," Proc. 2017 Specialist Meeting on Reflectometry Using GNSS and Other Signals of Opportunity, Ann Arbor, MI, 23-25 May 2017.

BIBLIOGRAPHY

[1] B. Hofmann-Wellenhof, H. Lichtenegger, and J. Collins, *Global Positioning System: Theory and Practice - 5th Edition*. Vienna, Austria: Springer-Verlag, 2001.

[2] P. Misra and P. Enge, *Global Positioning System: Signals, Measurements, and Performance - Revised 2nd Edition*. Lincoln, MA, USA: Ganga-Jamuna Press, 2001.

[3] T. A. Stansell, "Transit, the Navy navigation satellite system," *NAVIGATION, Journal of the Institute of Navigation*, vol. 18, no. 1, pp. 93-109, 1971, doi: 10.1002/j.2161-4296.1971.tb00077.x.

[4] B. W. Parkingson and J. J. Spilker, *Global Positioning System: Theory and Applications, Volume I*. Washington, D.C., USA: American Institute of Aeronautics and Astronautics, Inc., 1996.

[5] B. Hofmann-Wellenhof, H. Lichtenegger, and E. Wasle, *GNSS–Global Navigation Satellite Systems: GPS, GLONASS, Galileo, and More*. New York, NY, USA: Springer-Verlag, 2008.

[6] F. T. Ulaby and D. G. Long, *Microwave Radar and Radiometric Remote Sensing*. Ann Arbor, MI, USA: University of Michigan Press, 2014.

[7] V. U. Zavorotny, S. Gleason, E. Cardellach, and A. Camps, "Tutorial on remote sensing using GNSS bistatic radar of opportunity," *IEEE Geoscience and Remote Sensing Magazine*, vol. 2, no. 4, pp. 8-45, Dec. 2014, doi: 10.1109/MGRS.2014.2374220.

[8] T. P. Yunck, G. F. Lindal, and C. H. Liu, "Role of GPS in precise earth observation," *IEEE PLANS'88 - Position Location Navigation Symposium*, Orlando, FL, USA, 1988, pp. 251-258.

[9] A. S. Gurvich and T. G. Krasil'nikova, "Navigation satellites for radio sensing of the Earth' atmosphere," *Issled. Zemli Kosmosa (Soviet Journal of Remote Sensing, Engl. Transl.)*, vol. 6, pp. 1124-1131, 1990.

[10] R. Ware, C. Rocken, F. Solheim, D. Feng, B. Herman, M. Gorbu-nov, S. Sokolovskiy, K. Hardy, Y.-H. Kuo, X. Zou, K. Trenberth, T. Meehan, W. Melbourne, and S. Businger, "GPS sounding of the atmosphere from low Earth orbit: Preliminary results," *Bulletin of the American Meteorological Society*, vol. 77, no. 1, pp. 19-40, 1996, doi: 10.1175/1520-0477(1996)077<0019:GSOTAF>2.0.CO;2.

[11] E. R. Kursinski, G. A. Hajj, W. I. Bertiger, S. S. Leroy, T. K. Meehan, L. J. Romans, J. T. Schofield, D. J. McCleese, W. G. Melbourne, C. L. Thornton, T. P. Yunck, J. R. Eyre, and R. N. Nagatani, "Initial results of radio occultation observations of Earth's atmosphere using the Global Positioning System," *Science*, vol. 271, no. 5252, pp. 1107-1110, 1996, doi: 10.1126/science.271.5252.1107.

[12] C. D. Hall and R. A. Cordey, "Multistatic scatterometry," *IGARSS 1988 - 1988 IEEE International Geoscience and Remote Sensing Symposium*, Edinburgh, U.K., 1988, pp. 561-562, doi: 10.1109/IGARSS.1988.570200.

[13] M. Martin-Neira, "A passive reflectometry and interferometry system (PARIS): Application to ocean altimetry," *Ecological Society of America Journal*, vol. 17, no. 4, pp. 331-355, Dec. 1993.

[14] J. L. Garrison, S. J. Katzberg, and M. I. Hill, "Effect of sea roughness on bistatically scattered range coded signals from the Global Positioning System," *Geophysical Research Letters*, vol. 25, no. 13, pp. 2257-2260, July 1998, doi: 10.1029/98GL51615.

[15] B. Lin, S. J. Katzberg, J. L. Garrison, and B. A. Wielicki, "Relationship between GPS signals reflected from sea surfaces and surface winds: Modeling results and comparisons with aircraft measurements," *Journal of Geophysical Research: Oceans*, vol. 104, no. C9, pp. 20713-20727, Sept. 1999, doi: 10.1029/1999jc900176.

[16] G. Beyerle and K. Hocke, "Observation and simulation of direct and reflected GPS signals in radio occultation experiments," *Geophysical Research Letters*, vol. 28, no. 9, pp. 1895-1898, May 2001, doi: 10.1029/2000GL012530.

[17] G. Beyerle, K. Hocke, J. Wickert, T. Schmidt, C. Marquardt, and C. Reigber, "GPS radio occultations with CHAMP: A radio holographic analysis of GPS signal propagation in the troposphere and surface reflections," *Journal of Geophysical Research: Atmospheres*, vol. 107, no. D24, pp. ACL 27-1-ACL 27-14, Dec. 2002, doi: 10.1029/2001JD001402.

[18] S. T. Lowe, J. L. LaBrecque, C. Zuffada, L. J. Romans, L. E. Young, and G. A. Hajj, "First spaceborne observation of an Earth-reflected GPS signal," *Radio Science*, vol. 37, no. 1, pp. 7-1-7-28, Jan. 2002, doi: 10.1029/2000rs002539.

[19] A. Komjathy, V. U. Zavorotny, P. Axelrad, G. H. Born, and J. L. Garrison, "GPS signal scattering from sea surface: Wind speed retrieval using experimental data and theoretical model," *Remote Sensing of Environment*, vol. 73, no. 2, pp. 162-174, Aug. 2000, doi: 10.1016/S0034-4257(00)00091-2.

[20] J. L. Garrison, A. Komjathy, V. U. Zavorotny, and S. J. Katzberg, "Wind speed measurement using forward scattered GPS signals," *IEEE Transactions on Geoscience and Remote Sensing*, vol. 40, no. 1, pp. 50-65, Jan. 2002, doi: 10.1109/36.981349.

[21] A. Komjathy, M. Armatys, D. Masters, P. Axelrad, V. Zavorotny, and S. Katzberg, "Retrieval of ocean surface wind speed and wind direction using reflected GPS signals," *Journal of Atmospheric and Oceanic Technology*, vol. 21, no. 3, pp. 515-526, Mar. 2004,

doi: 10.1175/1520-0426(2004)021<0515:ROOSWS>2.0.CO;2.

[22] V. U. Zavorotny and A. G. Voronovich, "Scattering of GPS signals from the ocean with wind remote sensing application," *IEEE Transactions on Geoscience and Remote Sensing*, vol. 38, no. 2, pp. 951-964, Mar. 2000, doi: 10.1109/36.841977.

[23] S. J. Katzberg, R. A. Walker, J. H. Roles, T. Lynch, and P. G. Black, "First GPS signals reflected from the interior of a tropical storm: Preliminary results from Hurricane Michael," *Geophysical Research Letters*, vol. 28, no. 10, pp. 1981-1984, May 2001, doi: 10.1029/2000 GL012823.

[24] S. J. Katzberg, O. Torres, and G. Ganoe, "Calibration of reflected GPS for tropical storm wind speed retrievals," *Geophysical Research Letters*, vol. 33, no. 18, Sept. 2006, Art. no. L18602, doi: 10.1029/2006GL026825.

[25] S. J. Katzberg and J. Dunion, "Comparison of reflected GPS wind speed retrievals with dropsondes in tropical cyclones," *Geophysical Research Letters*, vol. 36, no. 17, Sept. 2009, Art. no. L17602, doi: 10.1029/2009GL039512.

[26] R. N. Treuhaft, S. T. Lowe, C. Zuffada, and Y. Chao, "2-cm GPS altimetry over Crater lake," *Geophysical Research Letters*, vol. 28, no. 23, pp. 4343-4346, Dec. 2001, doi: 10.102 9/2001GL013815.

[27] M. Martin-Neira, M. Caparrini, J. Font-Rossello, S. Lannelongue and C. S. Vallmitjana, "The PARIS concept: An experimental demonstration of sea surface altimetry using GPS reflected signals," *IEEE Transactions on Geoscience and Remote Sensing*, vol. 39, no. 1, pp. 142-150, Jan. 2001, doi: 10.1109/36.898676.

[28] M. Martin-Neira, P. Colmenarejo, G. Ruffini, and C. Serra, "Altimetry precision of 1 cm over a pond using the wide-lane carrier phase of GPS reflected signals," *Canadian Journal of Remote Sensing*, vol. 28, no. 3, pp. 394-403, June 2002, doi: 10.5589/m02-039.

[29] S. T. Lowe, C. Zuffada, Y. Chao, P. Kroger, L. E. Young, and J. L. Labrecque, "5-cm-precision aircraft ocean altimetry using GPS reflections," *Geophysical Research Letters*, vol. 29, no. 10, pp. 13-1-13-4, May 2002, doi: 10.1029/2002gl014759.

[30] S. T. Lowe, P. Kroger, G. Franklin, J. L. LaBrecque, J. Lerma, M. Lough, M. R. Marcin, R. J. Muellerschoen, D. Spitzmesser, and L. E. Young, "A delay/Doppler-mapping receiver system for GPS-reflection remote sensing," *IEEE Transactions on Geoscience and Remote Sensing*, vol. 40, no. 5, pp. 1150-1163, May 2002, doi: 10.1109/TGRS.2002.1010901.

[31] A. Rius, J. M. Aparicio, E. Cardellach, M. Martín-Neira, and B. Chapron, "Sea surface state measured using GPS reflected signals," *Geophysical Research Letters*, vol. 29, no. 23, pp. 37-1-37-4, Dec. 2002, doi: 10.1029/2002GL015524.

[32] G. Ruffini, F. Soulat, M. Caparrini, O. Germain, and M. Martín-Neira, "The Eddy experiment: Accurate GNSS-R ocean altimetry from low altitude aircraft," *Geophysical Research Letters*, vol. 31, no. 12, June 2004, Art. no. L12306, doi: 10.1029/2004GL019994.

[33] A. Komjathy, J. Maslanik, V. U. Zavorotny, P. Axelrad, and S. J. Katzberg, "Sea ice remote sensing using surface reflected GPS signals," *IGARSS 2000 - 2000 IEEE International Geoscience and Remote Sensing Symposium,* Honolulu, HI, USA, 2000, pp. 2855-2857, doi: 10.1109/IGARSS.2000.860270.

[34] M. B. Rivas, J. A. Maslanik, and P. Axelrad, "Bistatic scattering of GPS signals off arctic sea ice," *IEEE Transactions on Geoscience and Remote Sensing*, vol. 48, no. 3, pp. 1548-1553, Mar. 2010, doi: 10.1109/TGRS.2009.2029342.

[35] V. Zavorotny, D. Masters, A. Gasiewski, B. Bartram, S. Katzberg, P. Axelrad, and R. Zamora, "Seasonal polarimetric measurements of soil moisture using tower-based GPS bistatic radar," *IGARSS 2003 - 2003 IEEE International Geoscience and Remote Sensing Symposium,* Toulouse, France, 2003, pp. 781-783, doi: 10.1109/IGARSS.2003.1293916.

[36] D. Masters, P. Axelrad, and S. Katzberg, "Initial results of land-reflected GPS bistatic radar measurements in SMEX02," *Remote Sensing of Environment,* vol. 92, no. 4, pp. 507-520, Sept. 2004, doi: 10.1016/j.rse.2004.05.016.

[37] D. Masters, "Surface remote sensing applications of GNSS bistatic radar: Soil moisture and aircraft altimetry," Ph.D. dissertation, Univ. Colorado, Boulder, CO, USA, 2004.

[38] S. Gleason, S. Hodgart, Y. Sun, C. Gommenginger, S. Mackin, M. Adjrad, and M. Unwin, "Detection and processing of bistatically reflected GPS signals from low Earth orbit for the purpose of ocean remote sensing," *IEEE Transactions on Geoscience and Remote Sensing*, vol. 43, no. 6, pp. 1229-1241, June 2005, doi: 10.1109/TGRS.2005.845643.

[39] S. Gleason, "Remote sensing of ocean, ice and land surfaces using bistatically scattered GNSS signals from low earth orbit," Ph.D. dissertation, Univ. Surrey, Guildford, U.K., 2006.

[40] M. P. Clarizia, C. P. Gommenginger, S. T. Gleason, M. A. Srokosz, C. Galdi, and M. di Bisceglie, "Analysis of GNSS-R delay-Doppler maps from the UK-DMC satellite over the ocean," *Geophysical Research Letters*, vol. 36, no. 2, Jan. 2009, Art. no. L02608, doi: 10.1029/2008GL036292.

[41] S. Gleason, S. Lowe, and V. Zavorotny, "Remote sensing with bistatic GNSS reflections," in *GNSS Applications and Methods*, S. Gleason and D. Gebre-Egziabher, Eds. Boston, MA, USA: Artech House, 2009, pp. 399-436.

[42] S. Gleason, "Towards sea ice remote sensing with space detected GPS signals: Demonstration of technical feasibility and initial consistency check using low resolution sea ice information," *Remote Sensing*, vol. 2, no. 8, pp. 2017-2039, Aug. 2010, doi: 10.3390/ rs2082017.

[43] S. Gleason, "Space-based GNSS scatterometry: Ocean wind sensing using an empirically calibrated model," *IEEE Transactions on Geoscience and Remote Sensing*, vol. 51, no. 9, pp. 4853-4863, Sept. 2013, doi: 10.1109/TGRS.2012.2230401.

[44] M. Unwin, S. Duncan, P. Jales, P. Blunt, and J. Tye, "Implementing GNSS-reflectometry in space on the TechDemoSat-1 mission," *ION GNSS+ 2014 - 27th International Technical Meeting of the Satellite Division of The Institute of Navigation*, Tampa, FL, USA, Sept. 2014, pp. 1222-1235.

[45] M. Unwin, P. Jales, J. Tye, C. Gommenginger, G. Foti, and J. Rosello, "Spaceborne GNSS-reflectometry on TechDemoSat-1: Early mission operations and exploitation," *IEEE Journal of Selected Topics in Applied Earth Observations and Remote Sensing*, vol. 9, no. 10, pp. 4525-4539, Oct. 2016, doi: 10.1109/JSTARS.2016.2603846.

[46] C. S. Ruf, S. Gleason, Z. Jelenak, S. Katzberg, A. Ridley, R. Rose, J. Scherrer, and V. Zavorotny, "The CYGNSS nanosatellite constellation hurricane mission," *IGARSS 2012 - 2012 IEEE International Geoscience and Remote Sensing Symposium*, Munich, Germany, 2012, pp. 214-216, doi: 10.1109/IGARSS.2012.6351600.

[47] C. Ruf, M. Unwin, J. Dickinson, R. Rose, D. Rose, M. Vincent, and A. Lyons, "CYGNSS: Enabling the future of hurricane prediction," *IEEE Geoscience and Remote Sensing Magazine*, vol. 1, no. 2, pp. 52-67, June 2013, doi: 10.1109/MGRS.2013.2260911.

[48] H. Carreno-Luengo, A. Camps, P. Via, J. F. Munoz, A. Cortiella, D. Vidal, J. Jané, N. Catarino, M. Hagenfeldt, P. Palomo, and S. Cornara, "3Cat-2-An experimental nanosatellite for GNSS-R Earth observation: Mission concept and analysis," *IEEE Journal of Selected Topics in Applied Earth Observations and Remote Sensing*, vol. 9, no. 10, pp. 4540-4551, Oct. 2016, doi: 10.1109/JSTARS.2016.2574717.

[49] C. Jing, X. Niu, C. Duan, F. Lu, G. Di, and X. Yang, "Sea surface wind speed retrieval from the first Chinese GNSS-R mission: Technique and preliminary results," *Remote Sensing*, vol. 11, no. 24, Dec. 2019, Art. no. 3013, doi: 10.3390/rs11243013.

[50] D. Masters, V. Irisov, V. Nguyen, T. Duly, O. Nogués-Correig, L. Tan, T. Yuasa, J. Ringer, R. Sikarin, M. Gorbunov, and C. Rocken,"Status and plans for Spire's growing commercial constellation of GNSS science CubeSats," *Joint 6th ROM SAF User Workshop and 7th IROWG Workshop*, Helsingør, Denmark, Sept. 2019, pp. 19-25.

[51] A. Camps, A. Golkar, A. Gutierrez, J. A. Ruiz de Azua, J. F. Munoz-Martin, L. Fernandez, C. Diez, A. Aguilella, S. Briatore, R. Akhtyamov, and N. Garzaniti, "FSSCAT, the 2017 copernicus masters' "ESA Sentinel small satellite challenge" winner: A federated polar and soil moisture tandem mission based on 6U CubeSats," *IGARSS 2018 - 2018 IEEE International Geoscience and Remote Sensing Symposium*, Valencia, Spain, 2018, pp. 8285-8287, doi: 10.1109/IGARSS.2018.8518405.

[52] H. Carreno-Luengo, S. Lowe, C. Zuffada, S. Esterhuizen, and S. Oveisgharan, "Spaceborne GNSS-R from the SMAP mission: First assessment of polarimetric scatterometry over land and cryosphere," *Remote Sensing*, vol. 9, no. 4, Apr. 2017, Art. no. 362, doi: 10.3390/ rs9040362.

[53] Y. Sun, X. Wang, Q. Du, W. Bai, J. Xia, Y. Cai, D. Wang, C. Wu, X. Meng, Y. Tian, C. Liu, W. Li, D. Zhao, F. Li, and H. Qiao, "The status and progress of Fengyun-3E GNOS II

mission for GNSS remote sensing," *IGARSS 2019 - 2019 IEEE International Geoscience and Remote Sensing Symposium*, Yokohama, Japan, 2019, pp. 5181-5184, doi: 10.1109/IGARSS.2019.8899319.

[54] J. F. Munoz-Martin, N. Miguelez, R. Castella, L. Fernandez, A. Solanellas, P. Via, and A. Camps, "3CAT-4: Combined GNSS-R, L-band radiometer with RFI mitigation, and AIS receiver for a 1-unit CubeSat based on software defined radio," *IGARSS 2018 - 2018 IEEE International Geoscience and Remote Sensing Symposium*, Valencia, Spain, 2018, pp. 1063 -1066, doi: 10.1109/IGARSS.2018.8519037.

[55] A. Dielacher, H. Fragner, O. Koudelka, P. Beck, J. Wickert, E. Cardellach, and P. Høeg, "The ESA passive reflectometry and dosimetry (Pretty) mission," *IGARSS 2019 - 2019 IEEE International Geoscience and Remote Sensing Symposium*, Yokohama, Japan, 2019, pp. 5173-5176, doi: 10.1109/IGARSS.2019.8898720.

[56] H. Carreno-Luengo, A. Camps, C. Ruf, N. Flouri, M. Martin-Neira, T. Wang, S. J. Khalsa, M. P. Clarizia, J. Reynolds, J. T. Johnson, A. O'Brien, C. Galdi, M. di Bisceglie, A. Dielacher, P. Jales, M. Unwin, L. King, G. Foti, R. Shah, D. Pascual, B. Schreiner, M. Asgarimehr, J. Wickert, S. Ribo, and E. Cardellach, "The "Standard for GNSS-R data and metadata content" working group," submitted to *IEEE Geoscience and Remote Sensing Magazine*, under review.

[57] M. P. Clarizia, C. Ruf, P. Cipollini, and C. Zuffada, "First spaceborne observation of sea surface height using GPS-Reflectometry," *Geophysical Research Letters*, vol. 43, no. 2, pp. 767-774, Jan. 2016, doi: 10.1002/2015GL066624.

[58] W. Li, E. Cardellach, F. Fabra, S. Ribo, and A. Rius, "Assessment of spaceborne GNSS-R ocean altimetry performance using CYGNSS mission raw data," *IEEE Transactions on Geoscience and Remote Sensing*, vol. 58, no. 1, pp. 238-250, Jan. 2020, doi: 10.1109/TGRS.2019.2936108.

[59] E. Cardellach, W. Li, A. Rius, M. Semmling, J. Wickert, F. Zus, C. S. Ruf, and C. Buontempo, "First precise spaceborne sea surface altimetry with GNSS reflected signals," *IEEE Journal of Selected Topics in Applied Earth Observations and Remote Sensing*, vol. 13, pp. 102-112, 2020, doi: 10.1109/JSTARS.2019.2952694.

[60] J. Mashburn, P. Axelrad, C. Zuffada, E. Loria, A. Obrien, and B. Haines, "Improved GNSS-R ocean surface altimetry with CYGNSS in the seas of Indonesia," *IEEE Transactions on Geoscience and Remote Sensing*, vol. 58, no. 9, pp. 6071-6087, Sept. 2020, doi: 10.1109/TGRS.2020.2973079.

[61] B. Annane, B. Mcnoldy, S. M. Leidner, R. Hoffman, R. Atlas, and S. J. Majumdar, "A study of the HWRF analysis and forecast impact of realistically simulated CYGNSS observations assimilated as scalar wind speeds and as VAM wind vectors," *Monthly Weather Review*, vol. 146, no. 7, pp. 2221-2236, July 2018, doi: 10.1175/MWR-D-17-0240.1.

[62] S. M. Leidner, B. Annane, B. McNoldy, R. Hoffman, and R. Atlas, "Variational analysis of simulated ocean surface winds from the cyclone global navigation satellite system

(CYGNSS) and evaluation using a regional OSSE," *Journal of Atmospheric and Oceanic Technology*, vol. 35, no. 8, pp. 1571-1584, Aug. 2018, doi: 10.1175/JTECH-D-17-0136.1.

[63] Z. Cui, Z. Pu, V. Tallapragada, R. Atlas, and C. S. Ruf, "A preliminary impact study of CYGNSS ocean surface wind speeds on numerical simulations of hurricanes," *Geophysical Research Letters*, vol. 46, no. 5, pp. 2984-2992, Mar. 2019, doi: 10.1029/2019GL082236.

[64] D. Mayers and C. Ruf, "Tropical cyclone center fix using CYGNSS winds," *Journal of Applied Meteorology and Climatology*, vol. 58, no. 9, pp. 1993-2003, Sept. 2019, doi: 10. 1175/JAMC-D-19-0054.1.

[65] G. Foti, C. Gommenginger, P. Jales, M. Unwin, A. Shaw, C. Robertson, and J. Rosello, "Spaceborne GNSS reflectometry for ocean winds: First results from the UK TechDemoSat-1 mission," *Geophysical Research Letters*, vol. 42, no. 13, pp. 5435-5441, July 2015, doi: 10.1002/2015GL064204.

[66] M. P. Clarizia and C. S. Ruf, "Wind speed retrieval algorithm for the cyclone global navigation satellite system (CYGNSS) mission," *IEEE Transactions on Geoscience and Remote Sensing*, vol. 54, no. 8, pp. 4419-4432, Aug. 2016, doi: 10.1109/TGRS.2016.25413 43.

[67] C. S. Ruf, R. Atlas, P. S. Chang, M. P. Clarizia, J. L. Garrison, S. Gleason, S. J. Katzberg, Z. Jelenak, J. T. Johnson, S. J. Majumdar, and A. O'Brien, "New ocean winds satellite mission to probe hurricanes and tropical convection," *Bulletin of the American Meteorological Society*, vol. 97, no. 3, pp. 385-395, Mar. 2016, doi: 10.1175/BAMS-D-14-00218.1.

[68] A. Ghavidel and A. Camps, "Impact of rain, swell, and surface currents on the electromagnetic bias in GNSS-reflectometry," *IEEE Journal of Selected Topics in Applied Earth Observations and Remote Sensing*, vol. 9, no. 10, pp. 4643-4649, Oct. 2016, doi: 10.1109/JSTARS.2016.2538181.

[69] S. Soisuvarn, Z. Jelenak, F. Said, P. S. Chang, and A. Egido, "The GNSS reflectometry response to the ocean surface winds and waves," *IEEE Journal of Selected Topics in Applied Earth Observations and Remote Sensing*, vol. 9, no. 10, pp. 4678-4699, Oct. 2016, doi: 10. 1109/JSTARS.2016.2602703.

[70] B. Li, L. Yang, B. Zhang, D. Yang, and D. Wu, "Modeling and simulation of GNSS-R observables with effects of swell," *IEEE Journal of Selected Topics in Applied Earth Observations and Remote Sensing*, vol. 13, pp. 1833-1841, 2020, doi: 10.1109/JSTARS. 2020.2992037.

[71] A. Camp, H. Park, M. Pablos, G. Foti, C. P. Gommenginger, P.-W. Liu, and J. Judge, "Sensitivity of GNSS-R spaceborne observations to soil moisture and vegetation," *IEEE Journal of Selected Topics in Applied Earth Observations and Remote Sensing*, vol. 9, no. 10, pp. 4730-4742, Oct. 2016, doi: 10.1109/JSTARS.2016.2588467.

[72] C. Chew, R. Shah, C. Zuffada, G. Hajj, D. Masters, and A. J. Mannucci, "Demonstrating

soil moisture remote sensing with observations from the UK TechDemoSat-1 satellite mission," *Geophysical Research Letters*, vol. 43, no. 7, pp. 3317-3324, Apr. 2016, doi: 10.1002/2016GL068189.

[73] H. Carreno-Luengo, G. Luzi, and M. Crosetto, "Sensitivity of CyGNSS bistatic reflectivity and SMAP microwave radiometry brightness temperature to geophysical parameters over land surfaces," *IEEE Journal of Selected Topics in Applied Earth Observations and Remote Sensing*, vol. 12, no. 1, pp. 107-122, Jan. 2019, doi: 10.1109/JSTARS.2018.2856588.

[74] C. C. Chew and E. E. Small, "Soil moisture sensing using spaceborne GNSS reflections: Comparison of CYGNSS reflectivity to SMAP soil moisture," *Geophysical Research Letters*, vol. 45, no. 9, pp. 4049-4057, May 2018, doi: 10.1029/2018GL077905.

[75] A. Camps, M. Vall-llossera, H. Park, G. Portal, and L. Rossato, "Sensitivity of TDS-1 GNSS-R reflectivity to soil moisture: Global and regional differences and impact of different spatial scales," *Remote Sensing*, vol. 10, no. 11, Nov. 2018, Art. no. 1856, doi: 10.3390/rs10111856.

[76] M. M. Al-Khaldi, J. T. Johnson, A. J. O'Brien, A. Balenzano, and F. Mattia, "Time-series retrieval of soil moisture using CYGNSS," *IEEE Transactions on Geoscience and Remote Sensing*, vol. 57, no. 7, pp. 4322-4331, July 2019, doi: 10.1109/TGRS.2018.2890646.

[77] M. P. Clarizia, N. Pierdicca, F. Costantini, and N. Floury, "Analysis of CYGNSS data for soil moisture retrieval," *IEEE Journal of Selected Topics in Applied Earth Observations and Remote Sensing*, vol. 12, no. 7, pp. 2227-2235, July 2019, doi: 10.1109/JSTARS.2019.2895510.

[78] C. Chew and E. Small, "Description of the UCAR/CU soil moisture product," *Remote Sensing*, vol. 12, no. 10, May 2020, Art. no. 1558, doi: 10.3390/rs12101558.

[79] A. Camps, H. Park, J. Castellví, J. Corbera, and E. Ascaso, "Single-pass soil moisture retrievals using GNSS-R: Lessons learned," *Remote Sensing*, vol. 12, no. 12, June 2020, Art. no. 2064, doi: 10.3390/RS12122064.

[80] H. Park, A. Camps, J. Castellvi, and J. Muro, "Generic performance simulator of spaceborne GNSS-reflectometer for land applications," *IEEE Journal of Selected Topics in Applied Earth Observations and Remote Sensing*, vol. 13, pp. 3179-3191, 2020, doi: 10.1109/JSTARS.2020.3000391.

[81] M. Kurum, M. Deshpande, A. T. Joseph, P. E. O'Neill, R. H. Lang, and O. Eroglu, "SCoBi-Veg: A generalized bistatic scattering model of reflectometry from vegetation for signals of opportunity applications," *IEEE Transactions on Geoscience and Remote Sensing*, vol. 57, no. 2, pp. 1049-1068, Feb. 2019, doi: 10.1109/TGRS.2018.2864631.

[82] H. Carreno-Luengo, G. Luzi, and M. Crosetto, "Above-ground biomass retrieval over tropical forests: A novel GNSS-R approach with CYGNSS," *Remote Sensing*, vol. 12, no. 9, May 2020, Art. no. 1368, doi: 10.3390/RS12091368.

[83] A. Camps, A. Alonso-Arroyo, H. Park, R. Onrubia, D. Pascual, and J. Querol, "L-band vegetation optical depth estimation using transmitted GNSS signals: Application to GNSS-reflectometry and positioning," *Remote Sensing*, vol. 12, no. 15, Aug. 2020, Art. no. 2352, doi: 10.3390/RS12152352.

[84] C. Chew, J. T. Reager, and E. Small, "CYGNSS data map flood inundation during the 2017 Atlantic hurricane season," *Scientific Reports*, vol. 8, no. 1, pp. 1-8, 2018, doi: 10.1038/s41598-018-27673-x.

[85] K. Jensen, K. McDonald, E. Podest, N. Rodriguez-Alvarez, V. Horna, and N. Steiner, "Assessing L-Band GNSS-reflectometry and imaging radar for detecting sub-canopy inundation dynamics in a tropicalwetlands complex," *Remote Sensing*, vol. 10, no. 9, Sept. 2018, Art. no. 1431, doi: 10.3390/rs10091431.

[86] M. Rajabi, H. Nahavandchi, and M. Hoseini, "Evaluation of CYGNSS observations for flood detection and mapping during Sistan and Baluchestan torrential rain in 2020," *Water*, vol. 12, no. 7, July 2020, Art. no. 2047, doi: 10.3390/w12072047.

[87] S. L. K. Unnithan, B. Biswal, and C. Rüdiger, "Flood inundation mapping by combining GNSS-R signals with topographical information," *Remote Sensing*, vol. 12, no. 18, Sept. 2020, Art. no. 3026, doi: 10.3390/RS12183026.

[88] C. Chew and E. Small, "Estimating inundation extent using CYGNSS data: A conceptual modeling study," *Remote Sensing of Environment*, vol. 246, Sept. 2020, Art. no. 111869, doi: 10.1016/j.rse.2020.111869.

[89] S. V. Nghiem, C. Zuffada, R. Shah, C. Chew, S. T. Lowe, A. J. Mannucci, E. Cardellach, G. R. Brakenridge, G. Geller, and A. Rosenqvist, "Wetland monitoring with global navigation satellite system reflectometry," *Earth and Space Science*, vol. 4, no. 1, pp. 16-39, Jan. 2017, doi: 10.1002/2016EA000194.

[90] M. Morris, C. Chew, J. T. Reager, R. Shah, and C. Zuffada, "A novel approach to monitoring wetland dynamics using CYGNSS: Everglades case study," *Remote Sensing of Environment*, vol. 233, Nov. 2019, Art. no. 111417, doi: 10.1016/j.rse.2019.111417.

[91] A. Alonso-Arroyo, V. U. Zavorotny, and A. Camps, "Sea ice detection using UK TDS-1 GNSS-R data," *IEEE Transactions on Geoscience and Remote Sensing*, vol. 55, no. 9, pp. 4989-5001, Sept. 2017, doi: 10.1109/TGRS.2017.2699122.

[92] Q. Yan and W. Huang, "Detecting sea ice from TechDemoSat-1 data using support vector machines with feature selection," *IEEE Journal of Selected Topics in Applied Earth Observations and Remote Sensing*, vol. 12, no. 5, pp. 1409-1416, May 2019, doi: 10.1109/JSTARS.2019.2907008.

[93] Q. Yan and W. Huang, "Sea ice thickness measurement using spaceborne GNSS-R: First results with TechDemoSat-1 data," *IEEE Journal of Selected Topics in Applied Earth Observations and Remote Sensing*, vol. 13, pp. 577-587, 2020, doi: 10.1109/JSTARS.2020.2966880.

[94] N. Rodriguez-Alvarez, B. Holt, S. Jaruwatanadilok, E. Podest, and K. C. Cavanaugh, "An Arctic sea ice multi-step classification based on GNSS-R data from the TDS-1 mission," *Remote Sensing of Environment,* vol. 230, Sept. 2019, Art. no. 111202, doi: 10.1016/j.rse. 2019.05.021.

[95] B. J. Southwell and A. G. Dempster, "Sea ice transition detection using incoherent integration and deconvolution," *IEEE Journal of Selected Topics in Applied Earth Observations and Remote Sensing*, vol. 13, pp. 14-20, 2020, doi: 10.1109/JSTARS.2019. 2943510.

[96] Y. Zhu, T. Tao, J. Zou, K. Yu, J. Wickert, and M. Semmling, "Spaceborne GNSS reflectometry for retrieving sea ice concentration using TDS-1 data," *IEEE Geoscience and Remote Sensing Letters*, Apr. 2020, doi: 10.1109/LGRS.2020.2982959.

[97] A. Rius, E. Cardellach, F. Fabra, W. Li, S. Ribó, and M. Hernández-Pajares, "Feasibility of GNSS-R ice sheet altimetry in Greenland using TDS-1," *Remote Sensing*, vol. 9, no. 7, July 2017, Art. no. 742, doi: 10.3390/rs9070742.

[98] W. Li, E. Cardellach, F. Fabra, S. Ribó, and A. Rius, "Measuring Greenland ice sheet melt using spaceborne GNSS reflectometry from TechDemoSat-1," *Geophysical Research Letter,* vol. 47, no. 2, Jan. 2020, Art. no. e2019GL086477, doi: 10.1029/2019GL086477.

[99] A. G. Voronovich and V. U. Zavorotny, "Full-polarization modeling of monostatic and bistatic radar scattering from a rough sea surface," *IEEE Transactions on Antennas and Propagation*, vol. 62, no. 3, pp. 1362-1371, Mar. 2014, doi: 10.1109/TAP.2013.2295235.

[100] A. G. Voronovich and V. U. Zavorotny, "The transition from weak to strong diffuse radar bistatic scattering from rough ocean surface," *IEEE Transactions on Antennas and Propagation,* vol. 65, no. 11, pp. 6029-6034, Nov. 2017, doi: 10.1109/TAP.2017.2752219.

[101] A. G. Voronovich and V. U. Zavorotny, "Bistatic radar equation for signals of opportunity revisited," *IEEE Transactions on Geoscience and Remote Sensing*, vol. 56, no. 4, pp. 1959-1968, Apr. 2018, doi: 10.1109/TGRS.2017.2771253.

[102] T. Elfouhaily, B. Chapron, K. Katsaros, and D. Vandemark, "A unified directional spectrum for long and short wind-driven waves," *Journal of Geophysical Research: Oceans*, vol. 102, no. C7, pp. 15781-15796, July 1997, doi: 10.1029/97JC00467.

[103] M. Asgarimehr, J. Wickert, and S. Reich, "TDS-1 GNSS reflectometry: Development and validation of forward scattering winds," *IEEE Journal of Selected Topics in Applied Earth Observations and Remote Sensing*, vol. 11, no. 11, pp. 4534-4541, Nov. 2018, doi: 10.1109/ JSTARS.2018.2873241.

[104] S. Gleason, C. S. Ruf, M. P. Clarizia, and A. J. O'Brien, "Calibration and unwrapping of the normalized scattering cross section for the cyclone global navigation satellite system," *IEEE Transactions on Geoscience and Remote Sensing*, vol. 54, no. 5, pp. 2495-2509, May 2016, doi: 10.1109/TGRS.2015.2502245.

[105] S. Gleason, C. S. Ruf, A. J. Orbrien, and D. S. McKague, "The CYGNSS Level 1 calibration algorithm and error analysis based on on-orbit measurements," *IEEE Journal of Selected Topics in Applied Earth Observations and Remote Sensing*, vol. 12, no. 1, pp. 37-49, Jan. 2019, doi: 10.1109/JSTARS.2018.2832981.

[106] C. S. Ruf and R. Balasubramaniam, "Development of the CYGNSS geophysical model function for wind speed," *IEEE Journal of Selected Topics in Applied Earth Observations and Remote Sensing*, vol. 12, no. 1, pp. 66-77, Jan. 2019, doi: 10.1109/JSTARS.2018.2833075.

[107] C. S. Ruf, S. Gleason, and D. S. McKague, "Assessment of CYGNSS wind speed retrieval uncertainty," *IEEE Journal of Selected Topics in Applied Earth Observations and Remote Sensing*, vol. 12, no. 1, pp. 87-97, Jan. 2019, doi: 10.1109/JSTARS.2018.2825948.

[108] A. Wu, "Predictions and field measurements of the GPS Block IIR L1 and L2 ground powers," *2002 National Technical Meeting of The Institute of Navigation*, San Diego, CA, USA, Jan. 2002, pp. 931-938.

[109] P. Steigenberger, S. Thoelert, and O. Montenbruck, "Flex power on GPS Block IIR-M and IIF," *GPS Solutions*, vol. 23, no. 1, pp. 1-12, 2019, doi: 10.1007/s10291-018-0797-8.

[110] P. Steigenberger, A. Hauschild, S. Thoelert, and R. B. Langley, "US air force puts more power into GPS block IIR-M C/A-code," *GPS World*, vol. 28, no. 4, pp. 8-9, Apr. 2017.

[111] S. Thoelert, A. Hauschild, P. Steigenberger, R. B. Langley, and F. Antreich, "GPS IIR-M L1 transmit power redistribution: Analysis of GNSS receiver and high-gain antenna data," *NAVIGATION. Journal of the Institute of Navigation*, vol. 65, no. 3, pp. 423-430, 2018, doi: 10.1002/navi.250.

[112] P. Steigenberger, S. Thoelert, O. Esenbuga, A. Hauschild, and O. Montenbruck, "The new flex power mode: From GPS IIR-M and IIF satellites with extended coverage area," *Inside GNSS*, vol. 15, no. 3, pp. 52-56, 2020.

[113] T. Wang, C. Ruf, S. Gleason, B. Block, D. McKague, and D. Provost, "Development of GPS constellation power monitor system for high accuracy calibration/validation of the CYGNSS L1b data," *IGARSS 2017 - 2017 IEEE International Geoscience and Remote Sensing Symposium*, Fort Worth, TX, USA, 2017, pp. 1008-1011, doi: 10.1109/IGARSS.2017.8127125.

[114] T. Wang, C. S. Ruf, B. Block, D. S. McKague, and S. Gleason, "Design and performance of a GPS constellation power monitor system for improved CYGNSS L1b calibration," *IEEE Journal of Selected Topics in Applied Earth Observations and Remote Sensing*, vol. 12, no. 1, pp. 26-36, Jan. 2019, doi: 10.1109/JSTARS.2018.2867773.

[115] W. A. Marquis and D. L. Reigh, "The GPS Block IIR and IIR-M broadcast L-band antenna panel: Its pattern and performance," *NAVIGATION. Journal of the Institute of Navigation*, vol. 62, no. 4, pp. 329-347, Dec. 2015, doi: 10.1002/navi.123.

[116] Y. E. Bar-Sever, "A new model for GPS yaw attitude," *Journal of Geodesy*, vol. 70, pp. 714-723, Nov. 1996, doi: 10.1007/BF00867149.

[117] J. Kouba, "A simplified yaw-attitude model for eclipsing GPS satellites," *GPS Solutions*, vol. 13, pp. 1-12, 2009, doi: 10.1007/s10291-008-0092-1.

[118] M. P. Clarizia and C. S. Ruf, "Bayesian wind speed estimation conditioned on significant wave height for GNSS-R ocean observations," *Journal of Atmospheric and Oceanic Technology*, vol. 34, no. 6, pp. 1193-1202, June 2017, doi: 10.1175/JTECH-D-16-0196.1.

[119] P. Steigenberger, S. Thoelert, and O. Montenbruck, "GNSS satellite transmit power and its impact on orbit determination," *Journal of Geodesy*, vol. 92, no. 6, pp. 609-624, June 2018, doi: 10.1007/s00190-017-1082-2.

[120] S. Thoelert, M. Meurer, and S. Erker, "In-orbit analysis of antenna pattern anomalies of GNSS satellites," *NAVIGATION. Journal of The Institute of Navigation*, vol. 59, no. 2, pp. 135-144, 2012, doi: 10.1002/navi.11.

[121] T. Hartman, L. R. Boyd, D. Koster, J. A. Rajan, and J. Harvey, "Modernizing the GPS Block IIR spacecraft," *ION GPS 2000 - 13th International Technical Meeting of the Satellite Division of The Institute of Navigation*, Salt Lake City, UT, USA, Sept. 2000, pp. 2115-2121.

[122] F. Said, Z. Jelenak, P. S. Chang, and S. Soisuvarn, "An assessment of CYGNSS normalized bistatic radar cross section calibration," *IEEE Journal of Selected Topics in Applied Earth Observations and Remote Sensing*, vol. 12, no. 1, pp. 50-65, Jan. 2019, doi: 10.1109/JSTARS.2018.2849323.

[123] F. M. Czopek and S. Shollenberger, "Description and performance of the GPS Block I and II L-Band antenna and link budget," *ION GPS 1993 - 6th International Technical Meeting of the Satellite Division of the Institute of Navigation*, Salt Lake City, UT, USA, Sept. 1993, pp. 37-43.

[124] M. C. Moreau, F. H. Bauer, J. Russell Carpenter, E. P. Davis, G. W. Davis, and L. A. Jackson, "Preliminary results of the GPS flight experiment on the high Earth orbit AMSAT-OSCAR 40 spacecraft," *25th Annual American Astronautical Society Guidance and Control Conference*, Breckenridge, CO, USA, Feb. 2002, pp. AAS-02-004.

[125] T. Wang, C. Ruf, B. Block, and D. McKague, "Characterization of the transmit power and antenna pattern of the GPS constellation for the CYGNSS mission," *IGARSS 2018 - 2018 IEEE International Geoscience and Remote Sensing Symposium*, Valencia, Spain, 2018, pp. 4011-4014, doi: 10.1109/IGARSS.2018.8518531.

[126] J. E. Donaldson, J. J. K. Parker, M. C. Moreau, D. E. Highsmith, and P. D. Martzen, "Characterization of on-orbit GPS transmit antenna patterns for space users," *NAVIGATION. Journal of the Institute of Navigation*, vol. 67, no. 2, pp. 411-438, 2020, doi: 10.1002/navi.361.

[127] T. Wang, C. Ruf, B. Block, and A. O'Brien, "Measuring GPS transmit antenna pattern using on-orbit receivers," *2019 IEEE International Symposium on Antennas and Propagation and USNC-URSI Radio Science Meeting*, Atlanta, GA, USA, 2019, pp. 1717-1718, doi: 10.1109/APUSNCURSINRSM.2019.8888545.

[128] T. Wang and C. Ruf, "Measuring GPS EIRP in real-time with a spaceborne GNSS-reflectometry remote sensing system," *2021 United States National Committee of URSI National Radio Science Meeting (USNC-URSI NRSM)*, Boulder, CO, USA, 2021, pp. 146-147, doi: 10.23919/USNC-URSINRSM51531.2021.9336441.

[129] T. Wang, C. Ruf, A. O'Brien, S. Gleason, D. McKague, B. Block, and A. Russel, "Measurement of GPS and CYGNSS antenna gain patterns with a spaceborne antenna range," submitted to *IEEE Transactions on Antennas and Propagation*, under review.

[130] T. Wang, C. Ruf, B. Block, D. McKague, and S. Gleason, "Characterization of GPS L1 EIRP: Transmit power and antenna gain pattern," *ION GNSS+ 2018 - the 31st International Technical Meeting of the Satellite Division of The Institute of Navigation*, Miami, FL, USA, 2018, pp. 2879-2890, doi: 10.33012/2018.16101.

[131] S. Desai *et al.*, "GNSS-inferred positioning system and orbit analysis simulation software (GYPSY-OASIS)," Internet: https://gipsy-oasis.jpl.nasa.gov/.

[132] T. Wang, C. Ruf, S. Gleason, B. Block, D. McKague, and A. O'Brien, "A real-time EIRP Level 1 calibration algorithm for the CYGNSS mission using the zenith measurements," *IGARSS 2019 - 2019 IEEE International Geoscience and Remote Sensing Symposium*, Yokohama, Japan, 2019, pp. 8725-8728, doi: 10.1109/IGARSS.2019.8900456.

[133] T. Wang, C. S. Ruf, S. Gleason, A. J. O'Brien, D. S. McKague, and B. Block, "Monitoring GPS EIRP for CYGNSS Level 1 calibration," *IGARSS 2020 - 2020 IEEE International Geoscience and Remote Sensing Symposium*, online virtual conference.

[134] T. Wang, C. Ruf, S. Gleason, A. O'Brien, D. McKague, B. Block, and A. Russel, "Dynamic calibration of GPS effective isotropic radiated power for GNSS-reflectometry Earth remote sensing," submitted to *IEEE Transactions on Geoscience and Remote Sensing*, under review.

[135] S. J. Keihm, "TOPEX/Poseidon microwave radiometer (TMR). II. Antenna pattern correction and brightness temperature algorithm," *IEEE Transactions on Geoscience and Remote Sensing*, vol. 33, no. 1, pp. 138-146, Jan. 1995, doi: 10.1109/36.368214.

[136] T. Wang, V. U. Zavorotny, J. Johnson, Y. Yi, C. Ruf, S. Gleason, D. McKague, P. Hwang, E. Rogers, S. Chen, Y. Pan, and T. Bakker, "Improvement of CYGNSS Level 1 calibration using modeling and measurements of ocean surface mean square slope," *IGARSS 2020 - 2020 IEEE International Geoscience and Remote Sensing Symposium*, online virtual conference.

[137] WaveWatch III Development Group, "User manual and system documentation of WaveWatch III version 5.16," MMAB Technical Note, Oct. 2016.

[138] A. Camps, J. Font, J. Etcheto, V. Caselles, A. Weill, I. Corbella, M. Vall-Ilossera, N. Duffo, F. Torres, R. Villarino, L. Enrique, A. Julia, C. Gabarro, J. Boutin, E. Rubio, S. C. Reising, P. Wursteisen, M. Berger, and M. Martfn-Neira, "Sea surface emissivity observations at L-band: First results of the wind and salinity experiment WISE 2000," *IEEE Transactions on Geoscience and Remote Sensing*, vol. 40, no. 10, pp. 2117-2130, Oct. 2002, doi: 10.1109/TGRS.2002.802496.

[139] T. Wang, V. U. Zavorotny, J. Johnson, C. Ruf, and Y. Yi, "Modeling of sea state conditions for improvement of CYGNSS L2 wind speed retrievals," *IGARSS 2018 - 2018 IEEE International Geoscience and Remote Sensing Symposium*, Valencia, Spain, 2018, pp. 8288-8291, doi: 10.1109/IGARSS.2018.8518686.

[140] V. Zavorotny, "Mean square slope correction for the WW3 mss entries", unpublished private communication, Mar. 2019.

[141] P. A. Hwang, F. J. Ocampo-Torres, and H. García-Nava, "Wind sea and swell separation of 1D wave spectrum by a spectrum integration method," *Journal of Atmospheric and Oceanic Technology*, vol. 29, no. 1, pp. 116-128, Jan. 2012, doi: 10.1175/JTECH-D-11-00075.1.

[142] P. A. Hwang and T. Ainsworth, "L-Band ocean surface roughness," *IEEE Transactions on Geoscience and Remote Sensing*, vol. 58, no. 6, pp. 3988-3999, June 2020, doi: 10.1109/TGRS.2019.2960130.

[143] S. S. Chen, W. Zhao, M. A. Donelan, and H. L. Tolman, "Directional wind-wave coupling in fully coupled atmosphere-wave-ocean models: Results from CBLAST-hurricane," *Journal of the Atmospheric Sciences*, vol. 70, no. 10, pp. 3198-3215, Oct. 2013, doi: 10.1175/JAS-D-12-0157.1.